

Electric field sensing near the surface microstructure of an atom chip using cold Rydberg atoms

by

Jeffrey D. Carter

A thesis
presented to the University of Waterloo
in fulfilment of the
thesis requirement for the degree of
Doctor of Philosophy
in
Physics

Waterloo, Ontario, Canada, 2013

© Jeffrey D. Carter 2013

I hereby declare that I am the sole author of this thesis. This is a true copy of the thesis, including any required final revisions, as accepted by my examiners.

I understand that my thesis may be made electronically available to the public.

Abstract

This thesis reports experimental observations of electric fields using Rydberg atoms, including dc field measurements near the surface of an atom chip, and demonstration of measurement techniques for ac fields far from the surface. Associated theoretical results are also presented, including Monte Carlo simulations of the decoherence of Rydberg states in electric field noise as well as an analytical calculation of the statistics of dc electric field inhomogeneity near polycrystalline metal surfaces.

DC electric fields were measured near the heterogeneous metal and dielectric surface of an atom chip using optical spectroscopy on cold atoms released from the trapping potential. The fields were attributed to charges accumulating in the dielectric gaps between the wires on the chip surface. The field magnitude and direction depend on the details of the dc biasing of the chip wires, suggesting that fields may be minimized with appropriate biasing.

Techniques to measure ac electric fields were demonstrated far from the chip surface, using the decay of a coherent superposition of two Rydberg states of cold atoms. We have used the decay of coherent Rabi oscillations to place some bounds on the magnitude and frequency dependence of ac field noise.

The rate of decoherence of a superposition of two Rydberg states was calculated with Monte Carlo simulations. The states were assumed to have quadratic Stark shifts and the power spectrum of the electric field noise was assumed to have a power-law dependence of the form $1/f^\kappa$. The decay is exponential at long times for both free evolution of the superposition and Hahn spin-echo sequences with a π refocusing pulse applied to eliminate the effects of low-frequency field noise. This decay time may be used to calculate the magnitude of the field noise if κ is known.

The dc field inhomogeneity near polycrystalline metal surfaces due to patch potentials on the surface has been calculated, and the rms field scales with distance to the surface as $1/z^2$. For typical evaporated metal surfaces the magnitude of the rms field is comparable to the image field of an elementary charge near the surface.

Acknowledgements

I would first like to thank my supervisor, Dr. James Martin, for his hard work, dedication, and assistance through this project. I'd also like to thank Dr. Martin for reading the drafts of this thesis and making many helpful comments and suggestions.

Thanks to Owen Cherry, my colleague during the initial phase of this project. Owen fabricated the atom chips described in this work and was involved in the assembly of the vacuum chamber and the MOT optics.

I would like to thank Dr. Edward Eyler for travelling here from Connecticut to serve on the thesis examining committee. Thanks also to the Waterloo faculty who served on my examining committee, Dr. Adrian Lupascu, Dr. Frank Wilhelm-Mauch, Dr. Zoran Mišković, for their careful reading and suggestions. I would like to thank Dr. Lupascu, Dr. Wilhelm-Mauch, Dr. Mišković, and Dr. Donna Strickland for serving on my advisory committee.

Thanks to to all Martin group technicians and graduate students along the way who contributed to this project. These include: Maria Fedorov, Joe Petrus, Joel Keller, Rodger Mantifel, Ashton Mugford, Kourosch Afrousheh, Parisa Bohlouli-Zanjani, Lucas Jones, as well as many others. I would also like to thank the staff at Science Technical Services for their help and expertise, in particular the late Andy Colclough. Thanks also to the staff in the department office, especially Judy McDonnell, the graduate secretary, for all their help over the years.

Many thanks to all the friends and family who have encouraged and supported me, especially my wife Giselle, son Joel, and daughter Caroline.

Dedication

To Giselle, Joel, and Caroline.

Table of Contents

List of Figures	ix
1 Introduction	1
1.1 Electric fields near metal surfaces	1
1.2 Rydberg atoms	2
1.3 Structure of the thesis	3
2 Sensing of dc electric fields near the surface	5
2.1 Summary	5
2.2 Introduction	6
2.3 Experiment	8
2.3.1 Summary of techniques	8
2.3.2 Trap loading	9
2.3.3 Atom chip	10
2.3.4 Optical excitation	10
2.3.5 Measurement of electric fields	11
2.4 Results	14
2.5 Electric field measurement uncertainty	18
2.6 Summary and outlook	22

3	Theoretical background and ac electric field measurement techniques	24
3.1	Introduction	24
3.2	Ion traps	25
3.2.1	Surface noise	27
3.2.2	Noise models	27
3.3	Noise spectroscopy with free evolution Rydberg state superpositions	30
3.3.1	Introduction	30
3.3.2	Free evolution with linear coupling to noise	30
3.3.3	Free evolution with quadratic coupling to noise	35
3.4	Coherent manipulation with microwaves	39
3.5	Noise spectroscopy with driven evolution of Rydberg states	43
3.6	Numerical simulations	46
3.6.1	Monte Carlo calculations of decoherence $f_z(t)$	46
3.6.2	Time-evolution of the density matrix	54
3.7	Sensitivity limits	57
3.8	Summary	60
4	AC electric field measurements	62
4.1	Introduction	62
4.2	Apparatus	62
4.3	Coherent manipulation, Ramsey and spin-echo results	64
4.4	Microwave field homogeneity	69
4.5	Intermediate state population in two-photon resonances	77
4.6	Summary	79

5	Energy shifts of Rydberg atoms due to patch fields near metal surfaces	81
5.1	Summary	81
5.2	Introduction	82
5.3	Rydberg-atom energy shifts in external fields	83
5.4	Statistics of the patch fields	85
5.5	Models for the surface patch potentials	90
5.6	Fluctuations in the electric field	94
5.7	Patch fields and Rydberg atoms – estimates of energy level shifts	96
5.8	Potential and field covariance functions	98
5.9	Summary and outlook	99
6	Summary and future work	100
6.1	Summary of results	100
6.2	Future work	102
	References	103

List of Figures

2.1	Experimental apparatus and timings	7
2.2	Rydberg excitation spectra and determination of compensating field	13
2.3	Distance dependence and repeatability of compensating field measurements	15
2.4	Compensating field as a function of microtrap hold time	17
2.5	Effect of Stark shift on measured signal	19
3.1	Distance scaling of electric field noise in ion traps	26
3.2	Bloch-sphere representation of dephasing during a Ramsey sequence	32
3.3	Filter function $g_N(\omega, \tau)$ for CP and CPMG sequences with various N	34
3.4	Energy vs. electric field with quadratic and linear Stark shifts	35
3.5	Energy level schematic for a two-photon transition between Rydberg states	41
3.6	Excitation of the intermediate state $ a\rangle$ during two-photon Rabi flopping .	42
3.7	Simulated coherence decay for pure $1/f$ electric field noise	48
3.8	Coherence decay with scaled time units in pure $1/f$ noise	49
3.9	Coherence decay time constant vs S_0 : $1/\sqrt{f}$, $1/f$, $1/f^{3/2}$ noise	50
3.10	Coherence decay with scaled time units in $1/f^{3/2}$ noise	51
3.11	Coherence decay with scaled time units in $1/f^{1/2}$ noise	52
3.12	Dependence of decoherence rate on ω_c/Γ_f for $1/f^{1/2}$ noise	53

4.1	Geometry of Rydberg excitation	63
4.2	Rabi flopping of the two-photon $49s_{1/2} - 48s_{1/2}$ transition	65
4.3	Two-photon microwave spectrum of the $49s_{1/2} - 48s_{1/2}$ transition	66
4.4	Ramsey sequence for the two-photon $49s_{1/2} - 48s_{1/2}$ transition	67
4.5	Hahn spin-echo sequence for the two-photon $49s_{1/2} - 48s_{1/2}$ transition	68
4.6	Microwave standing waves	72
4.7	Measurement of microwave homogeneity with ac Stark shifts	73
4.8	Reducing sample size to improve microwave homogeneity	74
4.9	Effect of microwave homogeneity on decay of Rabi oscillations	75
4.10	Decay of rabi oscillations	76
4.11	Simulation of state populations in a two-photon Ramsey experiment	78
4.12	Intermediate state populations for various microwave amplitudes	80
5.1	Monte Carlo simulation of surface potential covariance	92
5.2	SEM image of a gold surface with computed covariance of surface potential	93
5.3	Numerical calculation and asymptotic series expansion of $G(2, z/w)$	95

Chapter 1

Introduction

1.1 Electric fields near metal surfaces

Devices such as microfabricated ion traps [1] and magnetic microtraps or “atom chips” [2, 3] are used to confine ultracold gas-phase atoms, molecules and ions near μm -scale surface structures which create the electric or magnetic fields necessary for trapping. Advantages of this miniaturization include scalability, allowing many independent trapping zones on a single device, and large field gradients which give high mechanical resonance frequencies of the trapped particles that allow for fast changes in the trapping geometry.

While the solid-state devices above are classical in nature, proposals also exist to combine the benefits of gas-phase ultracold atoms or molecules (long coherence times for information storage) with those of solid-state quantum devices (strong interactions for fast gates and scalability) in *hybrid* quantum devices [4, 5, 6].

To take advantage of large field gradients or couple strongly to solid-state quantum systems, the atoms or ions must be confined close to the surface of the device, with atom-surface distances comparable to the scale of the structures used for confinement, $\approx 10 - 100 \mu\text{m}$. These surfaces may be heterogeneous with exposed metal electrodes and dielectric insulators, which can be sources of uncontrollable and unwanted electric fields. Near dielectric surfaces, charge accumulation and time-dependent electric fields due to ad-

sorbates [7] may be problematic. Even flat polycrystalline metal surfaces may generate significant inhomogeneous electric “patch” fields due to the differing work-function between grains [8, 9]. Electric field noise tends to increase close to surfaces, which limits the degree to which ion traps may be miniaturized (see, for example Refs. [10, 11] and references therein). Electric field noise near surfaces is also a problem identified in proposals to manipulate Rydberg atoms near surfaces [12].

Identifying and removing the sources of undesirable electric fields near solid-state devices requires that the fields be measured. Ideally such a measurement should be performed *in situ*, under regular operating conditions without disrupting the function of the device. In this work, measurements of electric fields near the surface of an atom chip are made using Rydberg atoms — atoms with a valence electron excited to high principal quantum number n . Cold ground state atoms trapped using the chip are released and then excited to Rydberg states. Measurements of dc electric fields are made using optical spectroscopy of a single Rydberg state, and ac electric field noise is measured using the dephasing of a coherent superposition of two Rydberg states.

1.2 Rydberg atoms

Many properties of Rydberg atoms scale as powers of n and may be scaled by orders of magnitude from their values for ground state atoms (the states used in this work range from $n = 36$ to $n = 49$, compared to $n = 5$ for the ground state of ^{87}Rb). For example, the electric polarizability scales as n^7 , and spontaneous emission lifetimes of low angular-momentum Rydberg states scale as n^3 [13]. The long radiative lifetimes allow energy shifts of Rydberg states to be accurately measured. When accurate measurement of energy shifts is combined with the large polarizabilities of Rydberg atoms, electric fields can be detected spectroscopically with high sensitivity [14, 15]. Selective field ionization [16] is a powerful tool, enabling state-sensitive charged-particle detection of Rydberg atoms. This state sensitivity allows for spectroscopy of microwave transitions between Rydberg states, and observation of coherent population transfer between states [17]. In this work, the state selectivity is used to study the dephasing of coherent superpositions.

The presence of electric fields near microfabricated devices has been previously observed using Rydberg atoms [5, 18]. Adsorbed contaminants have also been detected using Rydberg atoms in another class of experiments, studies of intrinsic “image-field” ionization of Rydberg atoms in an atomic beam incident on a metal surface [19, 20]. These experiments were hampered by stray electric fields and required efforts to avoid adsorption of contaminants and the use of flat, single-crystal orientation surfaces to minimize the magnitude of patch fields. However, the atomic motion and large electric fields required to pull the ionized atoms away from the surface for detection made any systematic study of the distance dependence of the patch fields impossible.

1.3 Structure of the thesis

The primary area of study in this thesis is the observation of electric fields using Rydberg atoms. In the major experimental work, dc electric fields were measured near the surface of an atom chip using optical spectroscopy, and the decay of a coherent superposition of two Rydberg states was used to place some bounds on the magnitude and frequency dependence of ac field noise far from the chip surface. This thesis also includes some theoretical work: calculations of dc field inhomogeneity near polycrystalline metal surfaces and also calculations of the rate of decoherence of a superposition of two quadratically Stark-shifting Rydberg states in the presence of electric field noise with a power spectrum of the form $1/f^\kappa$. The chapters are organized as follows:

Chapter 2 contains measurements of dc electric fields near the surface of an atom chip with a heterogeneous surface of gold wires and SiO_2 insulating gaps on a silicon substrate. Fields were measured using optical spectroscopy on cold atoms released from a magnetic microtrap. The observed fields are attributed to charging of the insulating gaps between the wires. The measured field magnitude and direction were strongly affected by voltage biasing of the chip wires related to how currents were applied, a surprising result given that all the currents were shut off and the chip wires returned to ground prior to the Rydberg excitation. This result suggests that charging of insulating gaps may be minimized in future work with appropriate voltage biasing of structures on the surface.

Chapter 3 contains the theoretical background necessary to measure slowly varying ac electric fields with noise power spectra of the form $1/f^\kappa$ using Rydberg atoms. The problem of motional heating in ion traps is discussed as a motivation for the work and several theoretical microscopic models to explain the origin of the field noise are discussed. The techniques of spin-echo and spin-locking are explained and adapted to the measurement of field noise using the dephasing of Rydberg atoms. These techniques were originally developed to preserve coherence in nuclear magnetic resonance (NMR) experiments and have more recently been extended to measure noise, both in NMR and solid-state qubits. The decoherence rate of a superposition of states with quadratic Stark shifts in the presence of electric field noise is calculated using Monte Carlo simulations. The noise power spectral density in the calculations is of the form $1/f^\kappa$, for three values of κ corresponding to predictions of the microscopic models for field noise. Finally, the ultimate sensitivity of noise measurements with Rydberg atoms is estimated.

Chapter 4 contains experimental results using the two-photon $49s_{1/2} - 48s_{1/2}$ transition of ^{87}Rb . Observation of Rabi oscillations between the two states demonstrates the coherent control required for implementing spin-echo and spin-locking measurements of noise. The results of spectroscopy and Hahn spin-echo coherence decay have been used to set some upper and lower bounds on the electric field noise amplitude measured several mm away from the surface of the chip. A significant microwave field inhomogeneity due to standing waves in the microwave fields was observed. The decay rate of coherent Rabi oscillations was used to estimate the microwave field homogeneity over small samples of Rydberg atoms. Finally, the amount of undesired excitation of the intermediate $48p_{3/2}$ state during microwave pulses is estimated and strategies for minimizing this effect are discussed.

Chapter 5 contains calculations of the statistical properties of dc electric field inhomogeneities near metal surfaces due to random potentials on the surface, such as may be caused by polycrystalline grain structures. It is shown that the rms variation in the field strength scales with distance as $1/z^2$, and that spatial variations in the field over the size of the atom are not important.

Chapter 6 contains a summary and suggestions for future work.

Chapter 2

Electric field sensing near the surface microstructure of an atom chip using cold Rydberg atoms

This article is directly based on an article published by the author, together with O. Cherry and J. D. D. Martin [21].

2.1 Summary

The electric fields near the heterogeneous metal/dielectric surface of an atom chip were measured using cold atoms. The atomic sensitivity to electric fields was enhanced by exciting the atoms to Rydberg states that are 10^8 times more polarizable than the ground state. We attribute the measured fields to charging of the insulators between the atom chip wires. Surprisingly, it is found that although the chip wire currents were turned off before Rydberg excitation, the measured fields were strongly influenced by how the wire currents had been applied. These fields may be dramatically lowered with appropriate voltage biasing, suggesting configurations for the future development of hybrid quantum systems.

2.2 Introduction

It is desirable to be able to combine the benefits of gas-phase ultracold atoms/molecules (long coherence times for information storage) with those of solid-state quantum devices (strong interactions for fast gates) in *hybrid* quantum devices [4, 5, 6]. Rydberg, or “swollen”, atoms – atoms with a highly excited valence electron – may enable hybrid devices by amplifying the interactions between atoms and devices in a similar manner to the enhancement of interactions between atoms [22, 23]. However, these hybrid systems will require atoms to be located near a heterogeneous surface with exposed metal electrodes and dielectric insulators, which can be sources of uncontrollable and unwanted electric fields.

Rydberg atoms have a high sensitivity to small electric fields [13, 14, 15] and this can be problematic near surfaces. For example, to study the intrinsic “image-field” ionization of Rydberg atoms near a metal surface one must avoid adsorption of contaminants and use flat, single-crystal orientation surfaces [19, 20]. Even flat polycrystalline metal surfaces may generate significant inhomogeneous electric fields due to the differing work-function between grains [8, 9]. In addition to static fields, surfaces may also be a source of enhanced fluctuating fields, a problem which plagues ion-trapping (see Ref. [24] and references therein) and is also a consideration for Rydberg atoms near surfaces [12]. For dielectrics, which are a necessary part of any non-trivial device — as insulating gaps for instance — charging and time-dependent electric fields due to adsorbates [7] must also be considered.

Atom chips [2, 3] offer the ability to trap cold neutral atoms close to surfaces, and observe the influence of surfaces [25]. This technology has recently been exploited by Tauschinsky *et al.* [18] to study the shifts of Rydberg states due to adsorbates on metal surfaces as a function of distance away from a metal surface (a shield between the chip wires and atoms).

In this chapter, I describe experiments incorporating laser cooled ^{87}Rb , an atom chip, Rydberg excitation, and charged particle detection (see Fig. 2.1). This allows the sensing of electric fields near atom chip wire structures, with insulating gaps between wires that are typical of surface devices. The Stark effect is well-known and has been extensively exploited

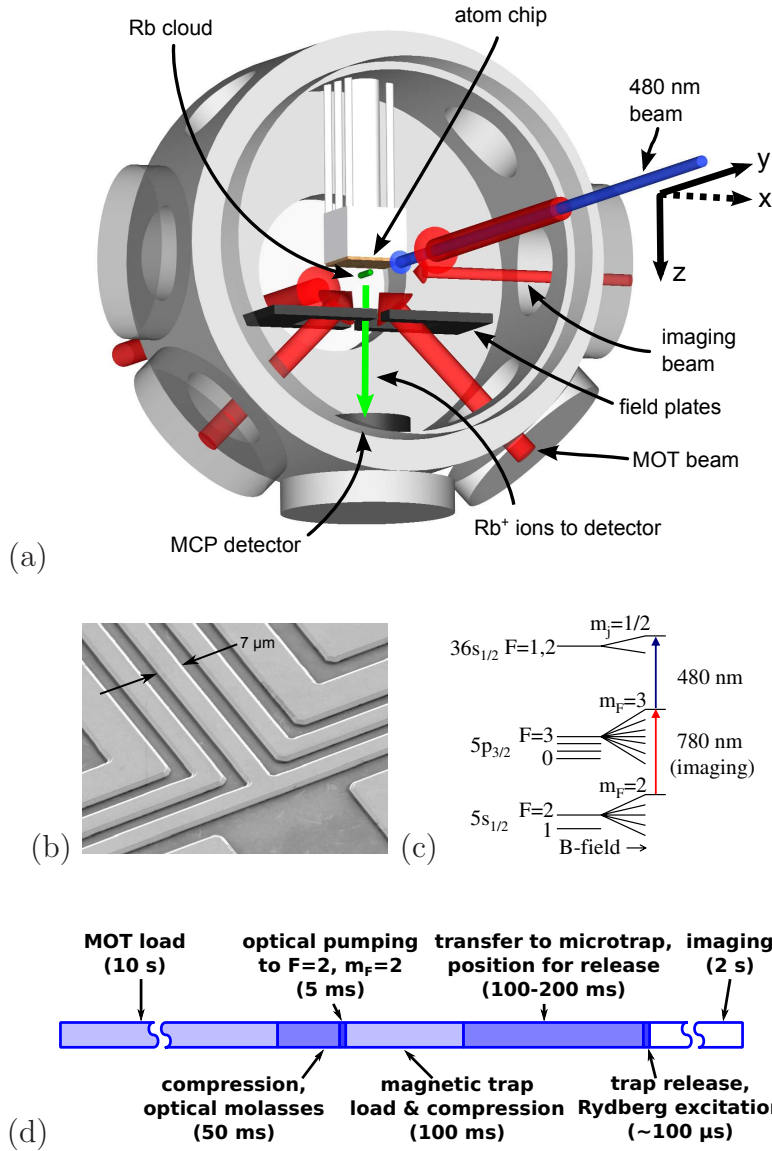


Figure 2.1: (a) Experimental apparatus. (b) Scanning electron microscope image of the atom chip at one end of trapping region, showing wires and insulating gaps. (c) ⁸⁷Rb Rydberg excitation scheme (see for example Ref. [26]). (d) Experimental sequence timing. A single cycle takes ≈ 15 s.

in the gas phase (in plasma diagnostics for example); here we demonstrate that it offers great potential for the measurement of unknown fields near microstructured surfaces.

2.3 Experiment

2.3.1 Summary of techniques

The experimental sequence is shown in Fig. 2.1: atoms are first loaded from background ^{87}Rb vapor into a mirror magneto-optical trap (MOT) [27], compressed, and optically pumped into the $5s_{1/2}, F = 2, m_F = 2$ sublevel. The atoms are trapped by quickly turning on a mm-scale magnetic trap and then adiabatically transferred to the trapping potential formed by the atom chip wires. In this work, the potential minimum is located between $35 - 70 \mu\text{m}$ from the surface of the chip.

We do not trap Rydberg atoms [28, 29] – the atoms are released from the microtrap prior to Rydberg excitation, because inhomogeneous magnetic fields (due to wire currents) and electric fields (due to voltage drops along the wires) broaden the transition and reduce the available signal level.

Atoms are held in the microtrap for periods ranging from $30 - 350 \text{ ms}$ and then released by quickly shutting off the chip wire current. Rydberg excitation is done $30 \mu\text{s}$ after release, when fields due to eddy currents associated with the wire shutoff have dissipated. A homogeneous magnetic field of 34.5 G remains in the x -direction (the microtrap “bias field”). A $30 \mu\text{s}$ long optical pulse excites Rydberg atoms via a two-step process: 1) a $\approx 780 \text{ nm}$ laser tuned to the $5s_{1/2}, F = 2, m_F = 2 \rightarrow 5p_{3/2}, F = 3, m_F = 3$ transition, and 2) $\approx 480 \text{ nm}$ laser light to drive the $5p_{3/2}, F = 3, m_F = 3 \rightarrow 36s_{1/2}$ transition. We study excitation to Rydberg states after release from the microtrap, varying distance by moving the 480 nm beam relative to the surface using servo-actuated mirrors (staying parallel to the surface). The cloud of trapped ground state atoms extends some distance from the surface and expands after release from the microtrap, so that the density of ground state atoms allows detectable Rydberg excitation up to approximately $800 \mu\text{m}$ from the surface.

The Rydberg atoms are detected by selective field ionization (SFI)[13]: a slowly rising ($\approx \mu\text{s}$) negative voltage pulse is applied to the two metal plates away from the chip surface (see Fig. 2.1), creating a field normal to the chip surface. Ionized Rb atoms are drawn towards a microchannel plate (MCP) detector.

In the following subsections we give more specific technical details concerning the techniques employed.

2.3.2 Trap loading

Atoms are first loaded from background ^{87}Rb vapor supplied with dispensers [30] into a mirror magneto-optical trap (MOT) centered 2-3 mm below the chip surface. The quadrupole field is generated by a current-carrying U-shaped structure underneath the chip and external field coils. Typically $10 - 20 \times 10^6$ atoms are loaded in about 10 s.

The cloud is then compressed by increasing the cooling laser detuning to reduce the radiation pressure. After compression, the quadrupole field is ramped down, with the MOT beams left on to slow the expansion of the cloud and damp any acceleration due to transient magnetic field gradients caused by eddy currents. The MOT beams are then turned off and the atoms are optically pumped into the weak field-seeking $F = 2, m_F = 2$ sublevel. The atoms are then confined by quickly turning on a mm-scale magnetic trap formed by a current-carrying z-shaped structure below the chip and external field coils. More than 2/3 of the MOT population can be successfully captured in the magnetic trap. The $1/e$ lifetime of the cloud in this trap is typically 2 – 4 s, consistent with the loss rate due to collisions with room-temperature background gas at a pressure of 10^{-9} Torr. The cloud is adiabatically transferred to the microtrap by ramping up the current in the chip wires and then slowly ramping down the current in the larger wire below the chip. There is some atom loss due to evaporation in this process. The initial population of the chip trap is about 1.5×10^6 and decays exponentially with a time constant of around 500 ms.

2.3.3 Atom chip

The atom chip consists of $1\ \mu\text{m}$ high gold wires deposited on a thin $20\ \text{nm}$ layer of insulating silicon dioxide on a silicon substrate. There are five wires on the chip surface: a central H-shaped structure (connected so that the current runs in a z-shape), and two pairs of nested U-shaped wires. In the $4\ \text{mm}$ long trapping region, the wires are arranged close to each other and run parallel. The three innermost wires are $7\ \mu\text{m}$ wide and the outer wires are $14\ \mu\text{m}$ wide. All wires are separated by gaps of $7\ \mu\text{m}$. The remainder of the $2 \times 2\ \text{cm}$ square chip is covered with a grounded $1\ \mu\text{m}$ layer of gold. The potential created by wire currents and external magnetic field coils has approximate cylindrical symmetry, though field gradients are largest near the chip surface. Details of the fabrication of the atom chip are contained in Cherry *et al.* [31] (see Fig. 3 in this reference for the exact wire geometry).

2.3.4 Optical excitation

The $780\ \text{nm}$ light for cooling and trapping is produced by two external-cavity diode lasers. The $480\ \text{nm}$ light for Rydberg excitation is obtained by frequency doubling a Ti:sapphire laser that is stabilized using a transfer cavity [32].

During Rydberg excitation, the $780\ \text{nm}$ light is introduced in the same way as for absorption imaging (along the x -axis; see Fig. 2.1), whereas the $480\ \text{nm}$ light travels along the long y -dimension of the released cloud, with vertical polarization (z -direction). The $480\ \text{nm}$ light has a beam waist of $w = 30\ \mu\text{m}$ ($1/e$ amplitude radius), and a Rayleigh range of $z_R = 5\ \text{mm}$ (measured using a scanning knife edge). Servo-actuated mirrors, calibrated using a scanning knife edge, are used to steer the $480\ \text{nm}$ beam in order to perform Rydberg excitation at various distances from the chip. Proper alignment of the beam relative to the chip surface is verified by measuring the excited Rydberg population as a function of servo position. This alignment is stable to within $10 - 20\ \mu\text{m}$ day-to-day, and therefore the dominant contribution to uncertainty in the Rydberg atom-surface distance is the finite size of the Rydberg sample, which has a radius of $\approx 30\ \mu\text{m}$ as dictated by the $480\ \text{nm}$ beam waist.

In this work, the two-photon Rydberg excitation is resonant with the intermediate $5p_{3/2}$ state. The observed linewidth of the Rydberg excitation is slightly narrower than the natural linewidth of the $5p_{3/2}$ state (6.0 MHz). Sub-natural linewidth has been observed previously in a similar two-photon excitation process where the intermediate state was coherently pumped with a weak coupling field [33].

By releasing atoms from the MOT and then performing Rydberg excitation at distances far from the chip (4.2 mm), we observe a linewidth of 3.6 ± 0.2 MHz (see Fig. 2(a)). This result was found in both zero magnetic field and in a homogeneous magnetic field of the same magnitude as the microtrap bias field.

2.3.5 Measurement of electric fields

The $36s_{1/2}$ state is red-shifted by electric fields. Therefore, we measure the “average” normal electric field component by blue-detuning the Rydberg excitation laser about half a linewidth from resonance (as illustrated in Fig. 2.2(c)) and varying an applied electric field created by biasing the field plates. Figure 2.2(d) shows signal vs. applied field at three distances from the surface. The signal is maximized when the applied electric field cancels the average electric field near the chip (the fields near the chip are inhomogeneous so this cancellation will not be complete for all locations). We call this value of the applied field the “compensating field”; for a given distance we determine it from the center of a fitted Gaussian.

The Stark shift of the $36s_{1/2} \rightarrow 36p_{1/2}$ microwave transition was used to calibrate the applied compensating electric field in terms of field plate bias voltage (far from the chip surface). This technique was also used to measure fringing fields from the front of the MCP detector (normally held at -1800 V relative to ground, but varied to determine its contribution to the field near the chip). This microwave transition has the advantages of narrower linewidth and a higher electric field sensitivity compared to the optical $5p_{3/2} \rightarrow 36s_{1/2}$ transition.

The $36s_{1/2} \rightarrow 36p_{1/2}$ microwave transition linewidth varies with field plate bias voltage. The observed broadening places an upper bound of 10% on the inhomogeneity of the electric field applied by the plates.

In addition to correcting for the fringing field (1.88 ± 0.09 V/cm), we also corrected variations in the measured electric field due to slowly time-varying fields associated with the ac line — the measured field varies sinusoidally at the ac electrical power line frequency, with an amplitude of 0.24 V/cm. Neglecting the effects of Rb adsorption, we would expect to see a small dc field on the order of 0.1 V/cm due to the work function difference between the gold chip surface and the stainless steel field plates, which are electrically connected by sharing a common ground. However, measurements taken far from the chip surface are consistent with zero field once the above corrections have been applied.

The plot in Fig. 2.3(b) illustrates the day-to-day measurement repeatability. Measurements far from the chip, where the effects of inhomogeneous fields near the surface are small, are quite consistent. At a distance of 3 mm from the surface, the measured fields are reproducible to within 0.04 V/cm. Our estimate of the measurement uncertainty due to detection signal/noise is consistent with this reproducibility (see Section 2.5).

Closer to the chip ($100 - 500 \mu\text{m}$), the measured fields are less reproducible. Measurements taken on the same day under nominally identical conditions are reproducible to within 0.15 V/cm, but the day-to-day variability is larger. The data shown in Fig. 3(b) are consistent with an overall measurement uncertainty of 0.6 V/cm. Therefore, most of the variability in field measurements made close to the surface is in fact due to day to day changes in the surface fields. Further work is required to identify the sources and conditions influencing this variability.

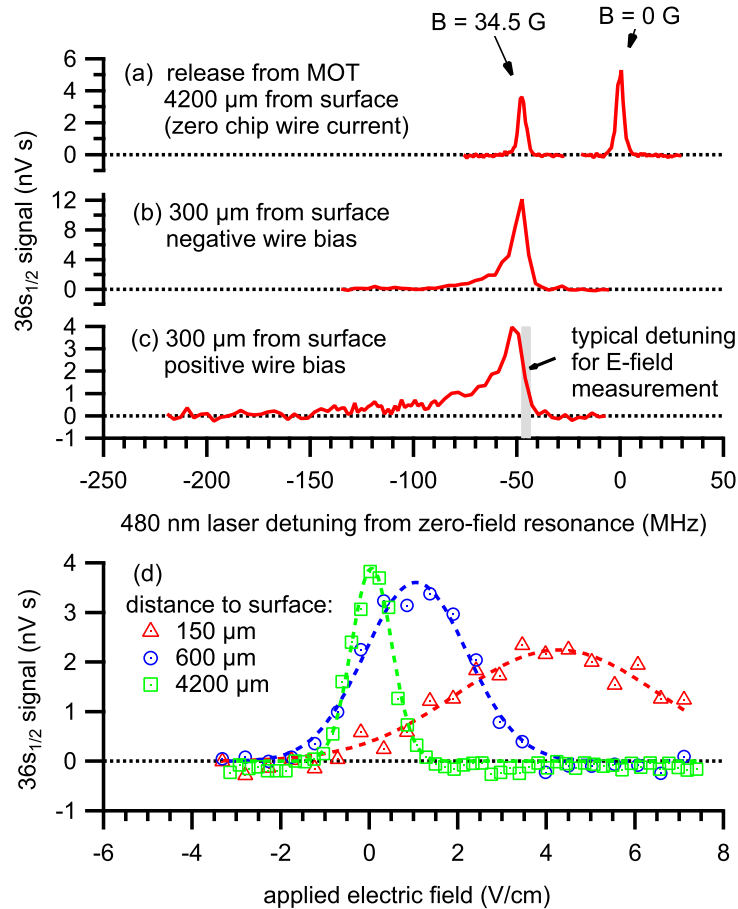


Figure 2.2: Rydberg excitation spectra after release from the (a) MOT (both with and without a magnetic field present), and (b-c) microtrap, with compensating electric fields applied (see text for details of compensation and wire biasing). (d) Measurement of the Rydberg signal as a function of applied electric field (by varying plate voltages, corrected for MCP fringing field and ac line interference; see Section 2.3.5), with Gaussian fits. Positive wire bias (see text) was used for the spectra at 150 μm and 600 μm , whereas the result for the larger distance 4200 μm was obtained by release from the MOT. We refer to the center of the fitted Gaussian (the applied field needed to null out the average electric field present at the atoms) as the “compensating field”.

2.4 Results

Optical spectra for excitation of the $36s_{1/2}$ state (with compensating field applied) are shown in Fig. 2.2(a)-(c). Far from the surface the linewidths are narrow, roughly dictated by the $5p_{3/2}$ radiative lifetime. When the atoms are within about $300\ \mu\text{m}$ from the surface, the optical spectra broaden and become asymmetric. Both effects are caused by Stark shifting due to inhomogeneous electric fields — the $36s_{1/2}$ level shifts quadratically towards lower energy as the field F increases [13]: $\Delta E = -(\alpha/2)F^2$ with $\alpha/2 \approx 2.6\ \text{MHz}/(\text{V}/\text{cm})^2$. For comparison, $\alpha/2 \approx 0.04\ \text{Hz}/(\text{V}/\text{cm})^2$ for the ground state of Rb.

We observe that the voltages of the chip wires during the microtrapping phase significantly affect the electric fields measured after the atoms are released. For typical operating currents, the electrical resistance of a chip wire causes a potential drop of about $6\ \text{V}$ along its length. Since the current supply holds one end of the wire near ground, the wire will have an overall biasing of several volts relative to ground. This biasing varies along the wire’s length and can be positive or negative, depending on whether the supply sources or sinks current. We refer to these conditions as “positive” or “negative wire bias”. Spectra obtained when the chip wires were positively biased consistently show more broadening and lower signal levels compared to negative biasing, even though the magnetic field geometry is identical.

The distance dependence of the measured average compensating field is plotted in Fig. 2.3. There is a dramatic difference between the field magnitudes for the positive and negative wire bias cases. When atoms are released from the microtrap, the scaling of the measured field with distance is consistent with a $1/z$ power law, with fitted power-law scalings of $z^{-0.99\pm 0.3}$ and $z^{-0.93\pm 0.1}$ for negative and positive wire bias, respectively. The electric field direction depends on the wire biasing, consistent with a positive surface charge when the wire potential is negative and vice versa.

This result is surprising. The wire currents are turned off and the wires grounded prior to Rydberg excitation, and so we would expect the surface potential to be the same for both biasing configurations. While the wire potential would decay to ground after shut-off with some characteristic time RC , we expect this time scale to be short compared to the $30\ \mu\text{s}$ delay between wire shut-off and Rydberg excitation. We measured the field

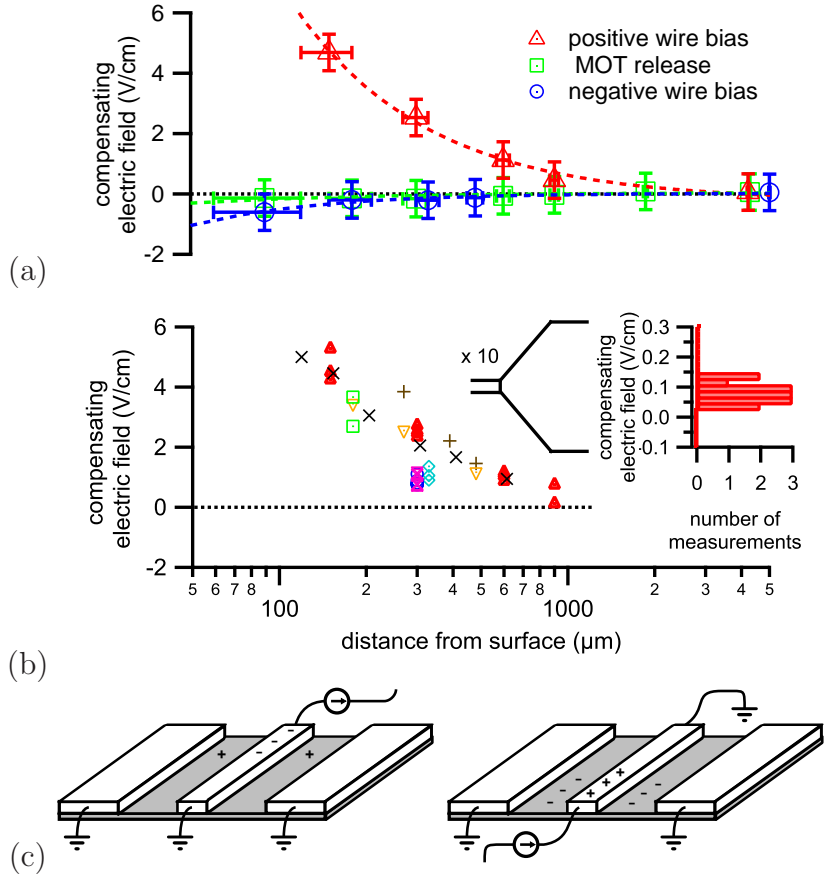


Figure 2.3: (a) Distance dependence of compensating field (corrected for MCP fringing fields and ac line interference; see Section 2.3.5) measured after microtrap release and MOT release, with power-law fits. The horizontal error bars indicate the excitation beam waist $\pm w$ (see Section 2.3.4). (b) Compensating field for positive wire bias, measured at various distances from the chip, taken over 8 different days (represented by different point styles) in a two-month period. In all microtrap measurements in (a)-(b), the atoms were held in the trap for 225 ms prior to release. Inset: histogram of 14 compensating field measurements 3 mm from the surface, taken after release from the MOT, on 13 days in a two-month period. (c) Charge accumulation in the dielectric gaps near a negatively biased wire (left) and positively biased wire (right).

at several different times ranging from 30 – 100 μs after release and found no significant time dependence over this interval. A time constant much longer than 100 μs demands an unreasonably large parasitic capacitance, given the wire resistance of 10 – 20 Ω .

We can use the methods employed to estimate the magnitude of patch fields [8, 9] to model the field created if the chip wires or dielectric gaps between them are not grounded but rather at some well-defined potential V_o with respect to ground. This non-grounded region has some characteristic width w and length ℓ (in our case the dimensions of the wires and gaps between them correspond to $w \approx 90 \mu\text{m}$ and $\ell = 4 \text{mm}$). If we consider the field at some distance z above the chip, such that $\ell \gg z \gg w$, the leading order of the field is normal to the surface and has magnitude $E_z \approx V_o w / \pi z^2$, which is inconsistent with the $1/z$ scaling we observe.

One possibility is that the non-grounded region is wider than the wire pattern (possible in the case of inhomogeneously distributed adsorbates, for example) such that our measurements are taken in the range of $z \approx w$. Thus, higher-order terms would need to be taken into account and the distance scaling of the field would become closer to $1/z$. However, in this regime the scaling of the field varies as a function of z , and our observed $1/z$ scaling appears quite robust over a rather large distance range (from 150 – 900 μm).

If we assume instead that the field is caused by a charge accumulation on the dielectric, with no well-defined potential on the dielectric surface, then in the $\ell \gg z \gg w$ regime we can use a long line charge model, with a charge per unit length given by λ . The field due to this line charge is $E_z = \lambda / (2\pi\epsilon_0 z)$. When the wires are positively biased, the fields we observe are consistent with a total accumulated charge of about 1×10^5 elementary charges, or a charge density of roughly $0.6 e / \mu\text{m}^2$ on the exposed dielectric in the wire gaps.

Thus, a possible explanation for the observed distance scaling and direction of the field is that ambient charged particles are drawn toward oppositely-biased wires, as illustrated in Fig. 2.3(c), and then trapped in the insulating gaps between the wires. They remain there for some time ($> 1 \text{ms}$) even after the chip wires are shut off and the wires are at ground (consistent with the observed lack of time-dependence of the fields after release on the 100 μs timescale). Such a charging mechanism should saturate. This is seen for positively biased wires in Fig. 2.4(a), where the field magnitude depends exponentially on

the amount of time the microtrap wires are turned on before the atoms are released, and at long times approaches a value proportional to the wire current (and thus the biasing potential).

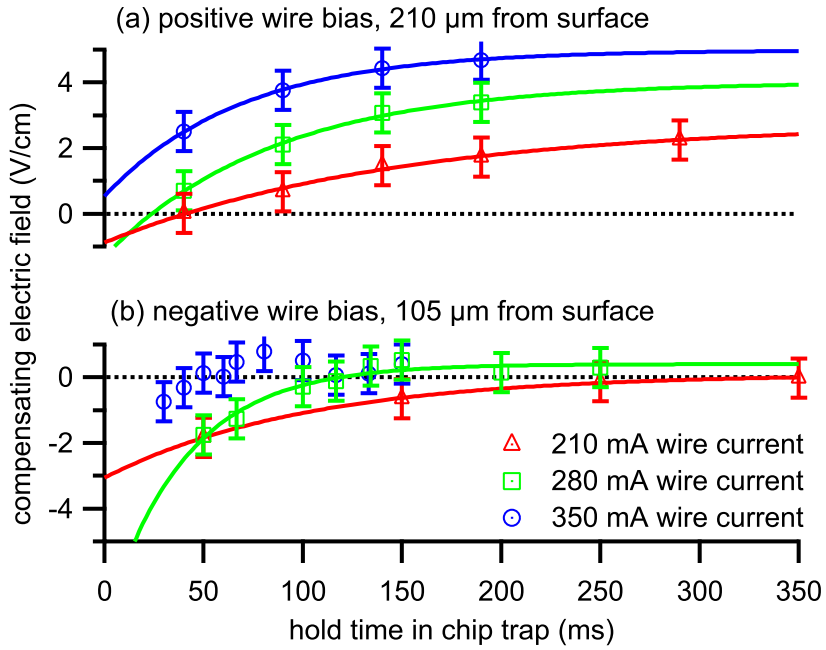


Figure 2.4: Compensating field as a function of hold time in microtrap together with exponential fits, (a) positive wire bias, Rydberg excitation 210 μm from surface. (b) negative wire bias, Rydberg excitation 105 μm from surface.

In this explanation there is a natural asymmetry between the positive and negative biasing cases due to the differing mobilities and trapping of oppositely signed charges. Our observations suggest that it is easier to attract an excess of negative charge into the insulating gaps between the wires, than it is to repel electrons from, or draw positive ions towards this region. When the wires are negatively biased, we do not observe charge accumulating over time. Instead, the gaps appear to have a significant net positive charge shortly after the wires are turned on, and the charge neutralizes as the wires operate. The rate of neutralization depends strongly on wire current (see Fig. 2.4), suggesting a thermally activated neutralization mechanism, as wire temperature increases with current.

Charge transfer between the dielectric surface and the semiconducting substrate — which is in contact with current-carrying metal structures below the chip — is one possible explanation for the initial charging in this case. Excess charge in silicon dioxide films and interfaces has previously been observed, and is important for semiconductor devices [34].

When atoms are released from the MOT, rather than the microtrap, the measured field direction is consistent with a small positive charge on the surface. However, the magnitude is smaller than when atoms are released from the microtrap, and has a weaker distance dependence, with $1/z^{0.67\pm 0.2}$ scaling. Turning on the chip wires while the atoms are trapped in the MOT (rather than the microtrap) has no effect on the measured electric field after release, a result which is inconsistent with a slowly-relaxing dielectric polarization as an explanation for the fields [7].

The field direction in the negative wire bias case is consistent with Rb deposited preferentially near the center of the chip [35], and the distance scaling we observe is similar to Ref. [18]. However, the fields we observe are an order of magnitude smaller and do not change when we deposit Rb on the surface by deliberately moving the cloud close to the chip (we deposited about half the cloud’s population of 1×10^6 atoms in an area roughly $4 \text{ mm} \times 100 \mu\text{m}$, approximately every 15 s for about an hour). Adsorbate fields are considered to be a significant problem for Rydberg atom surface studies [36]. Our diminished adsorbate field is encouraging for the study of intrinsic Rydberg atom surface phenomena, such as the Lennard-Jones shift [37] (using chips with an electrostatic shield between the wires and atoms [18]).

2.5 Electric field measurement uncertainty

Fluctuations in the detected signal limit the precision of electric field measurements as follows. Consider an atomic transition, with maximum signal S_o at the resonant frequency f_o , and a linewidth Γ , with the atoms in an electric field F . If the electric field is changed by a small amount, as illustrated in Fig. 2.5, the Stark shift changes the transition energy. Therefore, the observed signal will change (with the excitation frequency kept constant)

according to

$$\frac{dS}{dF} = \left(\frac{dS}{df_o} \right) \cdot \left(\frac{df_o}{dF} \right), \quad (2.1)$$

where the first factor is determined by the line shape and detuning of the excitation frequency from resonance, and the second factor by the Stark shift.

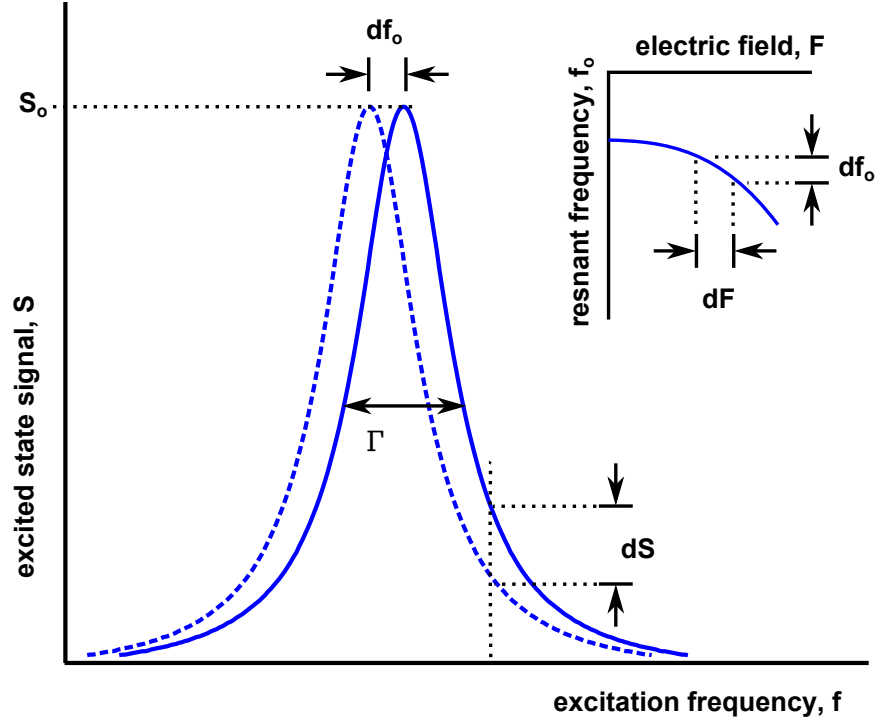


Figure 2.5: A small change dF in the electric field shifts the transition by some amount df_o , via the Stark shift. This changes the measured signal level by dS .

If a single measurement of the excited state signal has some uncertainty δ_S (perhaps due to detector noise), then the measurement of the local field (by varying the compensating field) has an uncertainty on the order of

$$\delta_F \approx \frac{\delta_S}{(dS/dF)\sqrt{N}}, \quad (2.2)$$

where N is the number of measurements. Therefore, maximum measurement precision occurs under conditions where (dS/dF) is maximum.

If the line shape is Lorentzian, the maximum possible magnitude for the first factor in Eq. 2.1 is

$$\frac{dS}{df_o} = \frac{1.30S_o}{\Gamma}, \quad (2.3)$$

when the excitation frequency is detuned by $\Gamma/(2\sqrt{3}) \approx 0.29\Gamma$ from resonance. The numerical factor depends only slightly on the line shape—for example, if the line shape is Gaussian (perhaps because of broadening in an inhomogeneous field) then the numerical factor is 1.43.

If the Stark shift is quadratic, $\Delta E = -(\alpha/2)F^2$ and the maximum possible precision of the field measurement (with optimal excitation frequency) for a given set of experimental conditions is

$$\delta_F \approx \frac{\Gamma}{1.30S_o\alpha F} \frac{\delta_S}{\sqrt{N}}. \quad (2.4)$$

This result is useful for estimating the measurement uncertainty in situations where the applied field and linewidth are both known.

In addition, Eq. 2.4 qualitatively shows how the measurement precision can be improved by increasing the field and using highly polarizable states with long lifetimes. However, if the field is not completely homogeneous, the transition will start to broaden as the polarizability and applied field increase. Therefore, the linewidth Γ and maximum signal S_o depend on the polarizability, applied field, and field inhomogeneity.

To estimate the ultimately achievable precision, the effects of field inhomogeneities must be considered. Due to the Stark effect, a field inhomogeneity ΔF will cause an additional contribution to the linewidth, given by

$$(\Delta\Gamma) = \alpha F(\Delta F) + \frac{\alpha}{2}(\Delta F)^2. \quad (2.5)$$

The second term is important only for large field inhomogeneity, such that the transition is significantly broadened when the average field F is zero. If we assume that this broadening adds in quadrature with γ , the linewidth in the limit of highly homogeneous field, then

$$\Gamma^2 = \gamma^2 + (\Delta\Gamma)^2. \quad (2.6)$$

This additional broadening also shifts some of the population out of resonance with the excitation, reducing S_o :

$$S_o = \frac{S_H \gamma}{\Gamma}, \quad (2.7)$$

where S_H is the maximum signal when the field is highly homogeneous.

Explicitly including the effects of the field inhomogeneity, we modify Eq. 2.4:

$$\delta_F = \frac{\gamma^2 + (\Delta\Gamma)^2}{1.30\gamma\alpha F} \cdot \frac{\delta_S}{S_H\sqrt{N}}. \quad (2.8)$$

The minimum uncertainty for a given polarizability α and field inhomogeneity Δ_F is found by optimizing the applied field F .

In the limit of small inhomogeneity, $\alpha(\Delta F)^2 \ll \gamma$, the first term in Eq. 2.5 dominates, and the minimum uncertainty is

$$\delta_F = \frac{2(\Delta F)}{1.30} \cdot \frac{\delta_S}{S_H\sqrt{N}}. \quad (2.9)$$

In this limit, the optimal field is $F = \gamma/\alpha\Delta F$, at which point the broadening due to field inhomogeneity is equal to the natural linewidth, i.e., $\Delta\Gamma = \gamma$. This ultimate limit is independent of γ and α . However, narrow linewidth and large polarizability allow the condition for maximum sensitivity to be achieved with a reasonably small applied field.

If the field inhomogeneity is large, such that $\alpha(\Delta F)^2 \gg \gamma$, the second term in Eq. 2.5 dominates. The minimum uncertainty achievable in these conditions is

$$\delta_F = \frac{2(\Delta F)}{1.30} \cdot \frac{\alpha(\Delta F)^2}{\gamma} \cdot \frac{\delta_S}{S_H\sqrt{N}}, \quad (2.10)$$

a factor of $\alpha(\Delta F)^2/\gamma$ larger than the small-inhomogeneity limit of Eq. 2.9. In this case, the measurement sensitivity could actually be improved by using states with smaller polarizabilities.

Equation 2.4, in combination with the data shown in Fig. 2.3, can be used to estimate the effects of field inhomogeneity and detection noise in our experiment. For example, when measuring the field several mm away from the chip surface, the maximum of dS/dF occurs at $F \approx 0.5$ V/cm. The polarizability of the $36s_{1/2}$ Rydberg state is $\alpha = 5.2$ MHz/(V/cm)².

Under these conditions, the linewidth is typically $\Gamma = 4$ MHz, the signal/noise ratio $\delta_s/S_o \approx 0.1$ and we make $N \approx 60$ measurements in the region of reasonably large dS/dF . The estimated measurement uncertainty under these conditions is therefore $\delta_F \approx 0.015$ V/cm, a figure reasonably consistent with the measured repeatability of 0.04 V/cm. The resonance is not significantly broadened by field inhomogeneities, so measurement precision could potentially be improved by the use of larger fields or states with higher polarizabilities.

Close to the chip, inhomogeneous fields broaden the linewidth to $\Gamma \approx 20$ MHz, and the longer duty cycle associated with loading atoms into the chip trap reduces the typical number of measurements to $N \approx 15$. The signal/noise ratio is similar to the MOT release case, and the maximum of dS/dF occurs at $F \approx 2$ V/cm. The estimated measurement uncertainty under these conditions is $\delta_F \approx 0.04$ V/cm. This estimate is smaller than both the observed day-to-day repeatability of 0.6 V/cm and the intra-day repeatability of 0.15 V/cm. However, this model does not take into account any time-variation of the fields so the discrepancy is hardly surprising. The transition is broadened significantly even at zero field, so in this case measurement precision could be improved by using an excited state with lower polarizability.

2.6 Summary and outlook

In summary, we have performed Rydberg atom sensing of electric fields near a microstructure consisting of gold wires and insulating gaps. We have observed an electric field due to charge accumulation in the gaps between the wires. The magnitude and direction of this field depend on the voltage biasing of the chip wires with respect to the surrounding grounded surfaces during operation of the microtrap. Therefore, appropriate choice of voltage biasing (negative with respect to ground) can dramatically reduce this charging.

The quantitative behavior we have observed is for a specific geometry, but our measurement approach and the influence of biasing are quite general. For example, recent experiments by Hogan *et al.* [5] involving Rydberg atoms close to a co-planar waveguide may also benefit from the type of dc biasing (inner conductor negative with respect to ground) found to minimize charging in our experiment. Although we have exploited the high sen-

sitivity of Rydberg atoms to measure electric fields, cold ground-state atoms [38, 35] and molecules [6] also exhibit sensitivity to electric fields, and similar biasing considerations apply.

In the future, our demonstration of selective-field-ionization near the chip can be extended to state-sensitive detection of Rydberg atoms, enabling the use of microwave transitions between Rydberg states for noise spectroscopy [39] near the chip surface. This would establish limits on the coherent manipulation of Rydberg atoms near atom chips due to electric field noise [12] and help test surface noise models [40].

We thank R. Mansour for use of the CIRFE facilities, J. B. Kycia for the loan of equipment, and C. E. Liekhus-Schmaltz for comments on this manuscript. This work was supported by NSERC.

Chapter 3

Theoretical background and ac electric field measurement techniques

3.1 Introduction

This chapter contains the theoretical background necessary to measure slowly varying ac electric fields with noise power spectra of the form $1/f^\kappa$ using Rydberg atoms. Electric field noise near surfaces is a subject of interest for microfabricated ion-trap research, because such field noise causes motional heating of the ions and leads to decoherence. A summary of noise measurements and theoretical microscopic models for the origin of the field noise from ion-trap literature is presented.

I discuss the detection of field noise using the dephasing of Rydberg atoms, adapting to Rydberg atom experiments the techniques of spin-echo and spin-locking. These techniques were originally developed to preserve coherence in nuclear magnetic resonance (NMR) experiments and have more recently been extended to measure noise in NMR and solid-state qubits. I review the analytical theory in the literature for calculating decoherence rates given a known noise spectral density for linear coupling and, for pure $1/f$ noise ($\kappa = 1$), quadratic coupling to the field noise. The theory of coherent manipulation

of Rydberg atoms using microwaves resonant with one- and two-photon transitions is also reviewed.

I extend the calculations for dephasing in the regime of quadratic stark shifts beyond the $\kappa = 1$ case using Monte Carlo simulation to determine dephasing rates for $\kappa = 1/2, 1$, and $3/2$. A method for Monte Carlo simulation of the time-evolution of the atomic density matrix is also discussed (results of the calculations are presented in chapter 4). Finally, an estimate of the ultimate sensitivity of noise measurements with Rydberg atoms is presented.

3.2 Ion traps

Electric field noise near metal surfaces is a subject of interest due to its role in “anomalous” heating of the microscopic of the motion of ions confined by microfabricated ion traps, with typical ion-electrode separations on the order of $30 - 300 \mu\text{m}$ [10, 41]. The heating is called “anomalous” because the microscopic mechanism responsible is not known [11].

Trapped ions have the potential to be used as qubits in quantum computers [42]. However, uncontrolled motion of the trapped ions due to the heating causes errors in the implementation of two-qubit logic gates, which has impeded improvements to the scalability and miniaturization of devices using trapped ions for quantum computing [11].

The heating is caused by electric field noise in the following way. Electric field noise near the trap’s mechanical oscillation angular frequency, ω , drives motion of the ion. The relationship between electric field noise spectral density $S_F(\omega)$ and the heating rate, $\dot{\bar{n}} \equiv d\bar{n}/dt$ is given by [41]

$$S_F(\omega) = \frac{4m\hbar\omega}{q^2}\dot{\bar{n}}, \quad (3.1)$$

where \bar{n} is the average number of motional quanta of the ion, m is the mass of the ion, and q is the charge of the ion. Therefore, measurements of the heating rate of an ion in the trap can be used as a sensitive probe of the electric field noise near the electrode.

The field noise spectral density depends on both the frequency and the distance between the ion and the surface of the trap electrodes. In most measurements of ion-trap heating rates, the frequency scaling of S_F is approximately $S_F(\omega) \propto 1/\omega$, such that $\omega S_F(\omega)$ can

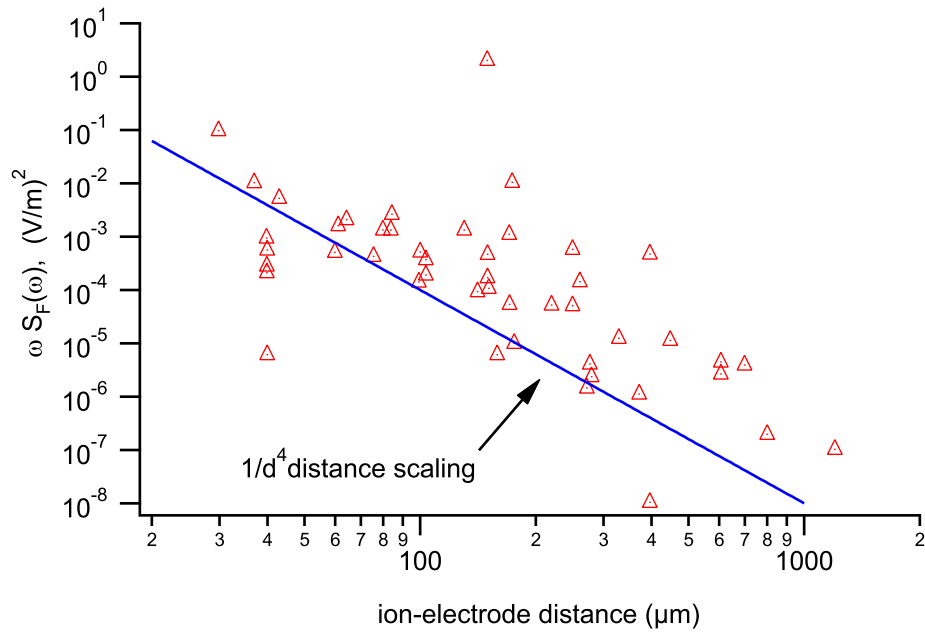


Figure 3.1: (cf. Fig. 5 in Ref. [11] and Fig. 5 in Ref. [10]) Electric field noise figure of merit $\omega S_F(\omega)$ vs. ion-electrode distance for various room-temperature ion trap measurements in the literature. For comparison, the $1/d^4$ distance dependence predicted by most patch-field models is shown as a line.

be used as a figure of merit when comparing traps with different mechanical resonance frequencies. The scaling of S_F with distance, d , to the surface is observed to be approximately $S_F(\omega) \propto 1/d^4$. Data compiled in Refs. [10, 41] are shown in Fig. 3.1.

3.2.1 Surface noise

Several recent experiments provide evidence that the electric field noise causing ion heating is likely associated with surface contamination. Wang *et al.* [43] fabricated ion traps with superconducting niobium electrodes and saw no change in the ion motional heating rate as the wire temperature was taken through the superconducting transition. They interpret this result as suggesting that the phenomenon responsible for anomalous heating is a surface, rather than bulk, effect. Hite *et al.* [11] reported that cleaning the electrodes with argon-ion bombardment reduced the amount of surface contamination and also reduced electric field spectral noise density by about two orders of magnitude following the cleaning. Daniilidis *et al.* [10] measured ion motional heating rates at various positions along their microtrap and found that the heating rate varied with position and was largest at the location where ions were loaded. They attribute this result to local changes in the chemical composition of the electrodes due to bombardment by electrons, ions, or the laser photons used to ionize the calcium atoms used in their experiment.

3.2.2 Noise models

The underlying mechanism causing electric field noise near metal surfaces is not entirely clear. However, the distance scaling of $S_F(\omega)$ can be used to eliminate some proposed mechanisms from consideration. Turchette *et al.* [41] calculated that heating caused by Johnson noise due to the finite resistivity of the electrodes would have a distance scaling of $S_F(\omega) \propto 1/d^2$, which is inconsistent with experimental results. Instead, the observed $1/d^4$ distance dependence for heating is consistent with a model consisting of fluctuating patch potentials on a spherical surface surrounding the ion. Dubessy *et al.* [44] considered an infinite planar surface, with fluctuating patches having a correlation length scale ζ . The distance scaling of the heating rate depends on the relative magnitudes of d and ζ , with a

$1/d^4$ scaling of the heating rate far from the surface ($d \gg \zeta$) smoothly transitioning to a $1/d$ scaling close to the surface ($d \ll \zeta$). Low *et al.* [24] calculated the distance dependence for a number of relevant electrode geometries. In general, the distance scaling of $S_F(\omega)$ depends on the geometry and field direction, as well as the relative magnitudes of d and ζ . However, for several typical ion trap geometries the heating rate was calculated to scale as $1/d^4$ far from the surface. In principle, if the length scale of the potential variations is large enough, the change in distance scaling of $S_F(\omega)$ near the surface could be used to characterize the length scale of the potential variations.

Likewise, the measured frequency scaling of $S_F(\omega)$ can be used to discriminate between different microscopic models. In one model, known as the “surface-diffusion model” [45, 46], contaminants adsorbed on the surface are polarized, creating electric dipoles. Over time, the adsorbates diffuse across the surface, causing the potential near the surface to change and creating ac electric fields near the surface. This diffusion has a natural time scale given by $\tau_d = d^2/4D$, where D is the diffusion coefficient for adsorbates on the surface and d is the atom-surface distance (which sets the length scale on the surface over which the presence of adsorbates is relevant). In the high-frequency limit of $\omega \gg 2\pi/\tau_d$, the electric field spectral density scales as $S_F(\omega) \propto 1/\omega^{3/2}$. Typical values for D appear to be on the order of $10^{-3} \text{ cm}^2/\text{s}$ for atoms physisorbed on room-temperature metal surfaces [47], corresponding to $\tau_d \approx 1 \text{ s}$ for d on the scale of tens of μm . Thus the high-frequency limit applies at typical ion-trap frequencies in the 0.1 MHz – 10 MHz range.

In another model proposed by Safavi-Naini *et al.* [40], adsorbed contaminants also create electric dipoles on the surface. However, these contaminants are assumed to not diffuse across the surface—they are bound to one location by a potential that is attractive (van der Waals) at long distances but repulsive at short distances. This potential has a number of possible bound vibrational states. Due to the asymmetric shape of the potential, the adsorbate-surface distance, and thus the induced dipole moment, depend on the vibrational state. While vibrational frequencies are on the order of THz for typical adsorbates, phonons in bulk material cause transitions between different vibrational states at MHz rates. At low frequencies, this model predicts that $S_F(\omega)$ is independent of ω , while at high frequencies $S_F(\omega) \propto 1/\omega^2$. In an intermediate frequency regime, predicted to be around 10 – 100 MHz for typical adsorbates on gold, $S_F(\omega)$ scales approximately as $1/\omega$. More recently, the

theory has been extended to show that a monolayer of adsorbates on the surface can change the magnitude of the field noise due to these dipoles, though the essential features of the frequency scaling are unchanged [48].

Henkel and Horovitz [49] have proposed a third model, where ac electric fields near the surface are due to the motion of charges, either on the surface or in the bulk of the metal. The skin depth, δ , of the metal sets a length scale for the problem. Far from the surface ($d \gg \delta$), the leading term of $S_F(\omega)$ has a $1/d^2$ scaling, as expected from Johnson noise. However, diffusion of charge across the surface leads to a correction term with a $1/d^4$ scaling. The magnitude of charge diffusion is not well characterized, but assuming this diffusion term dominates (as it must to explain the experimentally observed $1/d^4$ distance scaling of $S_F(\omega)$) this model predicts that $S_F(\omega) \propto 1/\omega^{1/2}$.

As ion traps are only sensitive to noise near the mechanical oscillation frequency of the ion, their use as ac field detectors is limited to a fairly narrow frequency range (typical frequencies are in the range of 100 kHz \rightarrow 10 MHz). The limited frequency range of measurements can make it difficult to determine which (if any) of the models described in this section accurately capture the details of the underlying microscopic phenomenon responsible for the noise.

In particular, the limited frequency range of measurements makes it difficult to evaluate the accuracy of the model of Safavi-Naini *et al.* [40] in which frequency scaling of $S_F(\omega)$ changes significantly with increasing frequency. Therefore, it is desirable to develop a complementary method of electric field noise measurement which is sensitive to a larger frequency range than may conveniently be observed with ion traps.

3.3 Noise spectroscopy with free evolution Rydberg state superpositions

3.3.1 Introduction

Coherence between states of a quantum system is quite easily destroyed in the presence of environmental noise; this is to say that under the right circumstances a quantum system can serve as a sensitive probe of noise in the surrounding environment.

Control techniques originally developed in NMR [50] and more recently extended to other two-level quantum systems or qubits (see Ref. [39] and references therein) have been used to extend the coherence times of these qubits. It has been recognized that these decoupling sequences act as a frequency filter on the noise [39], so that by systematically changing the decoupling sequence and observing the effect on decoherence it is possible to measure the power spectral density of the noise. Noise measurements of this type have already been done, for example, to measure diffusion through porous media in NMR [51], noise in solid state qubits [52, 39], and ac magnetic fields interacting with electron spins in diamond nitrogen-vacancy defects [53].

Because Rydberg atoms are highly sensitive to electric fields, extending the coherent control techniques discussed above to a coherent superposition of two Rydberg states has the potential to allow sensitive measurement of electric field noise. Pulsed refocusing sequences using reversal of dc electric fields have been used to extend coherence times of Rydberg atoms [54, 55] but so far these sequences have not been used to measure environmental noise with Rydberg atoms. In the rest of this section previous calculations of decoherence in the presence of $1/f$ noise, mostly published in the context of solid-state qubits, will be extended to Rydberg atoms.

3.3.2 Free evolution with linear coupling to noise

Electric field noise may be measured via its effect on a coherent superposition of two Rydberg states (here labelled $|i\rangle$ and $|f\rangle$) during free evolution, as may be measured in a

Ramsey or spin-echo experiment (see, for example, Ref. [50]). Fluctuations in the electric field change the transition energy $\hbar\omega_{if}$ via the Stark shift. These fluctuations are reflected in the accumulated phase of the superposition $\phi(t) = \langle\omega_{if}\rangle t + \delta\phi(t)$ (here I assume that the fluctuations are slow enough that the process is adiabatic). In each realization of the experiment, the field fluctuations will be different, so that $\delta\phi(t)$ is different in each realization and the superposition will dephase. (Realizations may be separated in space, as each experimental shot is performed on an ensemble of Rydberg atoms, or in time, as multiple shots are averaged to produce a signal).

If all the population is initially in state $|i\rangle$, a coherent $\pi/2$ rotation about the x -axis of the Bloch sphere creates a superposition of $|i\rangle$ and $|f\rangle$. The system is allowed to evolve for some time t , and a second coherent $\pi/2$ rotation around the x -axis is applied, followed by a measurement of the populations of state $|i\rangle$ and $|f\rangle$. The procedure is shown in Fig. 3.2.

The final populations depend on the dephasing $\langle\exp[i\delta\phi(t)]\rangle$. In the absence of dephasing, $\langle\exp[i\delta\phi(t)]\rangle = 1$ and the entire population is transferred to state $|f\rangle$. If the dephasing is complete the Bloch vector has no preferred direction ($\langle\exp[i\delta\phi(t)]\rangle = 0$) and the populations of the two states will be equal following the second $\pi/2$ pulse. Therefore, the dephasing can be inferred from the relative populations of the two states:

$$\langle e^{i\delta\phi(t)} \rangle = \frac{p(f) - p(i)}{p(f) + p(i)}. \quad (3.2)$$

In the Bloch-Redfield theory of two-level systems [56, 57], two processes contribute to the loss of coherence. Relaxation of the populations of $|i\rangle$ and $|f\rangle$ toward thermal equilibrium cause longitudinal relaxation, which is exponential with a rate $\Gamma_1 = 1/T_1$. For Rydberg atoms, the mechanisms associated with relaxation include spontaneous emission and coupling to microwave-frequency blackbody radiation of the 300 K environment. The second process is the pure dephasing described above, caused by fluctuations in the energy separation of $|i\rangle$ and $|f\rangle$. The dephasing is also exponential, with a rate Γ_ϕ , so that the total rate of coherence decay (known as the transverse relaxation rate) is $\Gamma_2 = \Gamma_1/2 + \Gamma_\phi$ [50].

When the noise source λ responsible for dephasing is $1/f$, with the power spectrum diverging at $\omega = 0$, the Bloch-Redfield theory does not apply [52]. The decoherence due to pure dephasing is a non-exponential function, $\langle\exp[i\delta\phi(t)]\rangle = f_z(t)$, and the total rate

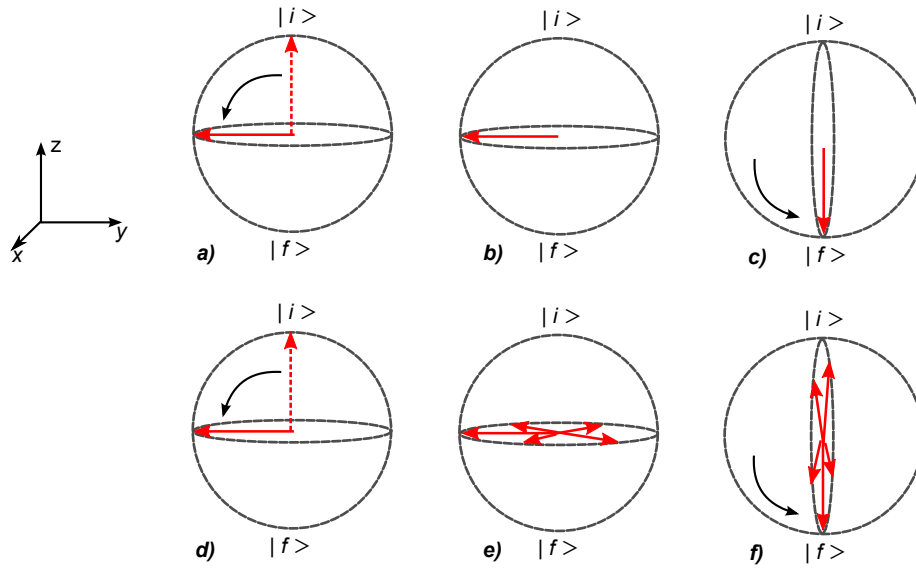


Figure 3.2: Bloch-sphere representation of a Ramsey sequence. a) The population is initially in state $|i\rangle$, and a $\pi/2$ rotation about the x -axis creates a superposition of $|i\rangle$ and $|f\rangle$, initially along the y -axis. b) the superposition is allowed to evolve freely; any noise will cause dephasing as the phase accumulates at different rates in different realizations. c) A second $\pi/2$ rotation projects the y -axis back onto the z -axis, so the dephasing may be inferred from the relative populations of $|i\rangle$ and $|f\rangle$. d)-f): The same sequence as in a)-c), with large amounts of dephasing.

of coherence decay takes the form $\exp[-\Gamma_1 t]f_z(t)$ [52]. The contribution of dc and low-frequency parts of the dephasing can be reduced via Hahn spin-echo, in which a π rotations is applied between the two $\pi/2$ pulses [58], or multiple π rotations such as the CP and CPMG sequences (after Carr, Purcell, Meiboom and Gill [59, 60]), with additional evenly spaced π -rotations around the x and y -axes, respectively (the principal advantage of the CPMG sequence is lower sensitivity to errors in the rotations [39]). The dephasing $f_z(t)$ will depend on the nature of the pulse sequence [52]:

$$f_z(t) = \left\langle \exp \left[i \frac{\partial \omega_{if}}{\partial \lambda} \int_0^t d\tau G(\tau) \lambda(\tau) \right] \right\rangle, \quad (3.3)$$

where $G(\tau)$ is a gating function determined by the timing of the refocusing pulses. During free evolution, $G(\tau) = \pm 1$, with the sign changing at each π pulse (pulses are assumed to be infinitesimally short). For example, a Ramsey experiment (with no refocusing pulses) will simply have $G(\tau) = 1$ at all times, and a Hahn spin-echo experiment with total free evolution time t will have a single π -pulse at $t/2$, and thus $G(\tau < t/2) = +1$ and $G(\tau > t/2) = -1$.

If λ is assumed to have Gaussian statistics and power spectral density $S_\lambda(\omega)$, the dephasing is given by Eq. (2) in Bylander *et al.* [39]:

$$f_z(t) = \exp \left[-\tau^2 \left(\frac{\partial \omega_{if}}{\partial \lambda} \right)^2 \int_0^\infty d\omega S_\lambda(\omega) g_N(\omega, \tau) \right]. \quad (3.4)$$

Here, τ is the total free evolution time of the superposition, and N is the number of π -pulses. The filter function g_N depends on the number and timing of the π -pulses, and is given by (cf. Eq. (3) in Ref. [39])

$$g_N(\omega, \tau) = \frac{1}{(\omega\tau)^2} \left| 1 + (-1)^{1+N} e^{i\omega\tau} \right. \quad (3.5)$$

$$\left. + 2 \sum_{j=1}^N (-1)^j e^{i\omega\delta_j\tau} \cos(\omega\tau_\pi/2) \right|^2, \quad (3.6)$$

where τ_π is the length of each π -pulse. Therefore, the total length of the pulse sequence is $\tau + N\tau_\pi$. The normalized position of the center of the j th π -pulse is $\delta_j = t_j/(\tau + N\tau_\pi)$.

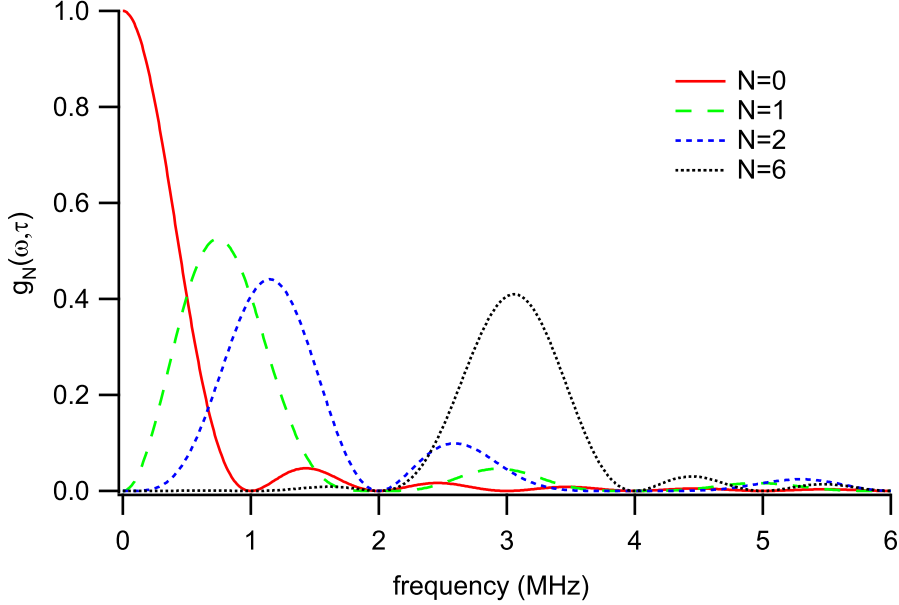


Figure 3.3: Filter function $g_N(\omega, \tau)$ for CP and CPMG sequences with various N , with the x -axis frequency units $f = \omega/2\pi$. Note that $N = 0$ corresponds to the Ramsey sequence and $N = 1$ to the Hahn spin-echo. For the calculations in this plot, $\tau = 1 \mu\text{s}$ and the pulses are assumed to be infinitesimally short ($\tau_\pi = 0$).

Plots of $g_N(\omega, \tau)$ for the CP and CPMG sequences for various N are shown in Fig. 3.3 (g_N is the same for both sequences). For $N > 0$ the effect of noise near dc is completely removed by the refocusing pulses, and the center frequency of $g_N(\omega, \tau)$ increases as pulses are added with τ kept fixed.

If ω_{if} shifts linearly with field, then writing the dephasing in terms of $S_F(\omega)$ is straightforward— F is simply the noise source λ , so that

$$\langle \exp[i\delta\phi(t)] \rangle = \tau^2 \left(\frac{\partial\omega_{if}}{\partial F} \right)^2 \int_0^\infty d\omega S_F(\omega) g_N(\omega, \tau). \quad (3.7)$$

Linear Stark shifts occur for high angular momentum Rydberg states (as well as all states of hydrogen). Even Rydberg states that shift quadratically in F can be made approximately

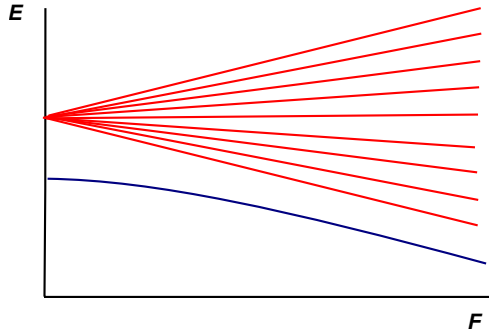


Figure 3.4: Sketch of energy vs. dc electric field for a Rydberg state with a quadratic Stark shift (blue) and the Stark manifold (red) of high angular-momentum states with linear Stark shifts. When dc fields are applied, the sensitivity $\partial E/\partial F$ increases for states with quadratic shift.

linear in their response to field noise with application of a sufficiently large dc electric field, as illustrated in Fig. 3.4. Applying a dc field in this case has the additional advantage of increasing the sensitivity of ω_{if} to changes in F .

3.3.3 Free evolution with quadratic coupling to noise

In zero dc electric field, the leading order of the Stark shift is quadratic for low-angular momentum Rydberg states. Elimination of first-order sensitivity to noise is desirable for maintaining coherence (consider, for example, the optimal working point of quantonium, where the biasing parameters are selected to eliminate first-order dependence [61]). When the goal is to *measure* field noise, reducing the sensitivity to noise by eliminating the first-order sensitivity may seem like a counter-intuitive strategy. However, when measuring large amounts of field noise using Rydberg atoms it may be desirable to reduce the sensitivity by working in zero dc field so that measurements may be conducted at higher n . This may be done to allow for longer Rydberg state lifetimes or smaller microwave transition frequencies between the states in the superposition, for example.

When the leading order of the coupling of transition energy to the noise source λ is quadratic, calculating the decoherence rate due to noise requires knowledge of the statistics of λ^2 , including not only the power spectral density $S_{\lambda^2}(\omega)$ but also higher orders in the statistics of λ^2 [62]. The need for higher orders is because of the non-linear coupling to the noise—even if λ obeys Gaussian statistics, fluctuations in the phase of the superposition do not because of the non-linear coupling.

Because the decoherence rate depends on the power spectral density of F^2 , $S_{F^2}(\omega)$, it is necessary to determine the relationship between $S_{F^2}(\omega)$ and $S_F(\omega)$ in order to extract information about $S_F(\omega)$ from measurements of decoherence. I first seek to determine $S_{F^2}(\omega)$ in terms of $S_F(\omega)$ by expanding $F(t)$, measured over some time interval $0 \leq t \leq T$, as the sum of random Fourier components (cf. Kubo *et al.*, Eq. [1.3.11]) [63]:

$$F(t) = \sum_{j=-\infty}^{j=\infty} a_j e^{i\omega_j t}. \quad (3.8)$$

The angular frequencies are $\omega_j = 2\pi j/T$, with spacing $\delta\omega = 2\pi/T$. Since $F(t)$ is real, the amplitude coefficients are constrained by $a_{-j} = a_j^*$. In the limit of $T \rightarrow \infty$ (or equivalently, $\delta\omega \rightarrow 0$), one may transform from discrete to continuous notation, expressing $S_F(\omega)$ in terms of a_j :

$$S_F(\omega_j) = \lim_{\delta\omega \rightarrow 0} \frac{1}{\delta\omega} \langle |a_j|^2 \rangle, \quad (3.9)$$

with $|a_j|$ determined by the power spectrum. Each Fourier component has a random phase so the complex amplitudes are written as $a_j = |a_j| \exp[i\phi_j]$.

One may write the square of the field as

$$|F(t)|^2 = \left(\sum_{k=-\infty}^{k=\infty} a_k^* e^{-i\omega_k t} \right) \left(\sum_{j=-\infty}^{j=\infty} a_j e^{i\omega_j t} \right), \quad (3.10)$$

which I will attempt to rewrite in the form

$$|F(t)|^2 = \sum_{\ell=-\infty}^{\ell=\infty} b_\ell e^{i\omega_\ell t} \quad (3.11)$$

in order to determine the power spectrum of F^2 . The coefficients for a particular frequency ω_ℓ are determined by summing the terms in Eq. 3.10 with $\omega_j - \omega_k = \omega_\ell$ (and therefore $k = j - \ell$), determining that

$$b_\ell = \sum_j a_{j-\ell}^* a_j. \quad (3.12)$$

All of the terms in Eq. 3.11 will time-average to zero except for the $\ell = 0$ term, so that

$$\overline{|F(t)|^2} = b_0 = \sum_j |a_j|^2. \quad (3.13)$$

Switching from discrete to continuous notation one may express Eq. 3.13 as

$$\langle |F(t)|^2 \rangle = \int_{-\infty}^{\infty} d\omega S_F(\omega). \quad (3.14)$$

Thus in the presence of electric field noise, the average quadratic Stark shift given by $\langle \Delta\omega_{if} \rangle = 1/2(\partial^2\omega_{if}/\partial F^2)\langle |F(t)|^2 \rangle$ is non-zero, and it is possible in principle get some information about $S_F(\omega)$ by measuring the shift spectroscopically.

If $\ell \neq 0$, the right side of Eq. 3.12 is the sum of many phasors pointing in random directions and can be rewritten as

$$b_\ell = \sum_j a_{j-\ell}^* a_j = \sum_j |a_{j-\ell}| |a_j| e^{i(\phi_j)} \quad (3.15)$$

since the difference between two random phases is itself a random phase. Thus the expectation value $\langle b_\ell \rangle = 0$. To determine the power spectral density of F^2 , however, one needs to find

$$\langle |b_\ell|^2 \rangle = \left\langle \left(\sum_k |a_{\ell-k}| |a_k| e^{-i(\phi_k)} \right) \left(\sum_j |a_{\ell-j}| |a_j| e^{i(\phi_j)} \right) \right\rangle, \quad (3.16)$$

which can be separated into two parts:

$$\langle |b_\ell|^2 \rangle = \left\langle \sum_j |a_{j-\ell}|^2 |a_j|^2 \right\rangle + \left\langle \sum_{j \neq k} |a_{j-\ell}| |a_j| |a_{k-\ell}| |a_k| e^{i(\phi_j - \phi_k)} \right\rangle. \quad (3.17)$$

The second term is again a sum of many random phasors and will average to zero. Approaching the continuous limit, one may write

$$\lim_{\delta\omega \rightarrow 0} \frac{\langle |b_\ell|^2 \rangle}{\delta\omega} = \lim_{\delta\omega \rightarrow 0} \sum_j \left(\frac{|a_{j-\ell}|^2}{\delta\omega} \frac{|a_j|^2}{\delta\omega} \right) \delta\omega, \quad (3.18)$$

which, in continuous notation, is

$$S_{F^2}(\omega) = \int_{-\infty}^{\infty} d\omega' S_F(\omega' - \omega) S_F(\omega'). \quad (3.19)$$

If the field noise is $1/f$, with $S_F(\omega) = S_0/|\omega|^\kappa$ ($\kappa \geq 0$), the integrals in Eqs. 3.14 and 3.19 diverge due to the singularity at $\omega = 0$. Convergence requires introduction of a low-frequency cutoff such that $S_F(\omega) \rightarrow 0$ (or is at least finite) below some frequency ω_{ir} . The relevant frequency is dictated by the lower limit of the measurement bandwidth, given approximately by the total time required for all trials averaged in a given measurement, i.e., $\omega_{ir} \approx 1/\tau_{meas}$ [52, 39]. For frequency scalings of interest in this work, the calculated decoherence times are not particularly sensitive to the precise nature of the cutoff or the frequency—for example, pure $1/f$ noise $S_F(\omega) = S_0/|\omega|$ leads to $S_{F^2} = (4/\pi)S_0^2/|\omega| \ln |\omega/\omega_{ir}|$ [62], which scales logarithmically in ω_{ir} .

For $\kappa \leq 1$, an additional high-frequency cutoff, with $S_F(\omega) \rightarrow 0$ above ω_c is required for convergence. Depending on the noise source in question, ω_c may be determined by the upper limit measurement bandwidth, i.e., $\omega_c \approx 1/\tau_{single}$, the time for a single trial [39], or ω_c may lie somewhere within the measurement bandwidth and be extracted from experimental data via fitting [52]. For the values of κ considered in this work ($\kappa = 1/2, 1, 3/2$), the decoherence rate depends explicitly on ω_c only when $\kappa = 1/2$; when $\kappa \geq 1$ the noise falls off quickly enough with increasing frequency that the decoherence rate is independent of ω_c .

In this work, $S_F(\omega)$ of $1/f$ noise is taken to be zero outside of the cutoffs, i.e.,

$$S_F(\omega) = \begin{cases} \frac{S_0}{|\omega|^\kappa}, & \omega_{ir} \leq |\omega| \leq \omega_c \\ 0, & \text{otherwise} \end{cases}. \quad (3.20)$$

For pure $1/f$ noise, if the statistics of F^2 are assumed to be Gaussian, the coherence decay during a Ramsey experiment is given by [62]

$$f_z(t) = e^{-[\Gamma_f \ln(\omega_{ir}t/\pi)]^2}. \quad (3.21)$$

Taking into account the higher order statistics for non-Gaussian F^2 (while assuming that F is Gaussian), the dephasing of Ramsey and Hahn spin echo experiments has been solved analytically in certain time regimes for pure $1/f$ noise, where $S_F(\omega) = S_0/|\omega|$ [62, 52]. It is useful to define

$$\Gamma_f = \left(\frac{1}{2} \frac{\partial \omega_{if}^2}{\partial F^2} \right) S_0. \quad (3.22)$$

In the limit of $\Gamma_f t \ll 1$ [62, 52],

$$f_z(t) = \left[1 + \left(\frac{2}{\pi} \Gamma_f t \ln \frac{1}{\omega_{ir} t} \right)^2 \right]^{-1/4}. \quad (3.23)$$

This is consistent with the Gaussian approximation of Eq. 3.21 for $t \rightarrow 0$. When $\Gamma_f t \gg 1$ [62, 52],

$$f_z(t) = e^{-\Gamma_f t/2}. \quad (3.24)$$

At long times, the exponential time dependence and lack of dependence on ω_{ir} are surprising. Makhlin *et al.* [62] offer a qualitative explanation: the interaction between various low-frequency components due to the non-linear coupling of field noise to the phase effectively cuts off the $1/f$ behaviour of the noise spectrum at frequencies below Γ_f . Below this frequency, the spectral density of the phase fluctuations are consistent with white noise rather than $1/f$ noise, which leads to exponential decay of the coherence at times $t \gg 1/\Gamma_f$ [62].

3.4 Coherent manipulation with microwaves

In the above sections, the details of how to apply rotations around various axes of the Bloch sphere were not discussed. When the Bloch sphere is used to represent a coherent superposition of two Rydberg states, near-resonant microwaves are used to drive population between the states and generate rotations of the Bloch vector. Typical microwave frequencies for the range of n used in this thesis are 30 – 100 GHz. Experimental imperfections such as microwave inhomogeneities and detunings associated with dc Stark shift

from inhomogeneous uncompensated dc electric fields cause loss of fidelity in the rotations; understanding the details of the process is important for estimating the effects of such imperfections.

The applied microwave fields are of the form $\vec{F}(t) = \vec{F}_0 \sin(\omega t + \phi)$, and the electric dipole term in the interaction Hamiltonian is [17]

$$W(t) = -\vec{\mu} \cdot \vec{F}(t) = \vec{\mu} \cdot \vec{F}_0 \sin(\omega t + \phi), \quad (3.25)$$

where $\vec{\mu}$ is the atomic electric dipole moment operator. Taking \vec{F} to lie along the z -axis, the single-photon Rabi frequency is defined as $\Omega_{if} = ez_{if}F_0/\hbar$, where $-ez_{if}$ is the electric dipole matrix element between $|i\rangle$ and $|f\rangle$.

When all the population is initially in state $|i\rangle$, the amplitudes of the state populations oscillate sinusoidally at the Rabi frequency, with the population of $|f\rangle$ given by:

$$|c_f|^2 = \frac{\Omega_{if}^2}{\Omega^2} \sin^2(\Omega t/2), \quad (3.26)$$

where $\Omega^2 = \Omega_{if}^2 + \Delta^2$, with the single-photon detuning $\Delta = (E_f - E_i)/\hbar$.

Representing the superposition of $|i\rangle$ and $|f\rangle$ as a vector on the Bloch sphere, the oscillating field causes the Bloch vector to precess at a rate Ω_{if} around an axis determined by Δ and the phase of the oscillating field. The angle η between the axis of rotation and the z -axis is defined by $\Delta = \Omega \cos \eta$. The azimuthal angle with respect to the z -axis of the Bloch sphere is simply ϕ . This is analogous to control of the spin direction with applied oscillating magnetic fields in NMR; good discussions of the techniques are found in Refs. [50] and [52]. By controlling the frequency and phase of the microwaves, it is possible to implement all of the rotations necessary for the noise spectroscopy described in Sec. 3.3.

When $|i\rangle$ and $|f\rangle$ are connected by a two-photon transition, it is possible for both states to have the same angular momentum quantum number ℓ , so that the difference in electric field polarizability can be made small compared to the one-photon case. This reduces sensitivity for a given n . However, compared to single-photon transitions of the same sensitivity (which will occur at lower n than the two-photon), transition energies between states will be smaller, which may be experimentally more convenient.

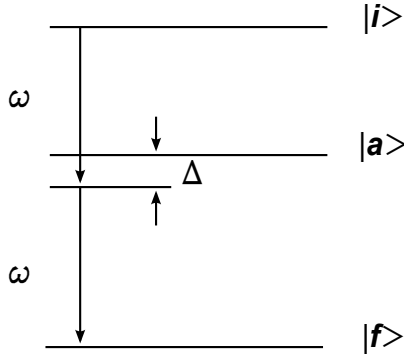


Figure 3.5: Energy level schematic for a resonant two-photon transition between two Rydberg states $|i\rangle$ and $|f\rangle$, driven by near-resonant with an intermediate state $|a\rangle$.

In the two-photon case, I assume that the system has three relevant levels, with an intermediate state $|a\rangle$ as shown in Fig. 3.5. Taking ω exactly (two-photon) resonant with the energy difference between $|i\rangle$ and $|f\rangle$ requires $2\omega = \omega_{if}$. I also define the single-photon detuning $\Delta = \omega - \omega_{ia}$. One should note that in the two-photon case, for oscillating fields of the form $\sin(\omega t + \phi)$, the axis of rotation has an azimuthal angle of 2ϕ with respect to the x -axis of the Bloch sphere.

There are now two single-photon Rabi frequencies, Ω_{ia} and Ω_{af} , for the $|i\rangle \rightarrow |a\rangle$ and $|a\rangle \rightarrow |f\rangle$ transitions, respectively. In the limit of $\Omega_{ia}, \Omega_{af} \ll \Delta$, an exactly resonant oscillating field will cause the populations of $|i\rangle$ and $|f\rangle$ oscillate sinusoidally at the two-photon Rabi frequency, given by [17]

$$\Omega_{R2} = \frac{\Omega_{ia}\Omega_{af}}{2\Delta}, \quad (3.27)$$

while the population of $|a\rangle$ is negligible so long as it is initially unpopulated.

This requirement that $\Omega_{ia}, \Omega_{af} \ll \Delta$ limits the speed at which population can be driven between the two states of interest. As the driving field is increased, Ω_{ia} and Ω_{af} are no longer negligible compared to Δ , and a significant fraction of the population may be driven to state $|a\rangle$. Assuming only state $|i\rangle$ is initially populated, the population of $|a\rangle$ will oscillate

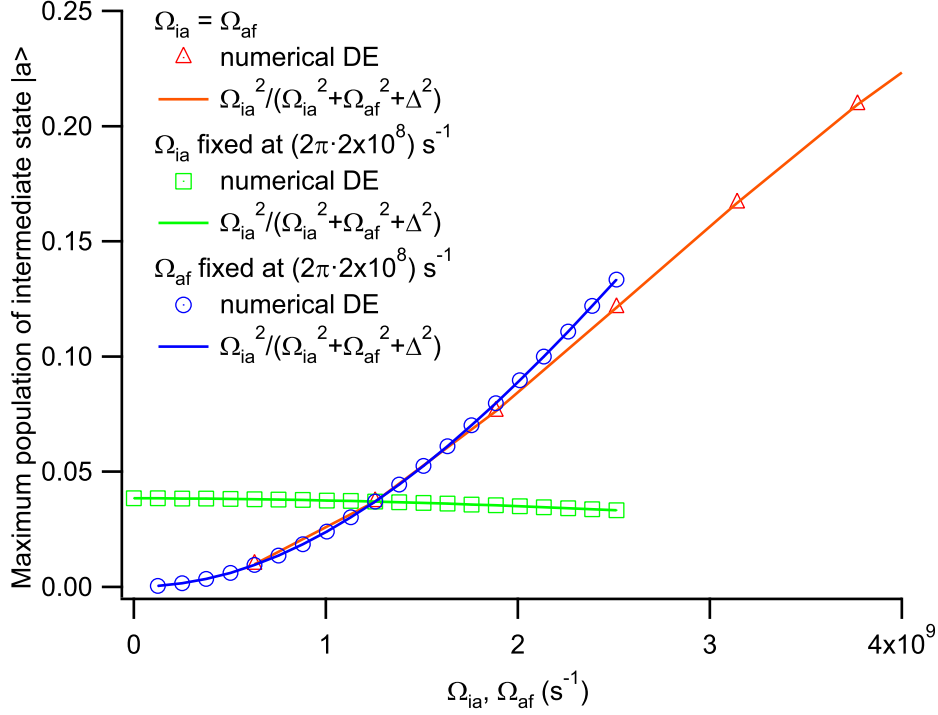


Figure 3.6: Maximum population of the intermediate state $|a\rangle$ during two-photon Rabi flopping (with all population initially in state $|i\rangle$), as a function of the single-photon Rabi frequencies Ω_{ia} and Ω_{af} . The single-photon detuning Δ is $2\pi \times 1$ GHz.

rapidly, evolving in time as

$$|c_a|^2 = \frac{\Omega_{ia}^2}{\Omega_a^2} \sin^2(\Omega_a), \quad (3.28)$$

where $\Omega_a^2 = \Omega_{ia}^2 + \Omega_{af}^2 + \Delta^2$, a result not easily found in literature but which can be verified by numerically integrating the time-dependent Schrödinger equations presented in Ref. [17]. Confirmation that Eq. 3.28 correctly predicts the population of $|a\rangle$ is shown in Fig. 3.6, where results of the numerical integration are consistent with the predictions of Eq. 3.28 for various values of Ω_{ia} and Ω_{af} .

If the microwave field is not homogeneous across the entire volume of the sample, then each atom will have a different Rabi frequency, causing errors in the pulses that lead to dephasing. Inhomogeneity of the oscillating field is also a problem in nuclear magnetic resonance experiments, and a variety of composite pulse sequences which compensate for inhomogeneities in the oscillating field amplitude have been developed (see, for example, the discussion of composite pulses in Refs. [50] and [64], as well as references therein).

However, composite pulse sequences have some disadvantages. Rotations may be performed around several different axes in quick succession, requiring fast modulation of the phase of the oscillating field. As well, the composite sequence will take more time than performing a rotation with a single pulse, which may limit the total amount of free evolution time available and hamper sensitivity of the noise detection. As an example, the commonly used BB₁ sequence [65] is made up of four pulses, rotating around three different axes. A net rotation by angle θ using the BB₁ sequence involves a total rotation of $4\pi + \theta$; therefore a π pulse takes five times as long using this composite sequence than it would for a single pulse of the same field amplitude.

3.5 Noise spectroscopy with driven evolution of Rydberg states

For periodic refocusing pulses at some time interval T , the filter function $g_N(\omega, \tau)$ in Eq. 3.5 will peak at $\omega = \pi/T$, as seen in Fig. 3.3. Therefore, refocusing pulses in high-frequency noise measurements must be closely spaced and short (the length of the refocusing pulses must be $\tau_\pi \ll T$ to allow for free evolution between pulses). Experimentally, such sequences may require undesirably high modulation bandwidths or microwave power. In such situations, driven evolution of the system, in either a spin locking sequence [66] or continuously driven Rabi oscillation, may be a more desirable approach for measuring field noise.

The term “spin locking” comes from NMR experiments [66] in which a magnetic field oscillating at the Larmor frequency is applied. If the nuclear spins are initially aligned

along the direction of the oscillating field (as seen in a frame of reference rotating at the Larmor frequency), the spins will tend to remain aligned with the field without dephasing.

The experimental procedure for a spin-locking experiment may be thought of as quite similar to a Ramsey experiment, in that two $\pi/2$ rotations to create (and then measure) a coherent superposition are separated by an interval in which the coherent superposition evolves. However, in the case of a spin-locking experiment, the evolution during this interval is *driven* evolution, with a continuous rotation around the axis of the Bloch vector, rather than the *free* evolution used in the Ramsey case. As a result, decoherence during a spin-locking sequence is dominated by noise near the Rabi frequency of the driven evolution. This is different from the case of Ramsey or spin-echo sequences, where the decoherence is dominated by noise at frequencies near the maximum of the filter function $g_N(\omega, \tau)$.

In a two-level atomic system described by the Bloch sphere, the spin-locking procedure is as follows: the experiment starts with all the population in state $|i\rangle$, and a $\pi/2$ rotation around the x -axis puts the Bloch vector in the equatorial plane. A continuous rotation around the axis containing the Bloch vector is then applied (this requires the phase of the driving electromagnetic field to be shifted relative to the initial pulse, by 90° if the transition is single-photon or by 45° for a two-photon transition). Finally, a second $\pi/2$ rotation around the same axis as the first is applied to rotate the Bloch vector back along the direction of the z -axis

Describing the system in the rotating frame, the eigenstates $|\tilde{0}\rangle$ and $|\tilde{1}\rangle$ have an energy splitting $\hbar\Omega$. At the start of the continuous rotation, the population is completely in one of these eigenstates, but relaxes exponentially towards equal populations of $|\tilde{0}\rangle$ and $|\tilde{1}\rangle$ (assuming $\hbar\Omega \ll k_B T$). This relaxation is partly due to T_1 relaxation of the energy eigenstate $|i\rangle$ and $|f\rangle$ populations in the non-rotating frame. There is an additional component due to energy fluctuations at the Rabi frequency, so the total relaxation rate (Eq. 42 in Ref. [52]) is:

$$\tilde{\Gamma}_1 = \Gamma_\nu \sin^2 \eta + \frac{1 + \cos^2 \eta}{2} \Gamma_1, \quad (3.29)$$

where $\Gamma_\nu = \pi S_{\delta\omega_{if}}(\Omega)$ is related to the power spectral density of the fluctuations of the energy level separation ω_{if} energy fluctuations at the Rabi frequency Ω (decoherence will be expressed in terms of energy level fluctuations since the coupling of energy levels to

fields may be either linear or quadratic in this analysis). Sensitivity to field noise is maximized when the axis of rotation lies along the equator of the Bloch sphere, i.e., $\eta = \pi/2$, which requires the applied microwaves to be resonant. At the end of the experiment, an additional $\pi/2$ rotation around the x -axis is applied and the coherence is determined from the populations of the energy eigenstates $|i\rangle$ and $|f\rangle$ in the same manner as for the pulsed decoupling sequences discussed previously.

The above analysis is only valid for noise with correlation times shorter than the measurement time [53]. If the noise spectrum is sufficiently broadband, however, the coherence will exponentially decay at long times $t > 2/\tilde{\Gamma}_1$, a result interpreted by Cummings [67] as the system losing “memory” of the initial field on this time scale. Therefore, Γ_1 and Γ_ν may be determined from simple exponential fits of the decay at long times.

Spin locking of a solid state qubit has been used to measure the noise in the phase δ across the Josephson junctions of a quntronium circuit at its optimal working point, where the lowest order of the coupling is quadratic in δ [52]. Spin locking of the electron spin of a single nitrogen-vacancy center in diamond has also been recently used to sensitively detect MHz-frequency oscillating magnetic fields, where the lowest order of the coupling was linear [53].

During spin-locking, if the Bloch vector is not aligned with the axis of rotation (perhaps due to errors in the $\pi/2$ rotations or detuning of the spin-lock pulse) then the vector will precess around the axis at the Rabi frequency. The coherence decays with some characteristic time \tilde{T}_2 , with noise causing both population relaxation and pure dephasing in the rotating frame [52]. The same analysis applies to Rabi oscillations (where an angle of $\pi/2$ between the Bloch vector and the rotation axis is usually desired), such that Rabi oscillations also lose coherence with time scale \tilde{T}_2 [52]. Therefore it is desirable to express this dephasing rate in terms of the noise, in order to measure the noise spectrum through experimental measurement of the decays of the Rabi oscillations.

For noise spectra that do not diverge at $\omega = 0$, the dephasing in the rotating frame is exponential, with a total rate [52]

$$\tilde{\Gamma}_2 = \frac{3 - \cos^2 \eta}{4} \Gamma_1 + \Gamma_\phi \cos^2 \eta + \frac{1}{2} \Gamma_\nu \sin^2 \eta, \quad (3.30)$$

where $\Gamma_\phi = \pi S_{\delta\omega_{if}}(\Omega = 0)$. If the noise is $1/f$, diverging at $\omega = 0$, the decay of the coherence is non-exponential. Ithier *et al.* [52] treat the case where only the Γ_ϕ -related part of the decay is non-exponential, which requires Ω to be large enough that the decay related to Γ_ν can be treated exponentially. In this limit, the amplitude of the Rabi oscillations decays as

$$f_{Rabi}(t) = f_{z,cos\eta}(t) \exp\left(-\frac{3 - \cos^2\eta}{4}\Gamma_1 t - \frac{\sin^2\eta}{2}\Gamma_\nu t\right) \quad (3.31)$$

where $f_{z,cos\eta}(t)$ is a modified form of one of the expressions for f_z given previously (the expression used depends on the coupling to the noise and whether the statistics are Gaussian). The expression is modified by replacing $(\partial\omega_{if}/\partial\lambda)$ by $\cos\eta(\partial\omega_{if}/\partial\lambda)$ in the case of linear coupling to the noise and $(\partial^2\omega_{if}/\partial\lambda^2)$ with $\cos\eta(\partial^2\omega_{if}/\partial\lambda^2)$ in the case of quadratic coupling. When the microwaves are resonant, $\cos\eta \rightarrow 0$ implies $f_{z,cos\eta}(t) \rightarrow 1$, simplifying Eq. 3.31.

Decay of Rabi oscillations has been used to measure the $1/f$ flux noise in persistent-current qubits [39] as well as noise in the phase of the Josephson junctions of a quantum circuit at its optimal working point [52], where measurements of the noise using Rabi flopping were consistent with spin-locking results.

In the case of Rydberg atoms, inhomogeneity of the microwave power across the size of the sample creates an additional source of dephasing, which may even dominate the other sources of decoherence. In this situation, the effectiveness of Rabi-flopping noise measurements will be limited, and spin-locking sequences, which are unaffected by dephasing if the microwaves are on-resonance, will be a better method.

3.6 Numerical simulations

3.6.1 Monte Carlo calculations of decoherence $f_z(t)$

Analytical solutions for the decoherence $f_z(t)$ of Ramsey and spin-echo sequences may not be feasible for all couplings, time scales, and noise spectral density scalings of interest.

In particular, analytical solutions in the case of quadratic coupling to noise with power spectral density of the form $1/f^\kappa$ appear to exist in the literature only for $\kappa = 1$.

Monte Carlo simulations averaging over many realizations of random field time sequences provide another method of calculating $f_z(t)$ in cases of interest. For Ramsey or spin-echo sequences with quadratic Stark shifts, the coherence is [52]

$$f_z(t) = \left\langle \exp \left[i \frac{1}{2} \frac{\partial \omega_{if}^2}{\partial F^2} \int_0^t d\tau G(\tau) F^2(\tau) \right] \right\rangle, \quad (3.32)$$

with the gating function $G(\tau)$ alternating between ± 1 at each refocusing π -pulse.

The random field noise may be modelled as the sum of Fourier components, with the amplitudes determined by the spectral density of the noise source as in Eq. 3.9 and random phases. With N independent Fourier components, spaced by $\Delta\omega$, the cutoff frequencies are $\omega_{ir} = \Delta\omega$ and $\omega_c = N\Delta\omega$. The summation is effectively an inverse discrete Fourier transform and gives a discrete time series of $2N$ discrete time points over a record length $T = 2\pi/\Delta\omega$. This may be done efficiently with any fast Fourier transform algorithm. Summing over n realizations, the fractional uncertainty of $\langle \exp[i\delta\phi] \rangle$ is of the order $1/\sqrt{n}$.

Results of the simulation for pure $1/f$ noise of the form $S_F(\omega) = S_0/\omega$ are presented for various S_0 in Fig. 3.7. For noise of this form, analytical solutions exist in the literature [62, 52]. However, reproducing the analytical result with the Monte Carlo simulations is useful for validating the model. At long times $t > 1/\Gamma_f$, these simulations show the Hahn spin-echo and Ramsey sequences tending toward identical coherences. This is consistent with the picture of high-frequency noise (which cannot be effectively mitigated by refocusing) being the dominant source of decoherence in this regime, as expected from the exponential form of the decay at long times calculated analytically (and quoted in this work as Eq. 3.24).

A natural time scale is provided by $\Gamma_f = 1/2(\partial\omega_{if}^2/\partial F^2)S_0$, and coherence is plotted as a function of scaled time $\Gamma_f t$ in Fig. 3.8. In this scaled-time representation, it is easy to see that the coherence decays at long times $\Gamma_f t > 1$ as

$$f_z(t) \propto e^{-\Gamma_f t/2}, \quad (3.33)$$

consistent with Eq. 3.24. This behaviour is independent of Γ_f , ω_{ir} , and ω_c up to a prefactor (constant at long times) dictated by the decoherence at short times—this prefactor depends

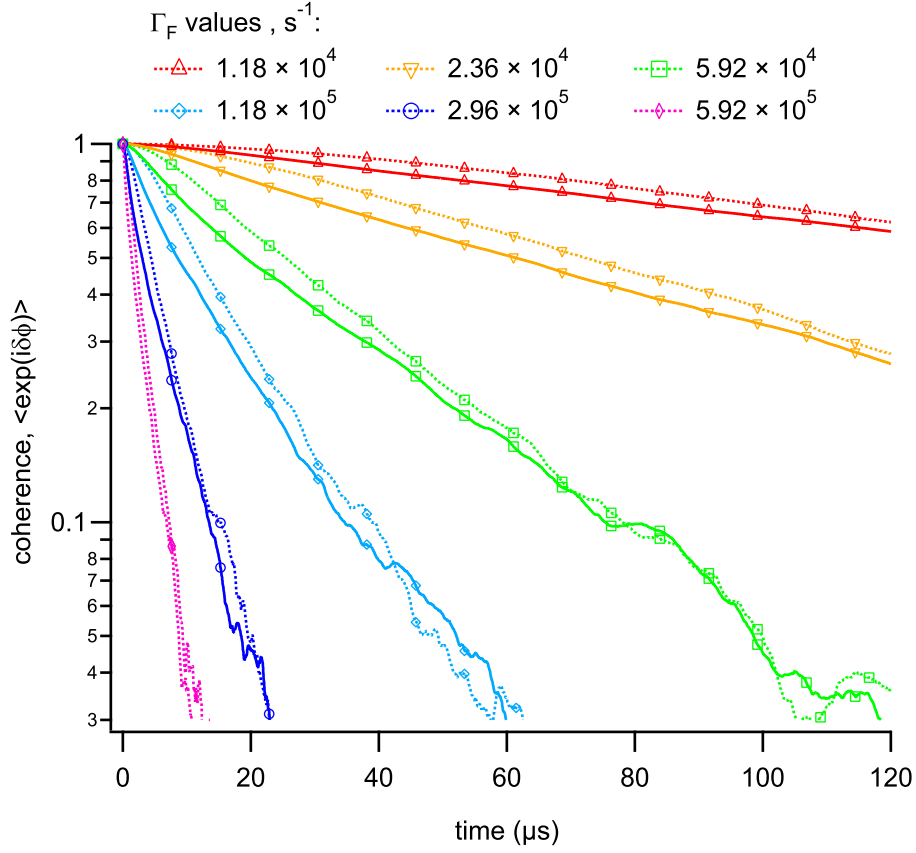


Figure 3.7: Monte Carlo simulation of coherence decay for Ramsey sequences (solid lines) and Hahn spin-echo sequences (dashed lines) with pure $1/f$ electric field noise and a quadratic Stark shift. Lower cutoff frequency $\omega_{ir} = 2\pi \times 1$ kHz, statistical uncertainty of the calculated coherences is $1/\sqrt{n} = 10000 = 0.01$.

on the relative magnitudes of ω_{ir} and Γ_f . The $1/f$ noise falls off sufficiently fast with increasing frequency that the results are independent of ω_c (provided that $\omega_c > 1/t$ for all times of interest).

This exponential behaviour at long times is not confined to pure $1/f$ noise. Simulations where the noise spectrum $S_F(\omega) = S_0/\omega^\kappa$, with $\kappa = 1/2, 3/2$, show similar exponential time dependence of the coherence at sufficiently long times. For a given value of κ , the time

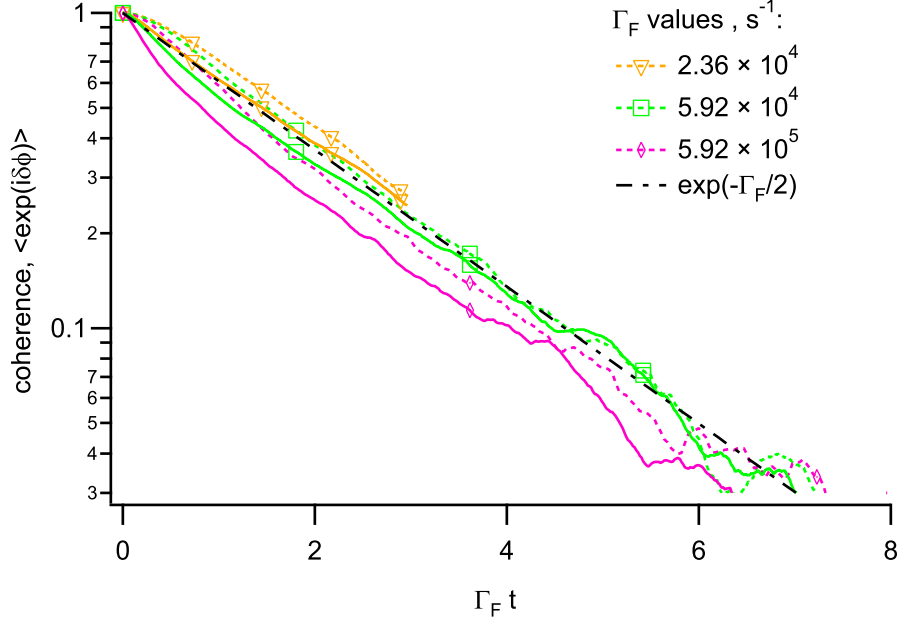


Figure 3.8: Coherence decay for Ramsey sequences (solid lines) and Hahn spin-echo sequences (dashed lines) as a function of the scaled time $\Gamma_f t$ in the presence of $1/f$ electric field noise and quadratic Stark shift. Lower cutoff frequency $\omega_{ir} = 2\pi \times 1$ kHz, statistical uncertainty of the calculated coherences is $1/\sqrt{n} = 10000 = 0.01$.

constant of the decay, τ , has a power-law dependence on S_0 , approximately $(1/\tau) \propto S_0^{1/\kappa}$ as shown in Fig. 3.9 (with ω_{ir} and ω_c kept fixed).

This result suggests the possibility of a simple relationship between the noise amplitude and the decay rate of the coherence at long times. I extend the definition of Γ_f beyond the $\kappa = 1$ case:

$$\Gamma_f = \left(\frac{1}{2} \frac{\partial^2 \omega_{if}}{\partial F^2} S_0 \right)^{1/\kappa}, \quad (3.34)$$

which is consistent with the previous definition of Eq. 3.22 when $\kappa = 1$.

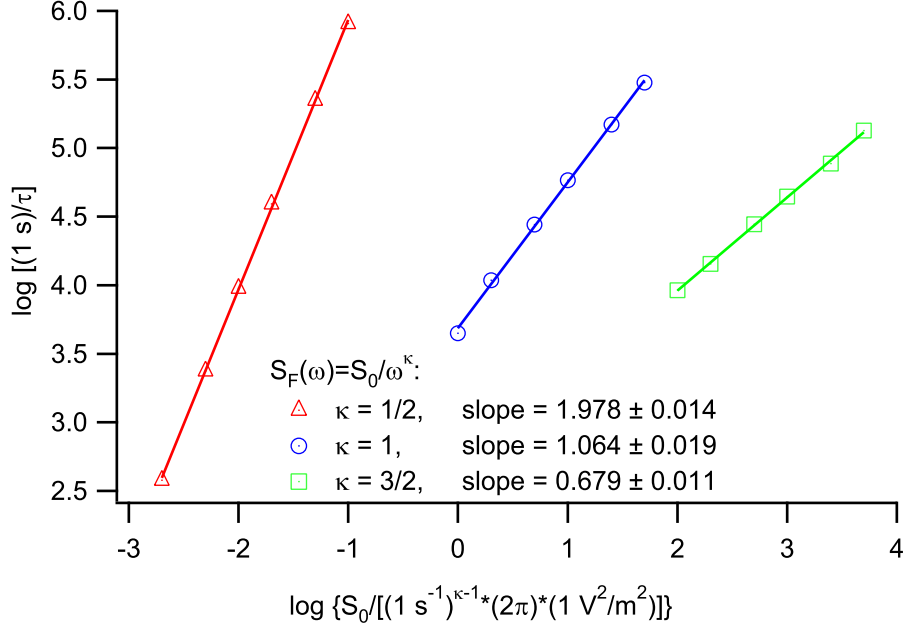


Figure 3.9: Dependence of τ , the time constant of coherence decay at long times, on S_0 , for noise spectral density of the form $S_F(\omega) = S_0/\omega^\kappa$. For all calculations in this plot, $\omega_{ir} = 2\pi \times 1 \text{ kHz}$, $\omega_c = 2\pi \times 4.19 \text{ GHz}$, and $(\partial^2 \omega_{if}/\partial F^2) = 2\pi \times 600 \text{ Hz}/(\text{V}/\text{m})^2$.

For $\kappa = 3/2$, coherence vs. $\Gamma_f t$ for various values of Γ_f is plotted in Fig. 3.10. At long times, the decay is of the form

$$f_z(t) = e^{-(3/2)\Gamma_f t/2}, \quad (3.35)$$

again up to a prefactor which is constant at long times. The dynamic range in S_0 is similar to Fig. 3.8; presumably the larger variation in the prefactor for $1/f^{3/2}$ noise is due to the larger amount of low-frequency noise present when κ is larger.

The situation at long times is more complicated when $\kappa = 1/2$, because the noise falls off more slowly with increasing frequency. Therefore, $f_z(t)$ depends on ω_c . Coherence vs. $\Gamma_f t$ for various values of Γ_f is plotted in Fig. 3.11. The dependence of the decay on Γ_f is rather weak, changing from $\exp[-1.41\Gamma_f t]$ to $\exp[-2.01\Gamma_f t]$ as Γ_f is changed over two orders of magnitude.

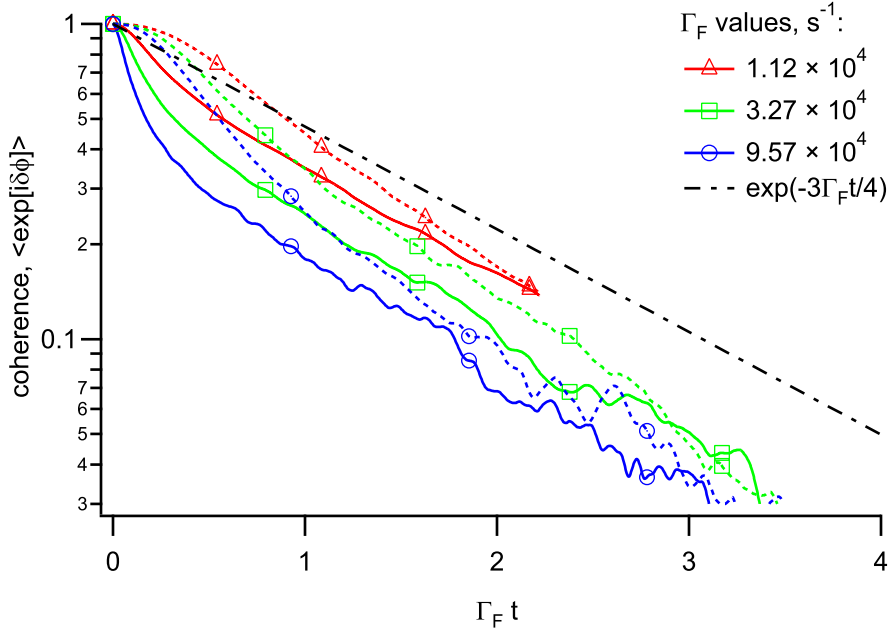


Figure 3.10: Coherence decay for Ramsey sequences (solid lines) and Hahn spin-echo sequences (dashed lines) as a function of the scaled time $\Gamma_f t$, with $1/f^{3/2}$ electric field noise and a quadratic Stark shift. Lower cutoff frequency $\omega_{ir} = 2\pi \times 1$ kHz, statistical uncertainty of the calculated coherences is $1/\sqrt{n} = 10000 = 0.01$.

At long times, the decay is consistent with the form

$$f_z(t) = e^{-c\Gamma_f \ln(\omega_u/\Gamma_f)t}, \quad (3.36)$$

where ω_u is a high frequency cutoff that may be different from ω_c . The scaled decay rate $1/\Gamma_f \tau$ as a function of Γ_f/ω_c is shown in Fig. 3.12, along with fits used to determine c and ω_u . Fixing $\omega_u = \omega_c$ for the calculations shown gives a fitted value of $c = 0.055 \pm 0.001$, while allowing ω_u to vary gives a better fit to the data shown, with $c = 0.042 \pm 0.002$ and $\omega_u/\omega_c = 25 \pm 15$. The uncertainty in ω_c and the large discrepancy between ω_u and ω_c show that the decay rate of the coherence is not particularly sensitive to the details of the high-frequency cutoff, particularly when $\Gamma_f \ll \omega_c$.

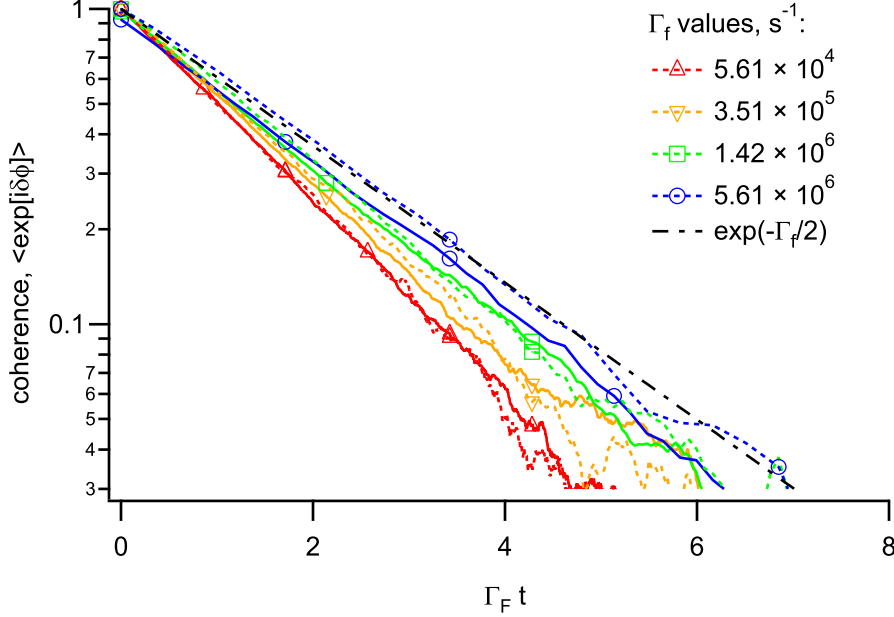


Figure 3.11: Coherence decay for Ramsey sequences (solid lines) and Hahn spin-echo sequences (dashed lines) as a function of the scaled time $\Gamma_f t$, with $1/f^{1/2}$ electric field noise and a quadratic Stark shift. Lower cutoff frequency $\omega_{ir} = 2\pi \times 1$ kHz, upper cutoff frequency $\omega_c = 2\pi \times 4.19$ GHz, and statistical uncertainty of the calculated coherences is $1/\sqrt{n} = 10000 = 0.01$.

The exponential behaviour of the coherence decay for Ramsey and spin-echo sequences over a range of κ , with decay rates on the order Γ_f , suggests that the decoherence rate may be described by a relatively straightforward scaling law. This is, in a way, an inconvenient result because the form of the coherence decay gives no information about the value of κ . However, if κ can be determined through measurements with higher spectral selectivity (multi-pulse sequences, for example) then the decay rate at long times can easily be used to measure the noise amplitude.

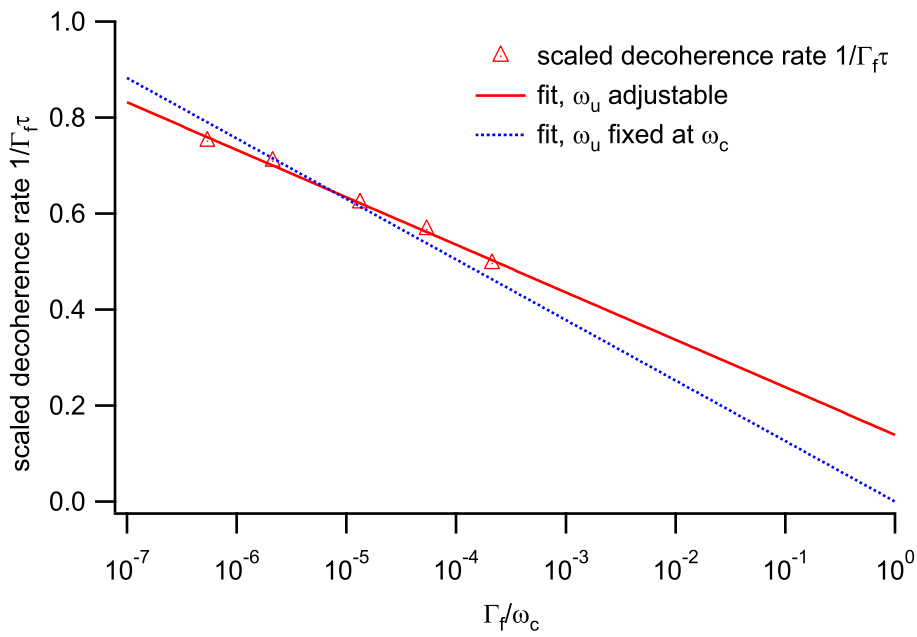


Figure 3.12: Dependence of scaled decoherence rate $1/\Gamma_f\tau$ on the scaled upper cutoff frequency ω_c/Γ_f for $1/f^{1/2}$ noise.

3.6.2 Time-evolution of the density matrix

The simulations in the previous section calculate the dephasing $f_z(t)$ due to noise but neglect the effects of experimental imperfections such as pulse errors due to microwave inhomogeneity and population transfer during microwave pulses to nearby Rydberg states which cannot be resolved by selective field ionization. It is useful to create Monte Carlo simulations incorporating these effects, as well as the field noise, in order to determine whether these experimental imperfections affect the measured coherence decay times for a measurement sequence of interest.

I use the Pauli master-equation model described in Bidégaray *et al.* [68]. The Hamiltonian is given by $H = H_0 + V(t)$, where H_0 is the unperturbed Hamiltonian (diagonal in the chosen basis) and $V(t)$ is a perturbation, in our case due to atom-electric field interactions. The state of the atomic system is described by the density matrix ρ , with populations given by the diagonal elements ρ_{jj} and coherences by the off-diagonal elements ρ_{jk} . The master equation is given by Eq. (3) in Ref. [68]:

$$\dot{\rho} = \frac{i}{\hbar} [H, \rho] + Q(\rho), \quad (3.37)$$

with the decoherence matrix Q to be defined below in Eqs. 3.39 and 3.40. I use the interaction picture, transforming operators from their Schrödinger equivalents by $O_{int} = \exp(iH_0)O_{sch}$. Thus Eq. 3.37 becomes

$$\dot{\rho} = \frac{i}{\hbar} [V, \rho] + Q(\rho). \quad (3.38)$$

The decoherence matrix Q can be used to include the effects of relaxation due to spontaneous emission, blackbody radiation-induced population redistribution, and collisions. In this model, the diagonal elements of Q ,

$$Q(\rho)_{jj} = \sum_{\ell \neq j} W_{j\ell} \rho_{\ell\ell} - \sum_{\ell \neq j} W_{\ell j} \rho_{jj} = \sum_{\ell \neq j} W_{j\ell} \rho_{\ell\ell} - \Gamma_j \rho_{jj}, \quad (3.39)$$

are determined by population transfer between states (cf. Eq. (4) in Ref. [68]). Here, $W_{\ell j}$ is the rate of population transfer from state $|j\rangle$ to state $|\ell\rangle$, and the total loss rate from state $|j\rangle$ is given by Γ_j . Off-diagonal elements of Q are associated with loss of coherence and

have contributions from population redistribution as well as any other possible decoherence mechanisms such as elastic collisions. I use the common model

$$Q(\rho)_{jk} = -\gamma_{jk}\rho_{jk} = -\left[\frac{1}{2}(\Gamma_j + \Gamma_k) + \gamma_{jk}^{coll}\right], \quad (3.40)$$

where $\gamma_{jk}^{coll} \geq 0$ represents the contribution of elastic collisions (and any other decoherence mechanism not associated with population transfer).

In our simulations, the perturbation $V(t)$ has two main components: oscillating electric fields near resonance with atomic transitions (frequencies typically 30 – 100 GHz) which are applied to manipulate the atoms, and non-resonant slowly varying electric fields (up to a few GHz) which slightly perturb the energy eigenstates via the Stark shift.

Resonant oscillating electric fields are taken as $\vec{F}(t) = \vec{F}_0(t) \exp(i\omega t) + \vec{F}_0^*(t) \exp(-i\omega t)$, with phase information contained in the slowly varying complex amplitude $\vec{F}_0(t)$. In the interaction picture, elements of the perturbation are

$$V_{jk}(t) = -\vec{\mu} \cdot \vec{F}(t) = e\vec{r} \cdot \vec{F}_0(t) e^{i(\omega_{jk} + \omega)t} + e\vec{F}_0^*(t) e^{i(\omega_{jk} - \omega)t}, \quad (3.41)$$

where $\vec{\mu} = -e\vec{r}$ is the atomic dipole moment operator and $\hbar\omega_{jk} = E_j - E_k$ is the energy level separation. The polarization of the resonant field is assumed to be constant, so that it is possible to take $F_0(t) = \hat{e}_F F_0(t)$. The radial integrals in the dipole matrix elements $\mu_{jk} = \langle j | \hat{e}_F \cdot \vec{r} | k \rangle$ are calculated numerically using the Numerov method [69]. Since $\omega \approx \omega_{jk}$, only the slowly varying terms in Eq. 3.41 are kept and the perturbation is written in matrix form as

$$V_r(t) = \begin{pmatrix} 0 & \mu_{12}F_0^*(t) & \mu_{13}F_0^*(t) & \cdots \\ \mu_{21}F_0(t) & 0 & \mu_{23}F_0^*(t) & \cdots \\ \mu_{31}F_0(t) & \mu_{32}F_0(t) & 0 & \cdots \\ \vdots & \vdots & \vdots & \ddots \end{pmatrix}, \quad (3.42)$$

(assuming $E_1 > E_2 > E_3$).

The resonant fields determine the choice of basis for numerically integrating Eq. 3.38. The basis must include the initially populated state and any states that can be significantly populated via resonant one- or two-photon transitions. It is also necessary to include any intermediate states involved in the two-photon transitions.

Non-resonant electric fields shift the energy levels of the atom via the Stark effect. If a field \vec{F} varies sufficiently slowly, the shift is given by the dc Stark effect:

$$\Delta E_j = \sum_{k \neq j} \frac{\langle j | \vec{F}(t) \cdot \vec{\mu} | k \rangle \langle k | \vec{F}(t) \cdot \vec{\mu} | j \rangle}{E_j - E_k}. \quad (3.43)$$

As before, the direction of \vec{F} is taken to be constant when the relevant matrix elements μ_{jk} are calculated. I assume that F is small enough that any mixing of the zero-field eigenstates due to F —which will be of order $F(t)\mu_{jk}/(E_j - E_k)$ —is negligible. For states with quadratic Stark shifts, calculating the polarizabilities

$$\alpha_j = -2 \frac{\Delta E_j}{F^2} = \sum_{k \neq j} \frac{\langle j | \hat{e}_F \cdot \vec{\mu} | k \rangle \langle k | \hat{e}_F \cdot \vec{\mu} | j \rangle}{E_j - E_k} \quad (3.44)$$

gives the energy shifts, which can be written in matrix form as

$$V_{nr}(t) = -\frac{1}{2} F(t)^2 \begin{pmatrix} \alpha_1 & 0 & \cdots \\ 0 & \alpha_2 & \cdots \\ \vdots & \vdots & \ddots \end{pmatrix}. \quad (3.45)$$

Accurate calculation of the polarizabilities α_j must include the contributions of a range of states extending over several values of the principal quantum number n in each direction. Therefore, the basis necessary for calculating the elements of V_{nr} is a good deal larger than the basis used for numerically integrating Eq. 3.38. However, the polarizabilities need only be calculated once. The fluctuating field is modelled as a time sequence of field magnitudes generated by summing a large number of Fourier components with random phases as described in Sec. 3.6.1.

Eq. 3.38 is numerically integrated using the implicit Adams differentiation method of the VODE integrator [70]. This is an adaptive routine which adjusts the step size as necessary for accuracy, requiring calculation of $F(t)$ at arbitrary times, which is done by interpolating the discrete values of $F(t)$ calculated using fast Fourier transforms. The code is implemented in Python; calculation of ρ , and particularly the interpolation of $F(t)$, is responsible for most of the computational time.

The simulations described in this section were used in to calculate the population transfer to the intermediate $48p_{3/2}$ state in experiments coherently driving the two-photon $49s_{1/2} - 48s_{1/2}$ transition; results are shown in Sec. 4.5. This method was also used to confirm the feasibility of adiabatic rotation of the spin-locking axis in order to decrease the susceptibility of the method to inhomogeneous dc electric fields; this adiabatic rotation is discussed in Sec. 3.7.

3.7 Sensitivity limits

The minimum detectable $S_F(\omega)$ depends on the polarizability of the states involved, which for a given state may be maximized with the application of a dc electric field. With a sufficiently strong bias field, the dominant order of the Stark shift (for small deviations from the bias field value) becomes linear.

As illustrated in Fig. 3.3, a pulsed decoupling sequence with total free evolution time τ will have a filter function $g_N(\omega, \tau)$ with center frequency $\omega_N = \pi N/\tau$, bandwidth $\Delta\omega_N \approx 2\pi/\tau$ and an average value over this bandwidth of approximately $1/2\pi$. Therefore, one may approximate the coherence integral of Eq. 3.4 as

$$\ln f_z(t) \approx -\tau^2 \left(\frac{\partial\omega_{if}}{\partial F} \right)^2 S_F(\omega_N) \left(\frac{1}{2\pi} \right) \left(\frac{2\pi}{\tau} \right) \quad (3.46)$$

$$= \tau \left(\frac{\partial\omega_{if}}{\partial F} \right)^2 S_F(\omega_N). \quad (3.47)$$

$$(3.48)$$

Reasonably detectable dephasing has $|\ln f_z(t)| \gtrsim 1$, so the minimum detectable field noise is:

$$S_{Fmin}(\omega_N) = \frac{1}{\tau(\partial\omega_{if}/\partial F)^2}. \quad (3.49)$$

Increasing τ while keeping ω_N constant requires adding more refocusing pulses. Therefore, if the number of pulses is limited due to time or microwave homogeneity constraints, rewriting Eq. 3.49 in terms of ω_N and the maximum number of pulses N_{max} may be more useful:

$$S_{Fmin}(\omega_N) = \frac{\omega_N}{\pi N_{max}(\partial\omega_{if}/\partial F)^2}. \quad (3.50)$$

Ultimately, τ is limited by T_1 , the time constant of population relaxation (both spontaneous emission and blackbody-induced population transfer contribute significantly to the rate).

For a spin-locking sequence, a reasonable detection limit for the decoherence rate due to dephasing is the population relaxation, such that detectable decoherence due to electric field noise requires $\Gamma_\nu \geq 1/T_1$. Therefore,

$$\pi \left(\frac{\partial\omega_{if}}{\partial F} \right)^2 S_F(\Omega_R) \geq \Gamma_1, \quad (3.51)$$

corresponding with a minimum detectable field noise

$$S_{Fmin} = \frac{1}{\pi T_1 (\partial\omega_{if}/\partial F)^2}. \quad (3.52)$$

This differs by a factor of π from the pulsed-refocusing case of Eq. 3.49 when τ is limited by T_1 . Thus spin-locking and pulsed-refocusing noise measurements have similar ultimate sensitivity.

By increasing the principal quantum number n of the Rydberg states used, one may increase both the sensitivity of the states to electric field and the lifetime. If arbitrary bias fields may be applied, the maximum $\partial\omega_{if}/\partial F$ is given by the permanent dipole moment of the extreme Stark manifold states:

$$\frac{\partial\omega_{if}}{\partial F} \approx \frac{ea_0 n^{*2}}{\hbar} \approx 2\pi (12.8 \text{ kHz}/(\text{V}/\text{m})) n^{*2}. \quad (3.53)$$

Therefore the sensitivity to electric field scales as n^{*4} .

The spontaneous emission lifetime can be approximated by the semiempirical formula [71]

$$\tau_0 = \tau_s n^{*\delta}, \quad (3.54)$$

with the values of δ and τ_s determined by detailed calculations. For low angular momentum states of alkali atoms, $\delta \approx 3.00$. Values of τ_s for rubidium are 1.37 ns for s states, 2.5 ns for

p states, and 1.07 ns for d states [72]. Blackbody radiation from the ≈ 300 K environment causes population to be transferred to nearby Rydberg states at a rate [73]

$$1/\tau_{BB} = 4\alpha^3 kT/3n^{*2} \approx 6.79 \times 10^4 (T/n^{*2}) (s^{-1}), \quad (3.55)$$

where T is the temperature of the environment in Kelvin, and α is the fine structure constant.

Several factors limit practically available sensitivity. Stark shifts due to uncompensated inhomogeneous dc electric fields must be small compared to the Rabi frequency of any microwave manipulation. The sensitivity to field inhomogeneity in the limit of large bias fields may be calculated from Eq. 3.53. Energy level spacings scale as $1/n^3$, so at large n maintaining large Rabi frequencies may not be possible without excitation of states nearby in energy. Finally, the matrix elements for optical excitation of Rydberg states drop sharply with increasing n , so at very large n the Rydberg population may be too small for good signal/noise in the detection.

As an example of practically achievable sensitivity for a pulsed decoupling sequence, consider a spin-echo experiment with dc field inhomogeneities of 1 V/m and a Rabi frequency of 100 MHz (feasible for single-photon transitions). DC Stark shifts $\delta\omega$ must be small compared to the Rabi frequency Ω , and keeping the maximum shift $\delta\omega < 0.1\Omega$ limits $\partial\omega_{if}/\partial F \leq 2\pi \times 10^7 \text{ s}^{-1}/(\text{V/m})$. The maximum practical polarizability is thus achievable with large dc biasing for $n^* \approx 30$, but states with higher n will still give improved sensitivity due to longer lifetimes. Using the $50s_{1/2}$ and $50p_{3/2}$ states of rubidium, with lifetimes in a 300 K environment of $65 \mu\text{s}$ and $89 \mu\text{s}$ respectively [72] results in $T_1 = 37 \mu\text{s}$ and $S_{Fmin} \approx 6.8 \times 10^{-12} (\text{V/m})^2\text{s}$. For noise at 1 MHz, this gives the figure of merit $\omega S_F(\omega) = 4.2 \times 10^{-5} (\text{V/m})^2$, which is typically seen about $200 \mu\text{m}$ away from the surface of non-cryogenic ion traps [10, 11].

For spin-locking sequences, the Rabi frequencies of interest will be lower, in the range of $\Omega \approx 2\pi \times 1 - 10$ MHz, while the same requirement that DC Stark shifts must be small applies. The maximum tolerable dc Stark shift is thus in the 0.1 – 1 MHz range, with $S_{Fmin} \approx 6.8 \times 10^{-8} - 6.8 \times 10^{-10} (\text{V/m})^2\text{s}$ for the parameters listed above. Therefore, pulsed decoupling sequences, when practical, offer greater sensitivity when the atomic polarizability is limited by inhomogeneous dc electric fields due to the higher Rabi frequencies.

It is possible to adiabatically change the microwave frequency during spin-locking to gradually move the axis of rotation from the z -axis to the x -axis of the Bloch sphere, replacing the $\pi/2$ pulses of the spin-locking sequence described earlier with an adiabatic frequency sweep. In such a sequence, the microwaves are applied in one long pulse, initially far detuned from resonance so that the axis of rotation of the Bloch vector is near the z -axis. The frequency is then gradually swept onto resonance, and the rotation axis moves correspondingly from the z -axis to the x -axis. The Bloch vector, precessing around the rotation axis, likewise rotates from its initial alignment along the z -axis to the x -axis. After holding the microwaves on-resonance for the desired spin-locking time, the frequency is then swept back to large detuning to implement rotation back to the z -axis.

This sequence keeps the Bloch vector aligned along the rotation axis regardless of any Stark-shift induced detuning due to dc field inhomogeneity and therefore relaxes the requirement of dc field homogeneity to $\delta\omega \approx \Omega$, improving $S_{Fmin} \approx 6.8 \times 10^{-10} - 6.8 \times 10^{-12} \text{ (V/m)}^2\text{s}$ when $\Omega \approx 2\pi \times 1 - 10 \text{ MHz}$ for the parameters listed above.

3.8 Summary

A summary of noise measurements and theoretical microscopic models for the origin of the field noise from the ion-trap literature has been presented. These models predict frequency scaling of the noise power spectral density of the form $1/f^\kappa$, though κ is frequency dependent for one model. Methods for detecting field noise using the dephasing of Rydberg atoms have been discussed. These are adaptations of techniques from the NMR and solid-state qubit literature.

Monte Carlo simulations have been used to calculate the decoherence of a coherent superposition of two low angular-momentum Rydberg states with quadratic Stark shifts in the presence of $1/f$ electric field noise. The noise was assumed to have a power spectral density of the form $S_F(\omega) = S_0/\omega^\kappa$. Three frequency scalings relevant to models of noise near the surface were investigated ($\kappa = 1/2, 1, 3/2$); analytical solutions in the literature are found only for $\kappa = 1$. The coherence decays exponentially at long times in both Ramsey-type and Hahn spin-echo sequences for all three values of κ , with the decay rate

of the order $\Gamma_f = [(1/2) \times (\partial^2 \omega_{if} / \partial F^2) \times S_0]^{1/\kappa}$ in all three cases. The calculated decay time for $\kappa = 1$ is consistent with analytical calculations in the literature. The results of these simulations suggest that a relatively straightforward scaling law for the decoherence rate may apply over a range of κ for systems quadratically coupled to $1/f$ noise sources.

Finally, the ultimate sensitivity of Rydberg atoms for detecting field noise has been estimated. Minimum detectable noise spectral density is on the order of $7 \times 10^{-12} \text{ (V/m)}^2 \text{ s}$ for conveniently accessible Rydberg states and reasonable constraints on the dc electric field homogeneity.

Chapter 4

AC electric field measurements

4.1 Introduction

This chapter contains experimental demonstration of the ac field noise measurement techniques described in chapter 3, using the $49s_{1/2} - 48s_{1/2}$ transition of ^{87}Rb . Rabi oscillations between the two states demonstrate the coherent control required for implementing spin-echo and spin-locking measurements of noise. Microwave spectroscopy and coherence decay of Ramsey and Hahn spin-echo sequences have been used to set upper and lower bounds on the electric field noise amplitude measured several mm away from the surface of the chip.

Two significant experimental imperfections have been characterized: a standing wave pattern in the microwave fields, and undesired excitation of the intermediate $48p_{3/2}$ state by the microwaves used to drive the two-photon $49s_{1/2} - 48s_{1/2}$ transition.

4.2 Apparatus

The apparatus has been previously described in Section 2.3 and most of the details of the experimental sequence are similar. The two-photon optical excitation is to the $49s_{1/2}$ state

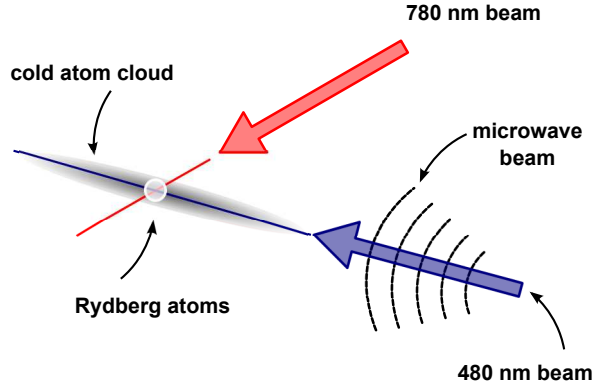


Figure 4.1: Geometry of two-photon optical excitation to Rydberg states. The 780 nm beam (near-resonant with the $5s_{1/2} - 5p_{3/2}$ transition) is focused and steered to control the length and position of the Rydberg sample in the standing wave pattern ($200\ \mu\text{m} - 4\ \text{mm}$ in this work). The 480 nm beam (near-resonant with the $5p_{3/2} - ns_{1/2}$ transition) is focused and steered to control the distance of the Rydberg sample from the chip surface. Microwaves are introduced through a horn along roughly the same axis as the 480 nm beam.

for the results in this chapter, using the same two-laser $5s_{1/2} - 5p_{3/2} - ns_{1/2}$ excitation scheme previously described. The microwaves to drive the $49s_{1/2} - 48s_{1/2}$ transition are introduced using a microwave horn outside the experimental chamber. Fig. 4.1 shows the geometry of the optical and microwave excitation.

For the experiments in this chapter, the cold ground-state atoms were prepared as described in Section 2.3 and the timing diagram in Fig. 2.1. The atoms were excited to the $49s_{1/2}$ state with a $30\ \mu\text{s}$ long optical pulse. The optical pulse was followed by the application of microwave pulse sequences (taking up to $6\ \mu\text{s}$) and detection of the populations of the $48s_{1/2}$ and $49s_{1/2}$ with selective field ionization.

Except where noted, the measurements in this chapter were taken with Rydberg atoms released from the magneto-optical trap several mm away from the surface of the chip, skipping loading of the microtrap. This was done in order to operate the experiment at

higher repetition rates while debugging the microwave sequences and measuring fields far from the chip surface.

4.3 Coherent manipulation, Ramsey and spin-echo results

The coherent manipulation techniques required for noise measurements were demonstrated using the $48s_{1/2}$ and $49s_{1/2}$ states of ^{87}Rb . These states are separated in energy by 70.475717 GHz, calculated using the quantum defects published in Ref. [74]. The Stark shifts are quadratic, $\Delta E = -(\alpha/2)F^2$, with $\alpha/2 \approx 19.2 \text{ MHz}/(\text{V}/\text{cm})^2$ for $48s_{1/2}$ and $\alpha/2 \approx 22.2 \text{ MHz}/(\text{V}/\text{cm})^2$ for $49s_{1/2}$. Thus the polarizability difference is $(\partial^2\omega_{if}/\partial F^2) = (2\pi) \times 600 \text{ Hz}/(\text{V}/\text{m})^2$. Spontaneous emission and population redistribution due to black-body radiation limit the lifetime of the states to $\tau_{BB} \approx 60 \mu\text{s}$ at 300 K [72].

Rabi oscillations of the two-photon $49s_{1/2} - 48s_{1/2}$ transition for a continuously applied microwave pulse are shown in Fig. 4.2. The oscillations begin to dephase within a few cycles due to microwave field inhomogeneities but a reasonable amount of coherence is maintained for sequences with a few relatively short manipulations, such as a Ramsey experiment or single-pulse spin-echo sequence.

A microwave spectrum of the $49s_{1/2} - 48s_{1/2}$ transition, for a weak $5 \mu\text{s}$ pulse, is shown in Fig. 4.3. This measurement of the resonance frequency is an important step, since any residual uncompensated dc electric field (as well as electric field noise) will shift the transition. Ramsey-type experiments show oscillations in the measured populations at a frequency equal to the detuning of the microwaves from the transition. For small detunings (tens of kHz) this oscillation frequency is comparable to the decay time of the coherence and complicates the analysis. One solution is to detune the microwaves by a relatively large amount to create oscillations in the MHz frequency range and then determine the decay of the envelope (as has been done in Fig. 4.4), but this approach tends to require more data points for the same degree of accuracy.

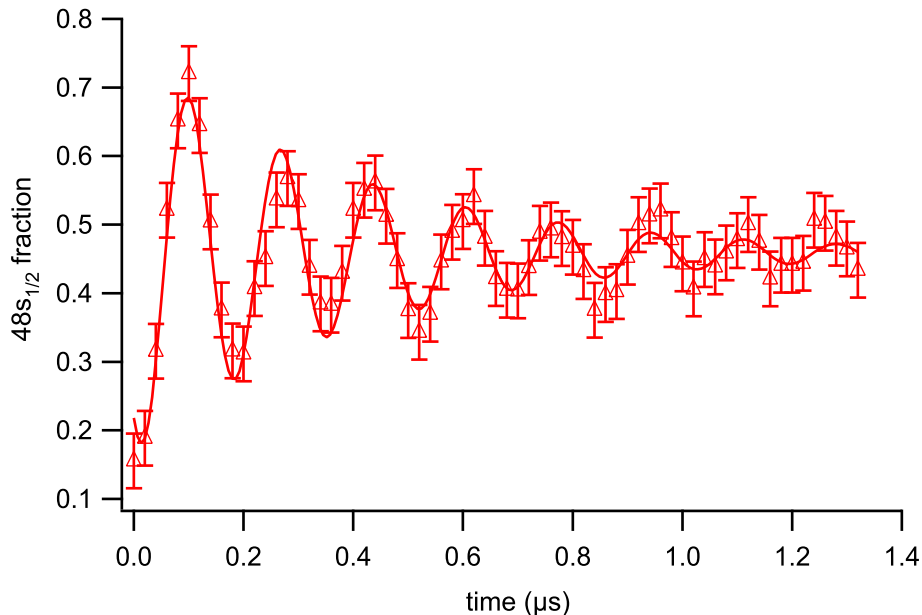


Figure 4.2: Rabi flopping of the two-photon $49s_{1/2} - 48s_{1/2}$ transition.

The Stark shift $\Delta\omega_{01} = 2\pi \times 240 \pm 20$ kHz is consistent with $\langle F^2 \rangle = 800$ V²/m². This can be used to establish an upper bound for any field noise, since $\langle F^2 \rangle \leq \int_{-\infty}^{\infty} S_F(\omega)$ (dc field inhomogeneities not associated with S_F may also contribute to $\langle F^2 \rangle$). In the case of $1/f$ noise, with $S_F(\omega) = S_0/\omega^\kappa$, $\langle F^2 \rangle \leq 2 \int_{\omega_{ir}}^{\omega_c} S_0/\omega^\kappa$. The measurement sequence, with $5 \mu\text{s}$ microwave pulses and a 2 Hz repetition rate, results in $\omega_c \approx 2 \times 10^5$ s⁻¹ and $\omega_{ir} \approx 0.2$ s⁻¹ when 10 measurements are averaged at each point in Fig. 4.3. This constrains $S_0 \leq 1.8$ (V/m)²s^{-1/2} for $\kappa = 1/2$, $S_0 \leq 120$ (V/m)² for $\kappa = 1$, and $S_0 \leq 360$ (V/m)²s^{1/2} for $\kappa = 3/2$.

Results of a Ramsey-sequence measurement are shown in Fig. 4.4. The $\pi/2$ pulses in this measurement were 50 ns long. The microwaves are detuned from the two-photon resonance by 1 MHz, creating oscillations in the population with time. This large detuning removes any possible confusion caused by small dc Stark shifts moving energy levels slightly out of resonance. An additional benefit is that any systematic offsets in the measured

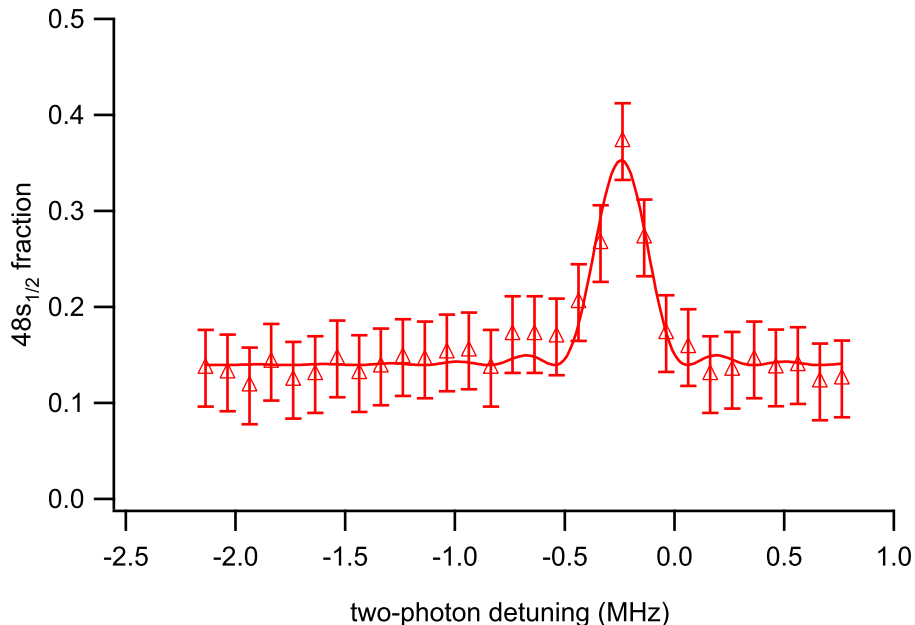


Figure 4.3: Two-photon microwave spectrum of the $49s_{1/2} - 48s_{1/2}$ transition. The transition is Stark shifted from the zero-field resonance by 240 ± 20 kHz.

$48s_{1/2}$ fraction may be determined from the fit—the populations of the $48s_{1/2}$ and $49s_{1/2}$ states should be equal for long times when the coherence decays completely. Fitting an exponential decay to the envelope for the entire range of free evolution times gives a time constant $\tau_R = 3.1 \pm 0.8 \mu\text{s}$. Therefore, the measurement is not in the $t \gg \tau$ regime necessary to determine S_0 from the decay constant. Fitting the decay of the form in Eq. 3.23, expected for pure $1/f$ noise at short times, gives $\gamma_f = 1.6 \pm 1.4 \times 10^5 \text{ s}^{-1}$ (taking $\omega_{ir} = 0.2 \text{ s}^{-1}$). This result is consistent with S_0 in the range of $11 - 160 (\text{V/m})^2$.

Results of a Hahn spin-echo sequence are shown in Fig. 4.5, along with the previous Ramsey-sequence data for comparison. The $\pi/2$ pulses in this measurement were 50 ns long, and the π -pulse was 100 ns long. Constraining the $48s_{1/2}$ fraction at long times to the same value as the previous Ramsey experiment, the time constant of exponential decay of the coherence is $\tau_{SE} = 7.2 \pm 1.9 \mu\text{s}$.

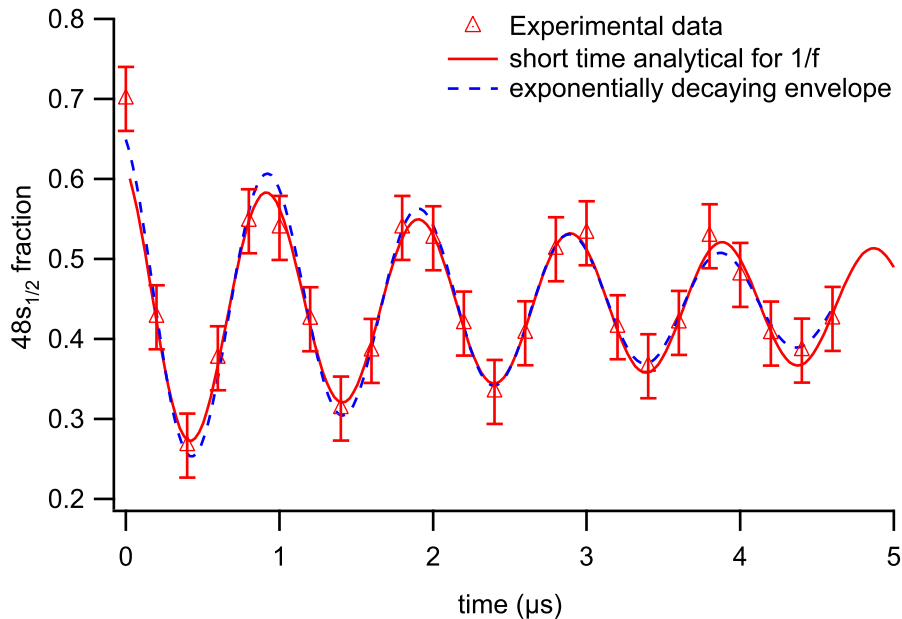


Figure 4.4: Ramsey sequence for the two-photon $49s_{1/2} - 48s_{1/2}$ transition, with the microwaves detuned from the two-photon resonance by 1 MHz.

This measurement is not in the $t \gg \tau$ regime necessary for a precise determination of S_0 from τ_{SE} . However, τ_{SE} is significantly shorter than τ_{BB} , the decay time expected in the absence of high-frequency field noise, with population relaxation as the dominant mechanism of decoherence. At the same time, $\tau_{SE} < \tau_R$ is consistent with the spin-echo sequence effectively reducing decoherence due to dc and low-frequency ac inhomogeneous fields.

Taking $1/\tau_{BB}$ as a rough lower limit for the contribution of high-frequency ac field noise to the decoherence rate, the results of Section 3.6.1 may be used to set a lower bound for any $1/f$ noise: $S_0 > 0.05 (\text{V/m})^2$ for $\kappa = 1/2$, $S_0 > 20 (\text{V/m})^2$ for $\kappa = 1$, and $S_0 > 2 \times 10^3 (\text{V/m})^2$ for $\kappa = 3/2$. The upper limit calculated here for $\kappa = 3/2$ is inconsistent with the lower limit of S_0 established spectroscopically. Therefore, the noise

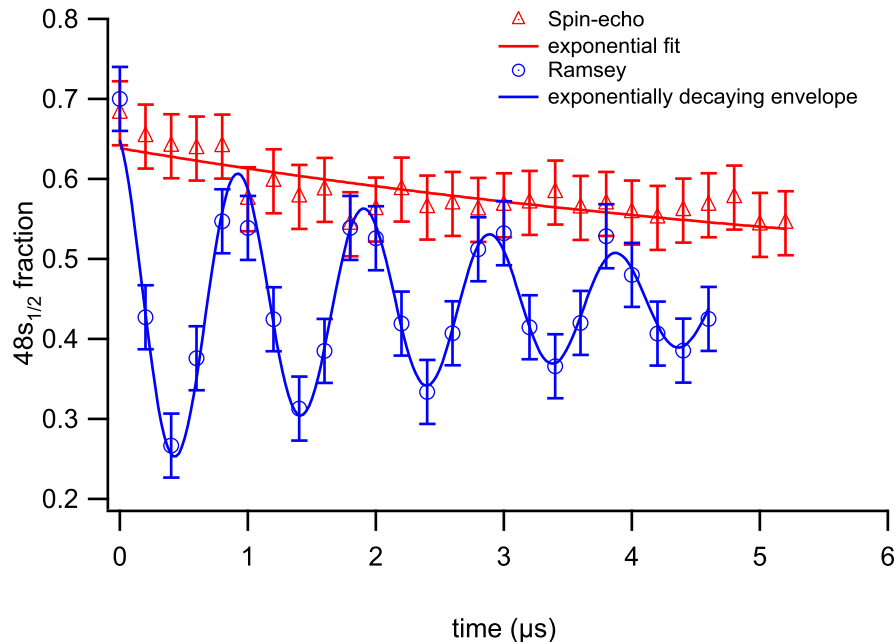


Figure 4.5: Hahn spin-echo sequence for the two-photon $49s_{1/2} - 48s_{1/2}$ transition, with the microwaves detuned from the two-photon resonance by 1 MHz.

power spectrum does not follow a $1/f^{3/2}$ frequency scaling. However, the measurements are consistent with both $1/f^{1/2}$ and $1/f$ frequency scalings of the power spectrum.

Far from the surface the dominant source of electric field noise is unlikely to be patch fields but rather voltage noise between the field plates. The origins of the noise may well be technical. Measurements of τ_{SE} at longer times will help to more accurately constrain the magnitude of S_0 for a given κ value. Measurements of $S_F(\omega)$ using spin-locking techniques would serve to further constrain the frequency scaling of the noise as well as identifying any sharp peaks in the noise power spectrum likely to be of technical origin.

4.4 Microwave field homogeneity

The microwaves used to manipulate the atoms are not completely homogeneous over the sample volume, due to standing waves caused by reflections from the chamber walls and components. In particular, the experimental geometry, shown in detail in Fig. 4.1, has microwaves propagating down the long axis of the microtrap and reflecting from the back flange of the chamber (the complete apparatus diagram can be found in Fig. 2.1). This reflection creates a standing wave pattern along the length of the microtrap, causing field inhomogeneity that limits the fidelity of operations. The homogeneity of the microwave field over the Rydberg atom sample can be improved by focusing the 780 nm excitation beam to limit the sample volume and centering the sample at a maximum in the microwave standing wave pattern. Unfortunately, this reduces the population of Rydberg atoms in the sample, which worsens signal/noise.

The standing wave can be clearly seen by measuring the Rabi frequency of a microwave Rydberg transition in small samples of Rydberg atoms created at various points along the length of the microtrap, as in Fig. 4.6, while keeping the applied microwave power constant. The size and position of the Rydberg sample are determined by the crossed 780 nm and 480 nm lasers used in the two-photon excitation; here the diameter of the 780 nm beam limits the extent of the sample in the direction of microwave propagation and steering of this beam moves the sample along this direction. For the data shown in Fig. 4.6, the Rydberg atoms are optically excited to the $36s_{1/2}$ state after release from the microtrap, with the Rydberg cloud centered $230 \mu\text{m}$ from the surface. The excitation volume defined by the lasers is $200 \mu\text{m}$ long and $60 \mu\text{m}$ in diameter.

The two-photon Rabi frequency varies by a factor of four, consistent with a factor of two variation in the microwave field strength between standing wave minima and maxima. The variation is sinusoidal with a period of 1.9 mm, reasonably consistent with the 1.68 mm vacuum half-wavelength of the microwaves.

For a particular location and size of the Rydberg sample, the microwave inhomogeneity can be measured *in situ* with a non-resonant microwave dressing field used to modify the energy of a transition via the AC Stark shift. The Stark shift is proportional to the square

of the dressing field amplitude, so the transition will shift and broaden in proportion to the microwave power as the dressing field is increased, as seen in Fig. 4.7.

With the same 38.1 GHz dressing field and trap geometry employed previously, Fig. 4.8 shows the effect of reducing the extent of the Rydberg atom sample size. The 780 nm beam was focused and steered to reduce the sample from 2 mm long, with the dressing field standing wave maximum near one end of the sample, to 0.5 mm long, centered around the maximum. The broadening, relative to the shift, gives the microwave field inhomogeneity $\Delta(F^2)/(F^2)$. For the measurements shown, the broadening is sufficiently large compared to the natural linewidth that the line shape may be assumed to be Gaussian rather than Lorentzian, with the width determined by a fit to a Gaussian. The measurements are consistent with standard deviations in the microwave field amplitude of $\Delta F/F \approx 30\%$ for the large sample and $\Delta F/F \approx 20\%$ for the small sample. This is likely an overestimate of the microwave field inhomogeneity, as ellipticity in the dressing field polarization splits the probe transition [75], and small values of the splitting will appear as broadening of the line.

As an alternate method, an upper bound for the microwave field inhomogeneity can be extracted from the decay rate of Rabi oscillations. The envelope of the oscillations is assumed to decay exponentially with time constant τ , and therefore a useful figure of merit is $\Omega\tau$, the product of this time constant and the Rabi frequency.

The amount of field inhomogeneity associated with the observed decay rate can be determined through Monte Carlo simulation of the decay. For a given statistical distribution of field amplitudes in the sample, the decay rate of coherence is calculated by summing the Rabi oscillations of a large number of atoms, each exposed to a random microwave field amplitude. Two models for the distribution of field amplitudes are considered. The first model is Gaussian distribution of the amplitudes around the average, an appropriate treatment if a large number of random parameters affect the field at the atom's location. In this model, an appropriate parametrization of the field inhomogeneity is σ_F , the standard deviation of the field amplitude. The second model assumes the dominant contribution to the amplitude is given by the atom's displacement from the standing wave maximum. Here the sample is assumed to be sufficiently small that the field amplitude varies as the square of displacement, $F(x) = F_{max} - \Delta x^2$, and atoms are uniformly distributed along x .

An appropriate parametrization for this model is Δ_F , the maximum deviation of F from F_{max} , which occurs at the ends of the sample.

Calculated decoherence rate as a function of field homogeneity for the two models considered is shown in Fig. 4.9, for one-photon ($\omega \propto F$) and two-photon ($\omega \propto F^2$) transitions. With the length of the Rydberg atom sample restricted to $\approx 200 - 300 \mu\text{m}$, the typical coherence decay rate measured for two-photon transitions is $\Omega\tau \approx 5 - 6$, with a typical measurement shown in Fig. 4.10. This result is consistent with field inhomogeneity $\sigma_F/F \approx 0.02$ or $\Delta_F/f \approx 0.05 - 0.1$ for the models discussed.

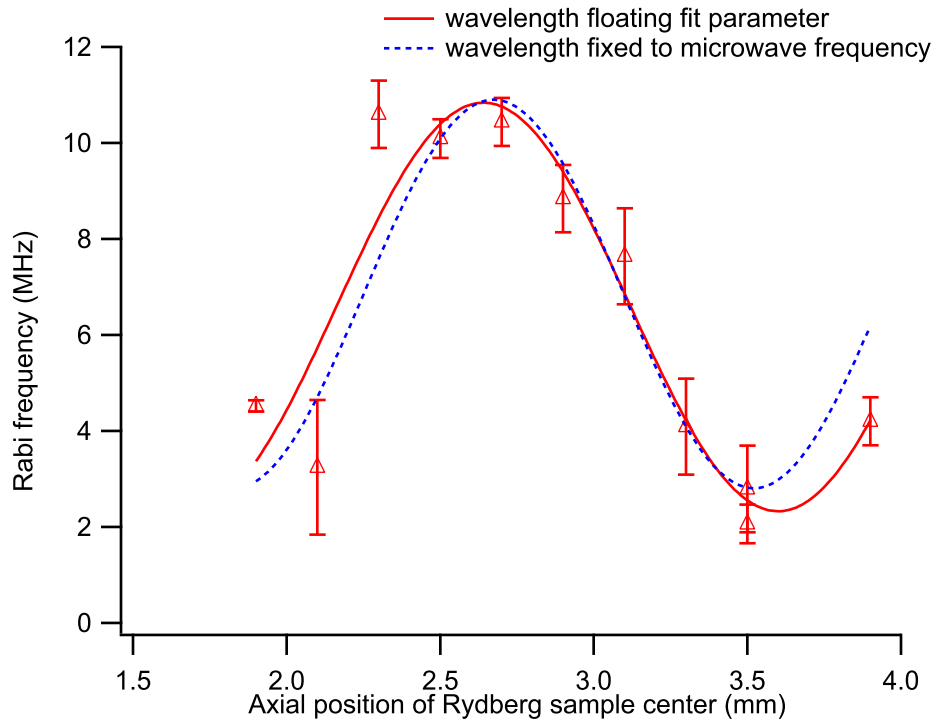


Figure 4.6: Two-photon Rabi frequency as a function of axial position. The variation is due to microwave field inhomogeneities caused by reflections in the vacuum chamber. Two sinusoidal fits are shown, one with the period of the standing wave allowed to vary freely in the fit and the other where the period of the standing wave is fixed by the microwave frequency.

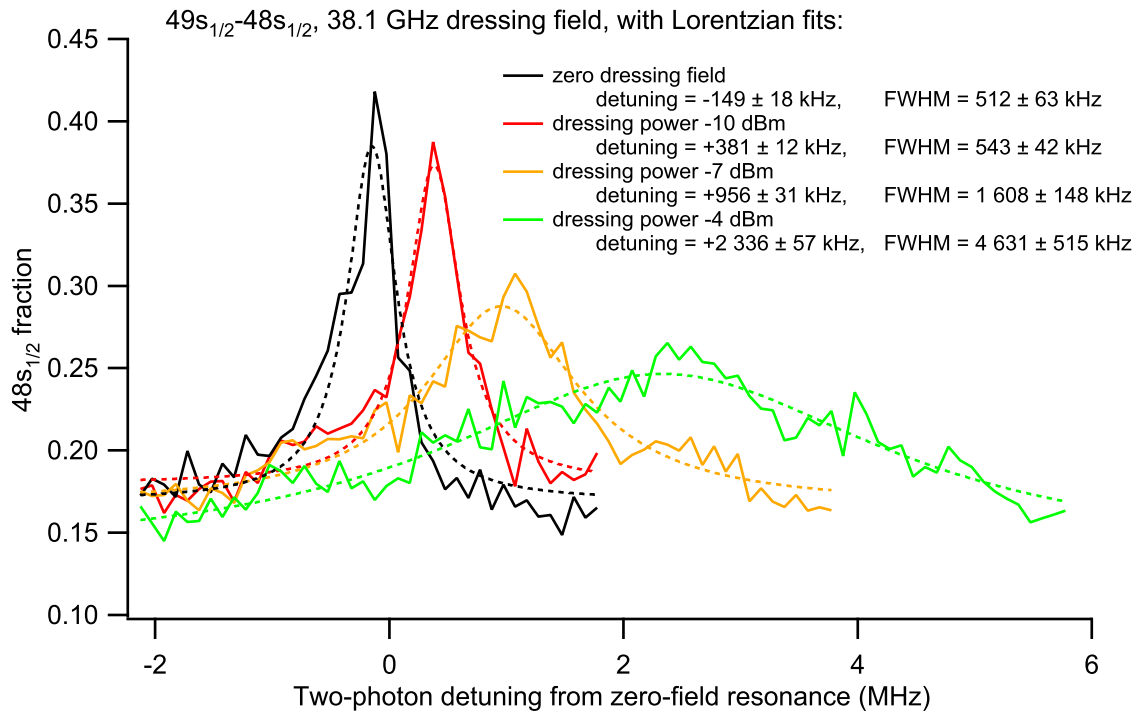


Figure 4.7: AC Stark shifting and broadening of the $49s_{1/2} \rightarrow 48s_{1/2}$ transition of ^{87}Rb with a non-resonant dressing field at 38.1 GHz. The shift is linear with applied microwave power. The sample consisted of cold atoms released from the MOT, with a diameter of $60\ \mu\text{m}$ and a length of 2 mm.

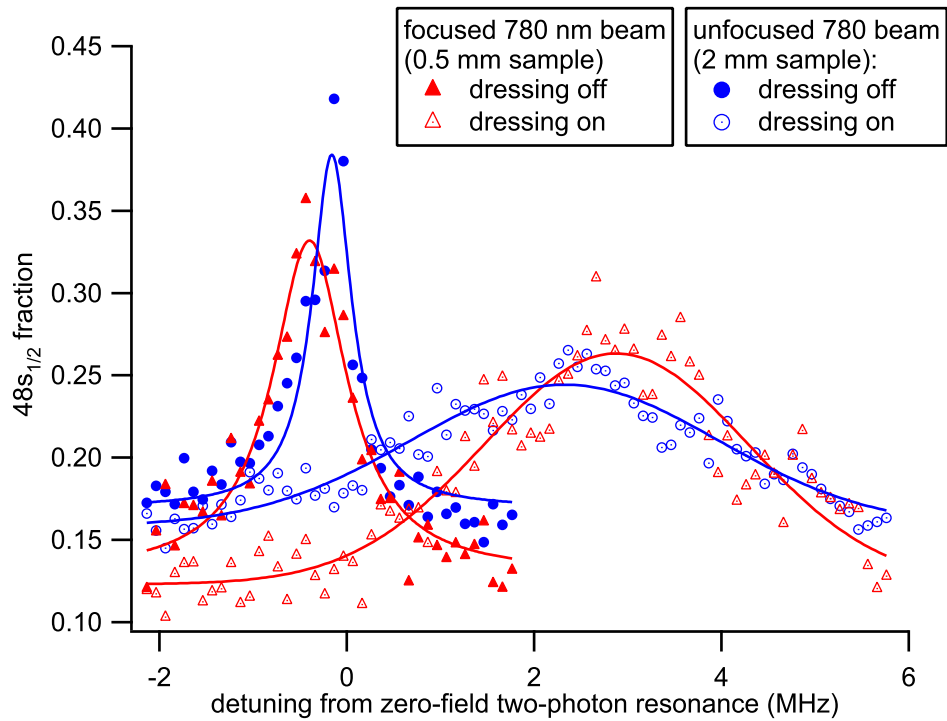


Figure 4.8: AC Stark shifting and broadening of the $49s_{1/2} \rightarrow 48s_{1/2}$ transition of ^{87}Rb with a non-resonant dressing field at 38.1 GHz. This measurement shows improvement of microwave field homogeneity achieved by reducing the length of the Rydberg atom sample from 2 mm to 0.5 mm.

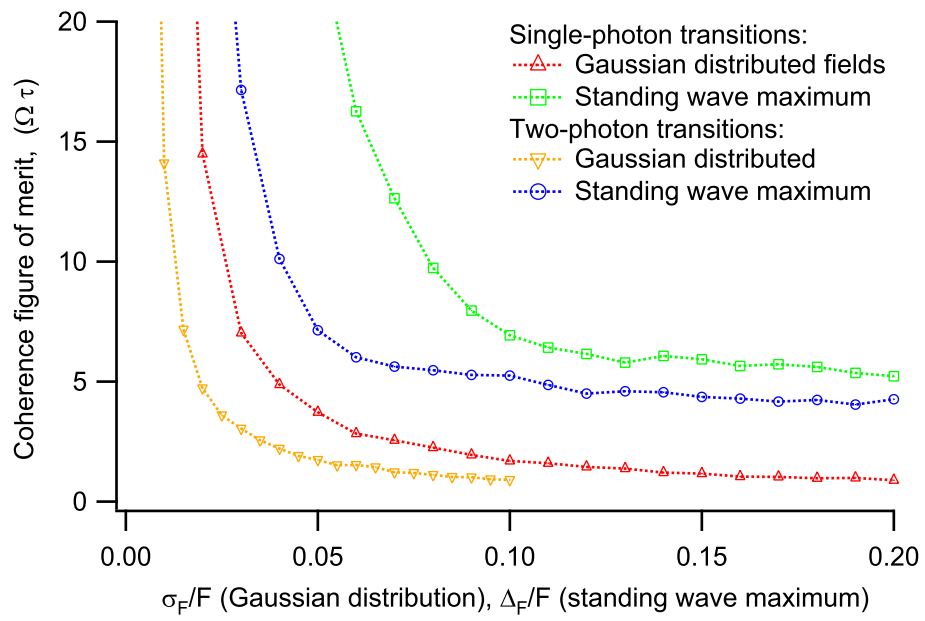


Figure 4.9: Effect of microwave homogeneity on the decay rate of Rabi oscillations, for one-photon ($\Omega \propto F$) and two-photon ($\Omega \propto F^2$) transitions.

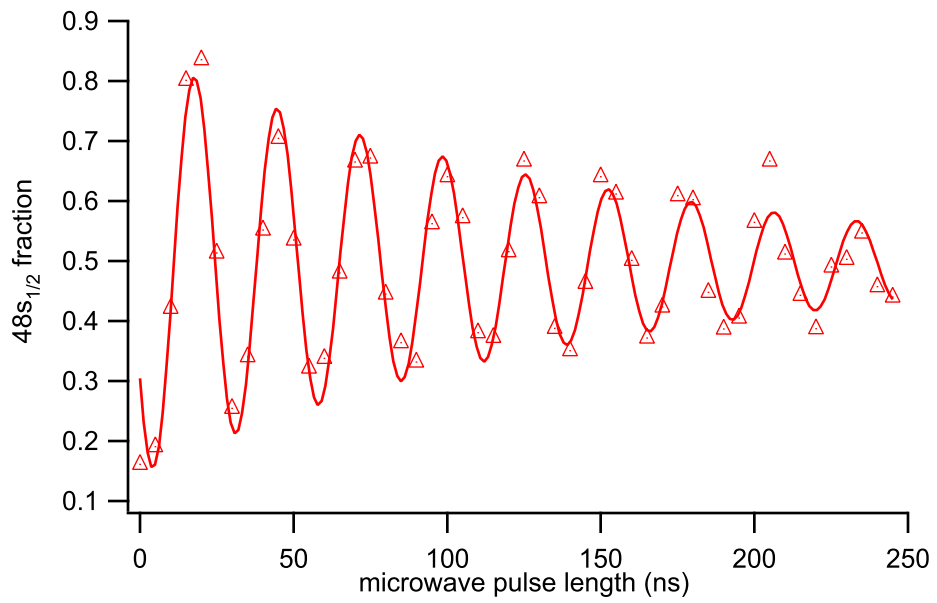


Figure 4.10: Rabi oscillations between the $49s_{1/2}$ and $48s_{1/2}$ states, fitted to an exponentially-damped cosine. Here the Rabi frequency $\Omega = 2\pi \times (37.10 \pm 0.14 \text{ MHz})$, with coherence time $\tau = 150 \pm 20 \text{ ns}$, for $\Omega\tau = 5.43$.

4.5 Intermediate state population in two-photon resonances

When driving the $49_{1/2} - 48s_{1/2}$ transition, electric dipole selection rules allow population to be driven via the intermediate $48p_{1/2}$ and $48p_{3/2}$ states. These intermediate states are indistinguishable from the $49s_{1/2}$ state during selective field ionization, so excessive population of the intermediate states complicates interpretation of the experimental results.

The $48p_{3/2}$ state is the dominant contributor to the coupling, as it has the largest transition dipole matrix elements (couplings of 1086 atomic units to $48s_{1/2}$ and 1059 atomic units to $49s_{1/2}$) and the smallest single-photon detuning $\Delta = 161.1$ MHz. In comparison, the $48p_{1/2}$ state has transition dipole matrix elements of 780 atomic units to $48s_{1/2}$ and 735 atomic units to $49s_{1/2}$, and $\Delta = 1.093$ GHz. Neglecting the contribution of the $48p_{1/2}$ state would lead to an error in the determination of Ω_{R2} of about 7 %.

A numerical simulation of the state populations for a Ramsey experiment creating a coherent superposition of the $49s_{1/2}$ and $48s_{1/2}$ states is shown in Fig. 4.11. The $\pi/2$ pulses are resonant with this two-photon transition. The pulses are 50 ns long and separated by 150 ns, with the amplitude envelopes modeled as square pulses with ramps of 1 ns. The corresponding electric field amplitude $F_0 = 2.862$ V/m. For the $|a\rangle = 48p_{3/2}$ intermediate state, the single-photon Rabi frequencies are $\Omega_{ia} = 38.77$ MHz and $\Omega_{af} = 39.75$ MHz, a significant fraction of Δ , and therefore Eq. 3.28 predicts significant $48p_{3/2}$ population. The simulation assumes ideal conditions, with homogeneous microwave fields and no ambient dc or slowly varying ac fields.

During the first pulse, the maximum $48p_{3/2}$ population is 4.9%. The behaviour during subsequent pulses depends sensitively on the pulse timings, durations, and amplitudes, as these affect the relative phases of the states involved. When realistic inhomogeneities in the microwave amplitude and electric field environment are considered, coherence between the $48p_{3/2}$ states and the other states in the problem decays relatively quickly, and simulated Ramsey or spin-echo sequences using pulses of this length typically conclude with 5 – 10% of the population in the $48p_{3/2}$ state. This is reasonably consistent with typically measured

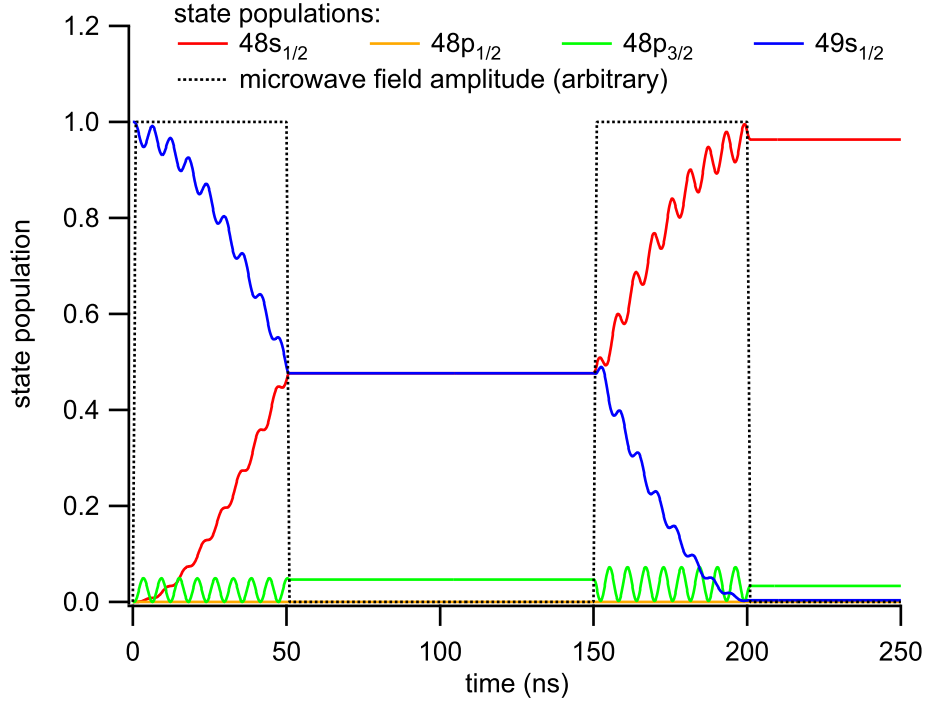


Figure 4.11: Calculated time-evolution of the state populations for a two-photon Ramsey experiment using the transition between $49s_{1/2} \rightarrow 48s_{1/2}$. The $\pi/2$ pulses are 50 ns long.

$48s_{1/2}$ fractions of ≈ 0.45 for long decay sequences where equal populations of $48s_{1/2}$ and $49s_{1/2}$ are expected.

There are several available methods to reduce the population of intermediate states. The microwave power may simply be reduced, at the cost of increasing rotation times to hundreds of ns. The amplitude of the microwave pulse may be shaped, analogous to pulse-shaping techniques of NMR [50]. However, these pulse-shaping sequences are often implemented with discrete time sequences of tens or even hundreds of amplitudes, requiring GHz-range modulation bandwidths for sub-100 ns pulses, and offering little practical advantage compared to simple rectangular pulses for longer pulses. It is possible in principle, even for strong fields, to select the field strength and pulse length in such a way that $\pi/2$ and π rotations of the $48s_{1/2} - 49s_{1/2}$ superposition coherently return the $48p_{3/2}$ population

to zero, as illustrated in Fig. 4.12. Unfortunately, suppression of the $48p_{3/2}$ excitation in this regime requires high microwave field homogeneity.

In cases where large differential Stark shifts between the two states of interest are not a problem (or are even desirable for increased sensitivity), eliminating the intermediate states entirely by switching to a single-photon transition is probably the best solution.

4.6 Summary

Far away from the chip surface, Rabi oscillations between the $49s_{1/2}$ and $48s_{1/2}$ states of ^{87}Rb have been observed. This observation demonstrates that the coherent control required for implementing spin-echo and spin-locking measurements of noise is possible using this apparatus. The results of microwave spectroscopy and the decay of Hahn spin-echo coherence have been used to bound the electric field noise amplitude measured several mm away from the surface of the chip. The results of these measurements are inconsistent with a noise power spectrum with frequency scaling $1/f^{3/2}$, but are consistent with frequency scalings of $1/f^{1/2}$ or $1/f$. The rate of decay of the Hahn spin-echo coherence is consistent with a power spectral density $S_F(\omega) \approx (20 \text{ V/m})/\omega$ if the noise is assumed to be pure $1/f$. This noise amplitude is about four orders of magnitude larger than the field noise typically seen by ions trapped much closer to the surface [11], suggesting that the origin of the dominant noise source may be technical.

A significant standing wave pattern in the microwave fields in the experimental chamber has been observed. Improvement of the microwave field homogeneity by restricting the sample volume has been demonstrated. The microwave field homogeneity over these small samples of Rydberg atoms has been measured using the decay of coherent Rabi oscillations. The amount of undesired excitation of the $48p_{3/2}$ state has been estimated using numerical simulations to be ($p \approx 0.05$). Various strategies for minimizing this effect have been discussed.

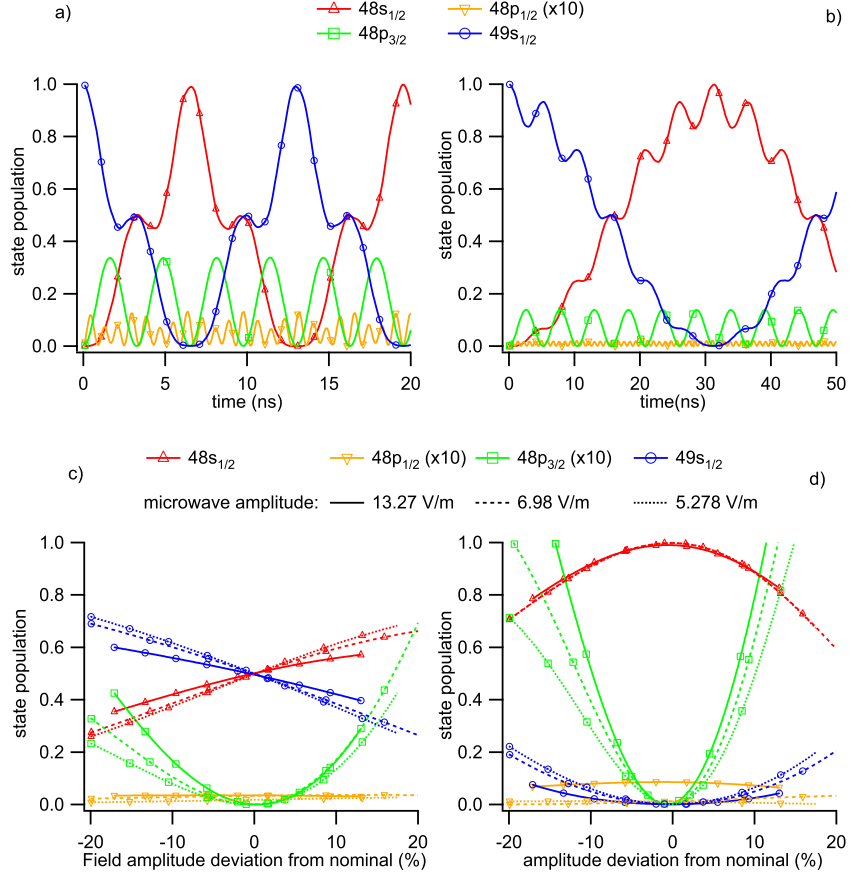


Figure 4.12: Numerical simulations of intermediate state populations for various microwave amplitudes.

(a),(b): Time-evolution of the state populations with the two-photon $49s_{1/2} \rightarrow 48s_{1/2}$ transition driven resonantly by microwaves with amplitudes chosen so that $\Omega_a = 4n\Omega_{2R}$ and therefore the $48p_{3/2}$ population is zero after every $\pi/2$ rotation. Field amplitudes are: (a) 13.27 V/m for $n = 1$ and (b) 5.278 V/m for $n = 3$.

(c),(d): Robustness of square-wave (c) $\pi/2$ - and (d) π -pulses to inhomogeneities in the microwave field, for field amplitudes of 13.27, 6.98, and 5.278 V/m corresponding to $n = 1, 2,$ and 3 respectively.

Chapter 5

Energy shifts of Rydberg atoms due to patch fields near metal surfaces

This chapter is based directly on a paper published by the author, together with J. D. D. Martin [9].

5.1 Summary

The statistical properties of patch electric fields due to a polycrystalline metal surface are calculated. The fluctuations in the electric field scale like $1/z^2$, when $z \gg w$, where z is the distance to the surface, and w is the characteristic length scale of the surface patches. For typical thermally evaporated gold surfaces these field fluctuations are comparable to the image field of an elementary charge, and scale in the same way with distance to the surface. Expressions for calculating the statistics of the inhomogeneous broadening of Rydberg-atom energies due to patch electric fields are presented. Spatial variations in the patch fields over the Rydberg orbit are found to be insignificant.

5.2 Introduction

Excitation to a Rydberg state enhances an atom’s interaction with a metal surface. At large atom-surface distances, this results in energy level shifts that can be calculated using first-order perturbation theory [76]. At smaller distances, the influence of the surface is more drastic—the Rydberg atom can be “field-ionized” by the surface [77, 19]. These phenomena may be visualized as arising from the interaction of the Rydberg atom with the electric fields due to its electrostatic “image.” Compared to an atom in the ground state, a Rydberg atom has an enhanced susceptibility to these fields. This is because the Rydberg electron experiences a greatly reduced electric field from the ion core due to their larger average separation.

Polycrystalline metal surfaces generate inhomogeneous “patch” electric fields outside of their surfaces [78]. These fields may also influence Rydberg atoms, potentially causing both level shifts and ionization and competing with the more intrinsic image charge effects. In general, patch fields arise from the individual grains of a polycrystalline surface exposing different faces of the bulk crystal. Each face has a different work function due to differing surface dipole layers [79]. For example, Singh-Miller and Marzari [80] have recently calculated the work functions of the (111), (100), and (110) surfaces of gold and found 5.15, 5.10, and 5.04 eV, respectively. These differing work functions correspond to potential differences just outside the surface beyond the dipole layer. Consequently, charge density must be redistributed on the surface to satisfy the electrostatic boundary conditions, producing macroscopic electric fields [79]. While patch fields were first discussed extensively in the context of thermionic emission [78], they may be present near polycrystalline metal structures of any type, including electrodes and electrostatic shields.

Recent advances in the trapping of cold atoms near surfaces have opened up the possibility of precision studies of Rydberg-atom–surface interactions as a function of atom-surface distance. For example, Tauschinsky et al. [18] have recently observed electromagnetically induced transparency due to Rydberg excitation of atoms at 10 μm to 200 μm away from a gold surface. Lesanovsky *et al.* [81] have calculated some interesting properties of Rydberg atoms exposed to inhomogeneous magnetic fields due to magnetic microtraps, and Crosse et al. [82] have recently calculated level shifts and transition rates of rubidium atoms near

a copper surface at room temperature. In addition, there are several quantum information proposals that will involve Rydberg atoms in proximity to metal surfaces [4, 83, 29]. Consequently, it is desirable to be able to estimate the influence of patch fields on Rydberg atoms. In this paper, we examine relevant models of the surface, report on the statistics of the patch fields, and determine the influence of these fields on Rydberg-atom energies. We assume that the atom-surface distance is large compared to other relevant length scales and that the atomic energy level shifts can be treated using perturbation theory.

The model we adopt for the patch fields is similar to one used by Rzchowski and Henderson [8]. Their work was motivated by the Witteborn-Fairbank experiment [84], which was intended to compare the force of gravity on electrons and positrons. Due to the relatively weak gravitational force, electrostatic shielding was necessary—the charged particles traveled down the axis of a hollow copper cylinder used for shielding. It was important to understand the variations in electrostatic potential along the axis of this tube due to patch fields, and Rzchowski and Henderson obtained results relevant to this geometry. In the present work, we concentrate on a planar surface and the statistical properties of the electric field and its spatial derivatives.

5.3 Rydberg-atom energy shifts in external fields

We first calculate the energy-level shifts of a single atom in response to the local electrostatic potential $V(x, y, z)$ created by the patches. This will allow us to calculate the statistics of the energy shifts once the statistics of the patch fields are known.

We consider an addition to the atom’s Hamiltonian H_0 of the form [85]

$$\begin{aligned}
 H_1 = & \sum_i \mu_i D_i V(x, y, z) \\
 & + \frac{1}{6} \sum_{i,j} Q_{i,j} D_i D_j V(x, y, z) + \dots,
 \end{aligned}
 \tag{5.1}$$

where μ_i and $Q_{i,j}$ are the dipole and quadrupole moment operators, respectively, and D_i is the operator representing the derivative with respect to the i th argument. The quadrupole

and higher-order moments will allow us to consider the influence of an electric field varying over the extent of the atom—of particular interest because Rydberg atoms are much larger than ground-state atoms.

We will consider the shift given in Eq. (5.1) using first-order perturbation theory. In the absence of preexisting external fields, there would normally be no contribution from the dipole term to the first-order shift. However, we will assume that a dc electric field aligned with the surface normal \hat{z} has been applied. This may be done to enhance sensitivity to patch fields, break degeneracies, or for technical reasons (see, for example, Ref. [29]). The effect of this field is incorporated into H_0 . Our basis states (eigenstates of H_0) will be considered to have a cylindrically symmetric charge distribution about the surface normal. This symmetry constricts the moments, so that $\mu_x = \mu_y = 0$, $Q_{xx} = Q_{yy} = -\frac{1}{2}Q_{zz}$, etc.

Equation (5.1) involves the evaluation of arbitrary order mixed derivatives of the potential in all three spatial dimensions. However, the introduction of cylindrical symmetry allows a considerable relaxation in this requirement if spherical (instead of cartesian) multipole moments are used. Therefore, the external potential due to the patches is expanded in the form

$$V = \sum_{\ell,m} d_{\ell,m} r^\ell C_{\ell,m}(\theta, \phi) \quad (5.2)$$

about the location of the atom, where $d_{\ell,m}$ are the expansion coefficients, r is the distance away from the center of the expansion, θ and ϕ the normal spherical coordinates with the polar axis aligned with the surface normal, and $C_{\ell,m}$ are rescaled spherical harmonics; $C_{\ell,m} = \sqrt{4\pi/(2\ell+1)}Y_{\ell,m}$.

To obtain an expression analogous to Eq. (5.1), this new expansion of the potential is substituted into the volume integral for the electrostatic energy due to a charge distribution ρ in an external potential, $E = \int d\tau \rho V$, with $d\tau$ as the differential volume element. We obtain

$$E = \sum_{\ell} d_{\ell,0} \int d\tau \rho r^\ell P_{\ell}(\cos \theta), \quad (5.3)$$

where terms involving $m \neq 0$ do not appear, due to the cylindrical symmetry of the charge distribution, and P_{ℓ} are the Legendre polynomials ($= C_{\ell,0}$). The values of the $d_{\ell,0}$ coefficients in the expansion can be readily determined from Eq. (5.2) by evaluating the

derivatives of the potential with respect to the distance to the surface z evaluated at the origin of the expansion, giving $d_{\ell,0} = (1/\ell!)D_z^\ell V(x, y, z)$, where D_z^ℓ means take the ℓ th derivative with respect to the z coordinate. The first-order energy shift can be written in a form that only depends on the gradients of the field in the z direction evaluated at the location of the atom:

$$E_1 = \sum_{\ell} M_{\ell} [D_z^{\ell} V(x, y, z)], \quad (5.4)$$

where M_{ℓ} has been introduced to simplify notation. To evaluate these matrix elements, we assume that only the charge distribution due to the Rydberg electron needs to be accounted for, so that $M_{\ell} = (1/\ell!)q_e \langle \psi_0 | r^{\ell} C_{\ell,0} | \psi_0 \rangle$, where q_e is the electron charge, and $|\psi_0\rangle$ are the energy eigenstates of the zeroth order Hamiltonian H_0 . The values of M_{ℓ} are proportional to the normal spherical multipole moments (see, for example, Ref. [86]).

5.4 Statistics of the patch fields

As shown in the previous section, the energy of any particular atom depends on the field at its location. Consider an ensemble of atoms placed a certain distance z away from the surface. In general, the patch fields are statistical in nature, so that spatial inhomogeneities in the field will cause an inhomogeneous broadening in the ensemble. We can characterize this by the variance in the energy of a given state, calculated using Eq. (5.4), assuming that the average shift is zero:

$$\langle (\Delta E)^2 \rangle_C = \sum_{\ell, \ell'} M_{\ell} M_{\ell'} \left\langle \left[D_z^{\ell} V(x, y, z) \right] \left[D_z^{\ell'} V(x, y, z) \right] \right\rangle_C, \quad (5.5)$$

where $\langle \dots \rangle_C$ is used to specify an ensemble (classical) expectation value.

Therefore, to calculate the variance of atomic energy levels $\langle (\Delta E)^2 \rangle_C$ due to the statistical fluctuations in the field above the surface, we will develop expressions for $\langle [D_z^{\ell} V(x, y, z)] [D_z^{\ell'} V(x, y, z)] \rangle_C$. For example, the most important statistical fluctuation

for Rydberg energy level shifts is of the electric field in the z direction, which can be characterized by its root mean square (rms) value: $[\langle F_z^2 \rangle - \langle F_z \rangle^2]^{1/2}$, which is given by $\{\langle [D_z^1 V(x, y, z)][D_z^1 V(x, y, z)] \rangle_C\}^{1/2}$.

To calculate these statistical averages, we start by considering the solution of Laplace's equation $\nabla^2 V(x, y, z) = 0$ above a plane surface when the potential on the surface is specified. One particular solution of Laplace's equation is: $V(x, y, z) = V_0 e^{ik_x x + ik_y y} e^{-kz}$, where $k = \sqrt{k_x^2 + k_y^2}$ and k_x, k_y and V_0 are constants. Consider the following superposition of similar solutions (all integrations are assumed to run from negative to positive infinity, unless otherwise specified):

$$V(x, y, z) = \int dk_x dk_y \tilde{V}(k_x, k_y) e^{ik_x x + ik_y y} e^{-kz}. \quad (5.6)$$

We may use this expression to determine the potential over any surface in the plane $z = 0$ with a defined potential $V_s(x, y)$ by using the inverse Fourier transform to determine $\tilde{V}(k_x, k_y)$:

$$\tilde{V}(k_x, k_y) = \frac{1}{(2\pi)^2} \int dx dy V_s(x, y) e^{-ik_x x - ik_y y}. \quad (5.7)$$

Putting Eqs. (5.6) and (5.7) together gives

$$V(x, y, z) = \frac{1}{(2\pi)^2} \int dk_x dk_y e^{ik_x x + ik_y y} e^{-kz} \times \int dx' dy' V_s(x', y') e^{-ik_x x' - ik_y y'}. \quad (5.8)$$

Consider the covariance between derivatives of the field evaluated at two points a and b in space, determined using the preceding equation:

$$\begin{aligned} & \left\langle \left[D_p^\ell V(x_a, y_a, z_a) \right] \left[D_q^{\ell'} V(x_b, y_b, z_b) \right] \right\rangle_C \\ = & \frac{1}{(2\pi)^4} \int dk_{x,a} dk_{y,a} dk_{x,b} dk_{y,b} dx'_a dy'_a dx'_b dy'_b \\ & \exp[ik_{x,a} x_a + ik_{y,a} y_a - k_a z_a - ik_{x,a} x'_a - ik_{y,a} y'_a \\ & - ik_{x,b} x_b - ik_{y,b} y_b - k_b z_b + ik_{x,b} x'_b + ik_{y,b} y'_b] \\ & \times (\alpha_{p,a})^\ell (\alpha_{q,b}^*)^{\ell'} \times \langle V_s(x'_a, y'_a) V_s(x'_b, y'_b) \rangle_C, \end{aligned} \quad (5.9)$$

where $\alpha_{1,a} = ik_{x,a}$, $\alpha_{2,a} = ik_{y,a}$, $\alpha_{3,a} = -k_{z,a}$, $\alpha_{1,b} = ik_{x,b}$, $\alpha_{2,b} = ik_{y,b}$ and $\alpha_{3,b} = -k_{z,b}$. As Eq. (5.5) shows, we only need $p = q = 3$ (derivatives in the z direction), but it is not difficult to deal with this slightly more general form, which will also allow us to calculate additional quantities, possibly of use to others, such as the total rms electric field.

We now make an assumption about the statistical nature of the field: the correlation function C for the surface potential only depends on the separation between the two points a' and b' (i.e., it is a “stationary” process):

$$\langle V_s(x'_a, y'_a) V_s(x'_b, y'_b) \rangle_C \equiv C(x'_b - x'_a, y'_b - y'_a), \quad (5.10)$$

and rewrite Eq. (5.9) using $\Delta x' = x'_b - x'_a$, and $\Delta y' = y'_b - y'_a$:

$$\begin{aligned} & \left\langle \left[D_p^\ell V(x_a, y_a, z_a) \right] \left[D_q^{\ell'} V(x_b, y_b, z_b) \right] \right\rangle_C = \\ & \frac{1}{(2\pi)^4} \int dk_{x,a} dk_{y,a} dk_{x,b} dk_{y,b} dx'_a dy'_a d(\Delta x') d(\Delta y') \\ & \exp[ik_{x,a}x_a + ik_{y,a}y_a - k_a z_a - ik_{x,a}x'_a - ik_{y,a}y'_a \\ & - ik_{x,b}x_b - ik_{y,b}y_b - k_b z_b \\ & + ik_{x,b}(\Delta x' + x'_a) + ik_{y,b}(\Delta y' + y'_a)] \\ & \times (\alpha_{p,a})^\ell (\alpha_{q,b}^*)^{\ell'} \times C(\Delta x', \Delta y'). \end{aligned} \quad (5.11)$$

Use of the familiar relationship:

$\int dx' \exp[ix'(k_a - k_b)] = 2\pi\delta(k_a - k_b)$, where $\delta(\dots)$ is the Dirac δ function, allows simplification to

$$\begin{aligned} & \left\langle \left[D_p^\ell V(x_a, y_a, z_a) \right] \left[D_q^{\ell'} V(x_b, y_b, z_b) \right] \right\rangle_C = \\ & \frac{1}{(2\pi)^2} \int dk_x dk_y (\alpha_p)^\ell (\alpha_q^*)^{\ell'} \\ & \times \exp[ik_x(x_a - x_b) + ik_y(y_a - y_b) - k(z_a + z_b)] \\ & \times \int d(\Delta x') d(\Delta y') \exp[ik_x(\Delta x') + ik_y(\Delta y')] \\ & \times C(\Delta x', \Delta y'). \end{aligned} \quad (5.12)$$

Assuming the surface has no preferred direction, $C(\Delta x', \Delta y')$ is only a function of $\Delta r' = \sqrt{\Delta x'^2 + \Delta y'^2}$, and the evaluation of the last integral in Eq. 5.12 is equivalent to taking the

two-dimensional (2D) Fourier transform of a radially symmetric function (see, for example, Ref. [87]):

$$\begin{aligned}
W(k) &\equiv \frac{1}{2\pi} \int d(\Delta x') d(\Delta y') \exp[ik_x(\Delta x') + ik_y(\Delta y')] \\
&\quad \times C(\Delta x', \Delta y') \\
&= \int_0^\infty d(\Delta r') \Delta r' J_0(k\Delta r') C(\Delta r'), \tag{5.13}
\end{aligned}$$

where $J_0(\dots)$ is the zeroth-order Bessel function. Equation (5.12) may then be written as

$$\begin{aligned}
&\left\langle \left[D_p^\ell V(x, y, z) \right] \left[D_q^{\ell'} V(x + \Delta x, y + \Delta y, z + \Delta z) \right] \right\rangle_C \\
&= \frac{1}{2\pi} \int dk_x dk_y (\alpha_p)^\ell (\alpha_q^*)^{\ell'} W(k) \\
&\quad \times \exp[ik_x \Delta x + ik_y \Delta y - 2kz - k\Delta z]. \tag{5.14}
\end{aligned}$$

A generalisation of this result to mixed derivatives is straightforward, but the notation cumbersome. To evaluate Eq. (5.5), we need a slightly less general expression:

$$\begin{aligned}
&\left\langle \left[D_z^\ell V(x, y, z) \right] \left[D_z^{\ell'} V(x, y, z) \right] \right\rangle_C \\
&= (-1)^{\ell+\ell'} \int_0^\infty dk W(k) k^{1+\ell+\ell'} \exp[-2kz]. \tag{5.15}
\end{aligned}$$

It is helpful to rewrite this in a dimensionless form. A natural length scale for the surface is $w = 1/\sqrt{d}$, where d is the mean areal density of the surface patches. We assume that the covariance of the surface potential depends on w in such a way that it can be written in terms of a scaled covariance function \tilde{C} as $C(\Delta r') = \Phi_{\text{rms}}^2 \tilde{C}(\Delta r'/w)$, where $\Phi_{\text{rms}} \simeq [\langle V_s(x, y)^2 \rangle - \langle V_s(x, y) \rangle^2]^{1/2}$ is the rms variation of the surface potential from the mean. We now introduce

$$\tilde{W}(u) \equiv \int_0^\infty d(\Delta r'/w) (\Delta r'/w) J_0(u\Delta r'/w) \tilde{C}(\Delta r'/w), \tag{5.16}$$

which allows us to rewrite Eq. (5.15) as

$$\begin{aligned} & \frac{\left\langle \left[D_z^\ell V(x, y, z) \right] \left[D_z^{\ell'} V(x, y, z) \right] \right\rangle_{\mathcal{C}}}{(\Phi_{\text{rms}}^2/w^{\ell+\ell'})} \\ &= (-1)^{\ell+\ell'} \int_0^\infty du \tilde{W}(u) \times u^{1+\ell+\ell'} \times \exp[-2u(z/w)]. \end{aligned} \quad (5.17)$$

In general, for the $\tilde{W}(u)$ that we are interested in (see below), these integrals do not have closed forms. However, they may be approximated for large z/w using an asymptotic technique. Part of the integrand, $\tilde{W}(u) \times u^{1+\ell+\ell'}$, may be written as a Taylor series in u about $u = 0$. Once multiplied with the rest of the integrand ($\exp[-2u(z/w)]$), the terms in the resulting series can be individually integrated in closed form (see, for example, Ref. [88]). Introducing $G(\ell + \ell', z/w)$ as a shorthand for the left-hand side of Eq. (5.17), we obtain:

$$\begin{aligned} G(L, z/w) &= \\ & (-1)^L \sum_{i=0,2,4,\dots} \frac{(L+1+i)!}{i!} \times \tilde{W}^{(i)}(0) \times \left(\frac{w}{2z}\right)^{L+2+i}, \end{aligned} \quad (5.18)$$

where $L = \ell + \ell'$ and $\tilde{W}^{(i)}(0)$ is the i th derivative of $\tilde{W}(u)$ evaluated at $u = 0$. Note that from its definition [Eq. (5.16)], the odd derivatives of $\tilde{W}(u)$ vanish at $u = 0$. For use later in this paper, we write out the first few terms of this series for small L :

$$G(0, z/w) = \frac{1}{4} \tilde{W}(0) \left(\frac{w}{z}\right)^2 + \frac{3}{16} \tilde{W}^{(2)}(0) \left(\frac{w}{z}\right)^4 + \dots \quad (5.19a)$$

$$G(1, z/w) = -\frac{1}{4} \tilde{W}(0) \left(\frac{w}{z}\right)^3 - \frac{3}{8} \tilde{W}^{(2)}(0) \left(\frac{w}{z}\right)^5 + \dots \quad (5.19b)$$

$$G(2, z/w) = \frac{3}{8} \tilde{W}(0) \left(\frac{w}{z}\right)^4 + \frac{15}{16} \tilde{W}^{(2)}(0) \left(\frac{w}{z}\right)^6 + \dots \quad (5.19c)$$

$$G(3, z/w) = -\frac{3}{4} \tilde{W}(0) \left(\frac{w}{z}\right)^5 - \frac{45}{16} \tilde{W}^{(2)}(0) \left(\frac{w}{z}\right)^7 + \dots \quad (5.19d)$$

The first terms of these series are almost certain to dominate when $z \gg w$. From the definition of $\tilde{W}(u)$ in Eq. 5.16, it can be seen that $\tilde{W}(0) = 0$ requires that the covariance function satisfies $C(\Delta r') < 0$ over some range of $\Delta r'$, so that the integral taken over $\Delta r'$ is zero. This can be interpreted physically as antiferroelectric ordering of the surface potential; a case which seems unlikely to apply to polycrystalline metal surfaces.

It is important to note that, subject to the assumptions above, the details of $C(\Delta r')$ do not affect the (z/w) scaling of $G(L, z/w)$ but only its magnitude. Therefore, the z scaling of the patch fields is independent of the form of $C(\Delta r')$.

5.5 Models for the surface patch potentials

We will now calculate $G(L, z/w)$ using several different models for the electrostatic potential distribution on the surface. We start by calculating $C(\Delta r')$ for the model and then use this to find $\tilde{W}(0)$ and thus $G(L, z/w)$.

A commonly used model for the surface potential covariance is of the form [8, 44, 89]

$$C(\Delta r') = \Phi_{\text{rms}}^2 e^{-\gamma \left(\frac{\Delta r'}{w}\right)}, \quad (5.20)$$

where γ is dimensionless and on the order of 1. This model follows from Poisson waiting statistics for grain boundary crossings. This, however, is an assumption, and a formal justification does not appear in the literature. An advantage of this model is that $\tilde{W}(u)$ has a closed form [using Eq. (5.16)]:

$$\tilde{W}(u) = \frac{\gamma}{[\gamma^2 + u^2]^{3/2}}, \quad (5.21)$$

and thus the coefficients in the expansion of Eq. (5.19) are readily determined [$\tilde{W}(0) = 1/\gamma^2$, $\tilde{W}^{(2)}(0) = -3/\gamma^4$, etc.].

Motivated to provide a justification for Eq. (5.20) (and determine a specific value for γ), we performed Monte Carlo simulations to calculate a surface potential covariance function according to the following recipe: 1) A total of N patch ‘‘centers’’ were randomly put within a square with sides of length $w\sqrt{N}$ (for a mean areal patch density of $1/w^2$). 2)

At the center of this square, the patch with the closest center was determined. 3) As we move out from the center of the square in a specific direction, eventually another patch center becomes closer in distance than the initial one. The point at which this happens is considered to be at a grain boundary, and beyond this point there is zero correlation between the local potential and the potential at the starting point in the center of the square. 4) By repeating this process (generating N new patch centers within the square, and traveling out from the center until a grain boundary is reached), we may accumulate a surface potential correlation function. Provided N is sufficiently large, this model seems physically reasonable—we are assuming that grains have grown isotropically outwards from randomly placed centers on a surface. Figure 5.1 illustrates the results of one of these Monte Carlo simulations. A least-squares fit to Eq. (5.20) gives $\gamma \approx 1.9$, so that $\tilde{W}(0) \approx 0.28$.

We find that, instead of Eq. (5.20), the covariance is a better fit to the relationship:

$$C(\Delta r') = \Phi_{\text{rms}}^2 e^{-\gamma_1 \left(\frac{\Delta r'}{w}\right) - \gamma_2 \left(\frac{\Delta r'}{w}\right)^2}, \quad (5.22)$$

with $\gamma_1 \approx 1.144(4)$ and $\gamma_2 \approx 0.993(6)$. The covariance falls off faster with increasing separation in this model. Man et al. [89] compared experimentally measured covariance functions with a model similar to Eq. (5.20) and also found that, although exponential decay was exhibited for small separations, the covariance falls off faster for increasing separations (see their Fig. 2). However, a detailed comparison with our model is not possible as their surface was not isotropic.

We have tested this model by analyzing a scanning electron microscope (SEM) image of an evaporated gold structure on a silicon substrate (see Fig. 5.2). The “watershed” segmentation algorithm [90, 91] was used to determine the location of the grain boundaries. To calculate the covariance function we assume that the potential measured at two points separated by $\Delta r'$ is perfectly correlated if both points are on the same grain and uncorrelated if the points are on different grains. As Fig. 5.2(c) shows, the computed covariance is in good agreement with the Monte Carlo simulation [and thus also with the fit of Eq. (5.22)].

Unfortunately, a closed form for $\tilde{W}(k)$ does not appear to be possible for the model of Eq. (5.22). Nonetheless, it is possible to numerically compute the $\tilde{W}^{(i)}(0)$ required in

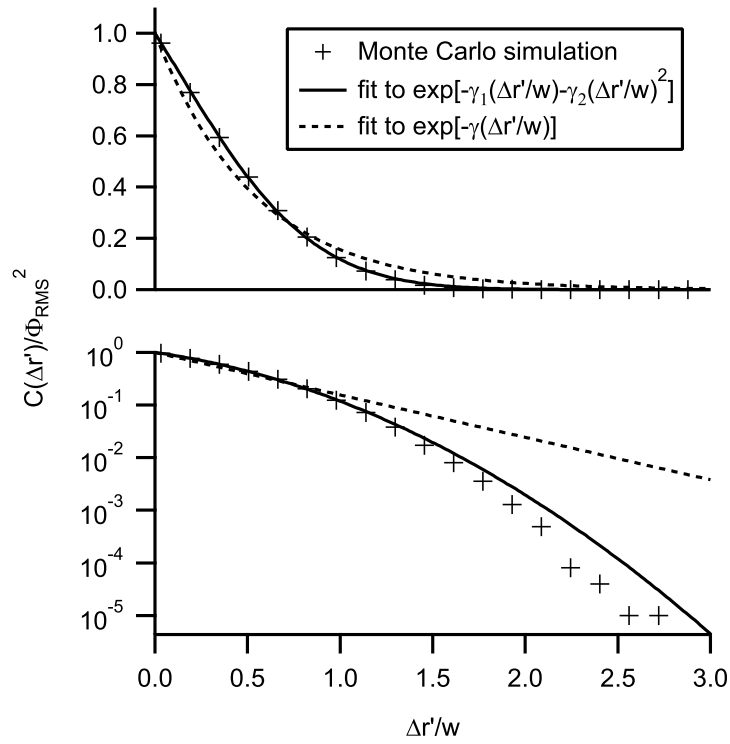


Figure 5.1: Monte Carlo simulation of the surface potential covariance function and two least-squares-fit models. In the lower plot a logarithmic vertical axis is used to illustrate the differences at large $\Delta r'/w$.

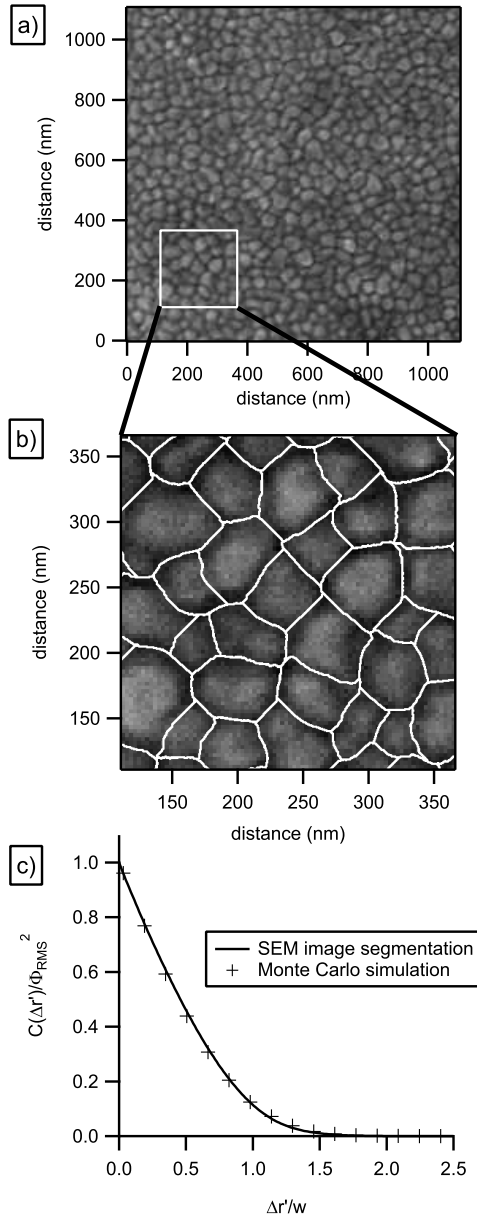


Figure 5.2: (a) SEM image of a gold surface obtained by thermal evaporation (this is a portion of Fig. 4 of Ref. [31]). (b) Grain boundaries (indicated by white lines) over a small region of the image as determined by watershed segmentation. The average area of a patch is $w^2 = (44 \text{ nm})^2$. (c) Computed covariance of the surface potential based on segmentation of the SEM image. To calculate this from the segmented image we assume constant surface potentials within grains, and completely uncorrelated potentials between grains. The Monte Carlo simulation of Fig. 5.1 is also shown for comparison.

Eq. (5.19) for any \tilde{C} using [see Eq. (5.16)]:

$$\tilde{W}^{(i)}(0) = [D^{(i)} J_0(0)] \int_0^\infty d\alpha \tilde{C}(\alpha) \alpha^{1+i}. \quad (5.23)$$

Performing these integrations for the model of Eq. (5.22), we find: $\tilde{W}(0) = \tilde{W}^{(0)}(0) \approx 0.207$, and $\tilde{W}^{(2)}(0) \approx -0.064$.

5.6 Fluctuations in the electric field

The $G(2, z/w)$ function determines the variance of the patch electric fields: $\langle F_z^2 \rangle_C \approx (3/8) \times (\Phi_{\text{rms}}^2/w^2) \times \tilde{W}(0) \times (w/z)^4$. Using Eq. (5.14), the variances of the x and y components of the electric field can be calculated. We find that they are each 1/2 of the result for z . Thus, we can summarize; with the model of Eq. (5.22), the rms electric field for $z \gg w$ is

$$E_{\text{rms}} \approx 0.39 \frac{\Phi_{\text{rms}}}{w} \left(\frac{w}{z} \right)^2. \quad (5.24)$$

This result is not especially sensitive to the particular patch model. For example, we have performed numerical simulations of the patch field over a large array of square patches (each w by w) with random potentials at distances $z \gg w$ and found that the numerical prefactor in Eq. (5.24) is 0.33 instead of 0.39. The model of Eq. (5.20) gives a numerical prefactor of 0.46. An approximate estimate similar to Eq. (5.24) has been provided by Sandoghdar *et al.* [37] and used by Mozley *et al.* [92].

It is worth asking when the higher-order terms of Eq. (5.19) can be neglected. In Fig. 5.3, we calculate $G(2, z/w)$ by direct integration of Eq. (5.15). The results due to the first two terms of Eq. (5.19c) are also shown. The figure indicates that keeping only the first term is an excellent approximation for $z \gg w$ (a similar plot for the model of Eq. (5.20) is given in Fig. 1 of Dubessy *et al.* [44]).

The rms patch field and the image field of an elementary-charge both scale in the same way with distance to the surface, so it is interesting to compare their magnitudes. If we assume a potential fluctuation of $\Phi_{\text{rms}}^2 = (90 \text{ mV})^2$ and $w = 50 \text{ nm}$, typical of thermally evaporated gold surfaces [93, 94], we find that the rms electric field due to patches is

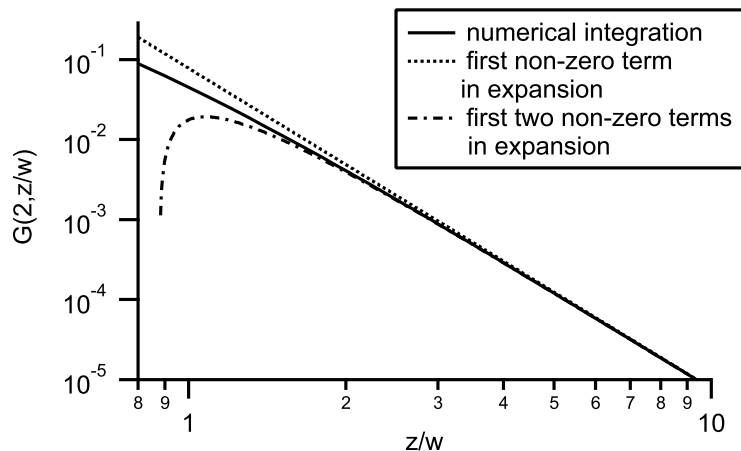


Figure 5.3: Comparison between numerical calculation of $G(2, z/w)$ for the model of Eq. (5.22) (using Eq. (5.15)), and the asymptotic series expansion of Eq. (5.19c), with the $\tilde{W}^{(i)}(0)$ coefficients calculated using Eq. (5.23).

approximately 5 times that of the elementary charge image field: $|\vec{E}_i| = q_e/[4\pi\epsilon_0(2z)^2]$. Seeing the influence of the image field due to an elementary charge near such a surface would be difficult.

Despite its simplicity and intrinsic importance, there does not appear to be any clear experimental observations that would support the validity of Eq. (5.24). Initial experiments with Rydberg atoms using microtrap technology have observed large dc fields due to the deposition of Rb on the surface [18] (see also Ref. [35]), possibly masking the influence of patch fields. Alkali adsorption has been recognized as a problem since the very early days of Rydberg atom-surface interaction experiments [95]. Some theoretical work on the influence of adsorbates has been done in the context of ion-surface collisions [96]. To avoid the problem of adsorbates, Dunning’s group switched to using xenon Rydberg atoms in their surface studies [19].

Dunning’s group has recently studied Rydberg atom image field ionization using Au(111) samples [20]. The surfaces consisted of multiple grains, typically 300–500 nm in size. Possibly due to contamination, the surface potential was inhomogeneous, with variations of up

to 70 mV from the average over length scales of 50–250 nm (shown in Fig. 1 of Ref. [20]). By using a scanning Kelvin probe to measure surface potential, they computed the statistical properties of the electric field above the surface and found that the field is consistent with their observed image field ionization. For $z \gtrsim 60$ nm, they found $E_{\text{rms}} \approx (5 \times 10^{-10} \text{ V m})/z^2$. Assuming our polycrystalline model is applicable, with $\Phi_{\text{rms}} \approx 22$ mV (determined from our analysis of Fig. 1 of Ref. [20]) and $w = 100$ nm, Eq. (5.24) predicts slightly larger fields, with $E_{\text{rms}} \approx (9 \times 10^{-10} \text{ V m})/z^2$. Given the uncertainty in determining w from the figure, this is reasonably consistent with the result in Ref. [20].

It is possible that polar or polarizable contaminants at grain boundaries could *reduce* the magnitude of the patch fields. Darling [97] did extensive scanning Kelvin probe measurements of the work function immediately above copper surfaces with large grain sizes, found that fluctuations were significantly less than one might expect, and attributed the reduction to oxidation of the surface and physisorbed molecules (e.g. water).

5.7 Patch fields and Rydberg atoms – estimates of energy level shifts

The statistical properties of the patch fields may now be combined with the atomic properties to predict the variance in the energy levels using Eq. (5.5). Writing this as a series in w/z :

$$\begin{aligned}
\langle(\Delta E)^2\rangle_C &\approx (M_1)^2 \langle F_z^2 \rangle_C + 2M_1 M_2 \langle F_z \partial_z F_z \rangle_C + \dots \\
&\approx (M_1)^2 \times (3/8) \tilde{W}(0) (\Phi_{\text{rms}}^2/w^2) \left(\frac{w}{z}\right)^4 \\
&\quad + 2M_1 M_2 \times (-3/4) \tilde{W}(0) (\Phi_{\text{rms}}^2/w^3) \left(\frac{w}{z}\right)^5 \\
&\quad + O\left(\left(\frac{w}{z}\right)^6\right).
\end{aligned} \tag{5.25}$$

The first term in this expansion is due to the rms z field and the atom's electric dipole, and is expected to be dominant at large z . However, the higher order terms in Eq. (5.25)

can be enhanced relative to the lower-order terms by increasing n (increasing the size of the atom). As the classical outer turning point of the Rydberg electron is $\approx n^2$ (in atomic units), the multipole moments of order ℓ scale with n like $M_\ell \approx n^{2\ell}$ (see, for example, Ref. [13]). These higher-order multipoles sense the field *variations* over the Rydberg orbit.

Under what conditions will variations in the patch fields over the extent of *individual* atoms contribute to the inhomogeneous broadening? We may estimate this by equating the first two terms written explicitly in Eq. (5.25). This tells us that the size of the Rydberg atom, n^2 , has to be approximately the distance of the atom to the surface before these would be comparable. Due to the interaction of the Rydberg atom with its image, this is a highly nonperturbative situation [77]. We conclude that it would be difficult to observe any effect of the variation in patch fields over the orbits of individual Rydberg atoms (at least when they have dipole moments of order n^2). An additional qualitative justification is given in Section 5.8.

We now give a simple numerical estimate for the inhomogeneous broadening of Rydberg energy levels due to patch fields. When z is large compared to w and the atom size, the first term in Eq. (5.25) dominates and the rms broadening will be $\delta E = M_1 \sqrt{\langle F_z^2 \rangle_C}$. For the extreme Stark states of hydrogen we have $M_1 = \mu_z = (3/2)n(n-1)$, which for $n = 30$ is 1.7 GHz/(V/cm) (this is also reasonable for non-hydrogenic atoms, assuming a large enough dc field is applied). For a typical thermally evaporated gold surface [93, 94], we assume $\Phi_{\text{rms}}^2 = (90 \text{ mV})^2$ and $w = 50 \text{ nm}$, giving $\sqrt{\langle F_z^2 \rangle_C} \approx 0.13 \text{ V/cm}$. We find that $\delta E \approx 200 \text{ MHz}$ – which should be straightforward to observe in optical excitation. For Rb atoms, a possible spectroscopic probe would be the last step in the $5s \rightarrow 5p \rightarrow 5d_{5/2} \rightarrow nk$ excitation sequence (where the last transition is enabled by a dc field sufficient to mix f character into the reddest nk states).

The extreme Stark states provide the largest broadening. Broadening due to patch fields will be much lower than this estimate if low angular momentum states are excited at fields small enough so that the Stark effect is second order.

5.8 Potential and field covariance functions

There is a qualitative way to understand why the inhomogeneities in the patch fields over the extent of individual Rydberg atoms would be difficult to observe. Equation (5.14) can be used to determine the covariance between the potential and derivatives of the potential measured at different locations in space. Using the result for the 2D Fourier transform of a radially symmetric function we obtain:

$$\begin{aligned}
& \left\langle \left[D_z^\ell V(x, y, z) \right] \left[D_z^{\ell'} V(x + \Delta x, y + \Delta y, z + \Delta z) \right] \right\rangle_C \\
&= (-1)^{\ell+\ell'} \frac{\Phi_{\text{rms}}^2}{w^{\ell+\ell'}} \times \int_0^\infty du \tilde{W}(u) u^{1+\ell+\ell'} \\
&\times J_0(u\Delta r/w) \exp[-u(2z + \Delta z)/w],
\end{aligned} \tag{5.26}$$

where $\Delta r = \sqrt{\Delta x^2 + \Delta y^2}$.

Again, like with Eq. (5.17), this integral can be approximated for large z/w by writing the $\tilde{W}(u)u^{1+\ell+\ell'}$ part of the integrand as a Taylor series and then integrating the individual terms. For covariances in the potential, we obtain for the first nonzero term

$$\begin{aligned}
& \langle V(x, y, z) V(x + \Delta x, y + \Delta y, z + \Delta z) \rangle_C \\
&\approx \frac{1}{4} \tilde{W}(0) \Phi_{\text{rms}}^2 \left(\frac{w}{z} \right)^2 \frac{1}{\left(1 + \frac{\Delta z}{2z}\right)^2} \frac{1}{\left[1 + \left(\frac{\Delta r}{2z + \Delta z}\right)^2\right]^{3/2}}.
\end{aligned} \tag{5.27}$$

For covariance in the z-component of the electric field, we obtain for the first nonzero term

$$\begin{aligned}
& \left\langle \left[D_z^1 V(x, y, z) \right] \left[D_z^1 V(x + \Delta x, y + \Delta y, z + \Delta z) \right] \right\rangle_C \\
&\approx \frac{3}{8} \frac{\tilde{W}(0) \Phi_{\text{rms}}^2}{w^2} \left(\frac{w}{z} \right)^4 \frac{1}{\left(1 + \frac{\Delta z}{2z}\right)^4} \frac{\left[1 - \frac{3}{2} \left(\frac{\Delta r}{2z + \Delta z}\right)^2\right]}{\left[1 + \left(\frac{\Delta r}{2z + \Delta z}\right)^2\right]^{7/2}}.
\end{aligned} \tag{5.28}$$

Higher order terms involve larger powers of w/z . These results have been written in such a way as to emphasize the influence of nonzero Δr and Δz as a correction factor to the

$\Delta r = \Delta z = 0$ result. It is apparent that z , the distance to the surface, sets the length scale for spatial variations in the potential and fields. Thus, we can understand in a qualitative way the results of the main text: a Rydberg atom should have a size comparable to its distance from the surface for spatial variations to be significant.

If an atom is moving near a surface, spatial variations in the fields manifest themselves as time-dependent variations experienced in the atom's frame. In this case, we note that the calculations of this section could be adapted to determine the power spectral densities of these fluctuations (using the Wiener-Khinchin theorem).

5.9 Summary and outlook

Rydberg atoms with permanent electric dipole moments have a high sensitivity to electric fields. We have shown that the patch fields near a typical metal surface can be large compared to the image field of an elementary charge and should be expected to cause measurable inhomogeneous broadening of Rydberg energy levels. The rms spatial variation in the field strength has a distance dependence of $1/z^2$. Spatial variations in the fields over the Rydberg atom orbit do not appear to be important. An experiment to verify the magnitude of the rms field and the expected scaling with surface distance [see Eq. (5.24)] would be useful in assessing the feasibility of coherently manipulating Rydberg atoms near polycrystalline surfaces and in planning future experiments.

We gratefully acknowledge discussions with Chris Gray (Guelph), and thank T. Darling (University of Nevada, Reno) for providing a copy of his PhD thesis [97], which contains useful background information on patch effects. We thank M. Mazurek and C. Liekhus-Schmaltz for comments on this manuscript. This work was supported by NSERC.

Chapter 6

Summary and future work

6.1 Summary of results

DC electric fields near the surface of an atom chip have been measured using optical spectroscopy of the $36s_{1/2}$ state using cold atoms released from the microtrap. The surface of the chip is heterogeneous, with evaporated gold wires and SiO_2 insulating gaps on a silicon substrate. The measured field magnitude and direction were strongly affected by voltage biasing of the chip wires related to how currents were applied, a surprising result given that all the currents were shut off and the chip wires returned to ground prior to the Rydberg excitation. The scaling of the field with distance to the surface was consistent with the $1/z$ power law given by a line charge on the surface, and the observed fields were attributed to charging of the insulating gaps between the wires. This result suggests that charging of insulating gaps may be minimized in future work with appropriate voltage biasing of structures on the surface.

Monte Carlo simulations have been used to calculate the decoherence of a coherent superposition of two low-angular Rydberg states with quadratic Stark shifts in the presence of $1/f$ electric field noise. The noise was assumed to have a power spectral density of the form $S_F(\omega) = S_0/\omega^\kappa$. Three frequency scalings relevant to models of noise near the surface ($\kappa = 1/2, 1, 3/2$) were investigated. Two types of experimental sequences were modelled:

1) Ramsey-type sequences, where the coherent superposition freely evolved for the entire measurement time, and 2) Hahn spin-echo sequences with a single refocusing pulse in the middle of the free evolution period to eliminate the effects of low-frequency field noise. For Ramsey-type sequences and $\kappa = 1$, the decay has been calculated analytically in the literature to be exponential at long times. The simulations in this work reproduce the exponential decay (and time constant) from the literature. Similar exponential decay was calculated for spin-echo sequences and all three values of κ . The decay rate is determined by the polarizability of the energy levels and the magnitude of the noise and is of the order $\Gamma_f = [(1/2) \times (\partial^2 \omega_{if} / \partial F^2) \times S_0]^{1/\kappa}$ in all three cases. This suggests that a relatively straightforward scaling law for the decoherence rate may apply over a range of κ for systems quadratically coupled to $1/f$ noise sources.

The ultimate sensitivity of electric field noise measurements has been estimated. For conveniently achievable n and dc field homogeneity requirements of 1 V/m, the estimated minimum detectable noise spectral density is $S_F(\omega) \approx 7 \times 10^{-12} \text{ V}^2 \text{ m}^{-2} \text{ s}$ for Ramsey or pulsed-refocusing sequences and about two orders of magnitude worse for spin-locking at a Rabi frequency of 1 MHz.

Using the $49s_{1/2}$ and $48s_{1/2}$ states of ^{87}Rb , the coherent control required for observation of Rabi oscillations and implementation of spin-echo and spin-locking measurements of noise has been demonstrated. The results of microwave spectroscopy and the decay of Hahn spin-echo coherence have been used to bound the electric field noise amplitude measured several mm away from the surface of the chip. These results appear to rule out $1/f^{3/2}$ noise far from the surface. The lower bound assuming pure $1/f$ noise, $S_F(\omega) \approx 20 (\text{V/m})^2 / \omega$, is about four orders of magnitude larger than the field noise typically seen by ions trapped much closer to the surface [11], suggesting that the origin of the noise may largely be technical. A substantial microwave standing wave pattern over the sample volume was observed. Focusing of the optical excitation beams to reduce the size of the Rydberg sample improved microwave field homogeneity over the sample; the field inhomogeneity was estimated to be a few per cent by using the decay of coherent Rabi oscillations. The amount of undesired population in the intermediate $48p_{3/2}$ state was estimated to be ≈ 0.05 through Monte Carlo simulation of the time-evolution of the density matrix.

Finally, the statistical properties of dc electric field inhomogeneities near metal surfaces have been calculated — these inhomogeneities are due to random potentials on the surface, such as may be caused by polycrystalline grain structures. The rms variation in the field strength scales with distance as $1/z^2$, and for parameters typical of an evaporated gold surface the rms field inhomogeneity is approximately 5 times larger than the image field of an elementary point charge, which also scales as $1/z^2$. Spatial variations in the field over the size of a Rydberg atom are not important.

6.2 Future work

One obvious direction in future work is to measure decoherence times of Rydberg state superpositions near the surface of the chip. Spin-locking techniques will be useful to determine the frequency scaling of any noise near the chip; another interesting method for determining the frequency scaling of $1/f^\kappa$ noise involves comparing the coherence decay times of Ramsey and Hahn spin-echo sequences as the ratio of these times is quite sensitive to κ provided $\kappa > 1$ [98].

More detailed study of the ac field spectrum far away from the chip surface, particularly measurement of Hahn spin-echo decay out to times comparable to the Rydberg state lifetimes, will better constrain the level of background noise far from the chip. This will also provide a better basis for confirming increased levels of electric field noise near the surface. Measurement of the background noise using spin-locking sequences will give better determination of the frequency dependence of the noise and also help identify any peaks in the noise spectrum which may be associated with technical noise in the apparatus.

Installation of a new atom chip [99], in which the current-carrying wires are covered with a grounded electrostatic shield layer of evaporated gold, will remove the effects of charging on the dielectric gaps between wires. This new chip will allow the study of atom-surface interactions for a well-defined homogeneous flat surface, so that the origins of any observed field noise or dc inhomogeneity are likely to be intrinsic to many types of atom-surface devices and therefore of general interest.

References

- [1] S. Seidelin, J. Chiaverini, R. Reichle, J. J. Bollinger, D. Leibfried, J. Britton, J. H. Wesenberg, R. B. Blakestad, R. J. Epstein, D. B. Hume, W. M. Itano, J. D. Jost, C. Langer, R. Ozeri, N. Shiga, and D. J. Wineland, “Microfabricated surface-electrode ion trap for scalable quantum information processing,” *Phys. Rev. Lett.*, vol. 96, p. 253003, Jun 2006.
- [2] J. Fortágh and C. Zimmermann, “Magnetic microtraps for ultracold atoms,” *Rev. Mod. Phys.*, vol. 79, p. 235, 2007.
- [3] J. Reichel and V. Vuletić, *Atom Chips*. John Wiley & Sons, 2011.
- [4] A. S. Sørensen, C. H. van der Wal, L. I. Childress, and M. D. Lukin, “Capacitive coupling of atomic systems to mesoscopic conductors,” *Phys. Rev. Lett.*, vol. 92, no. 6, p. 063601, 2004.
- [5] S. D. Hogan, J. A. Agner, F. Merkt, T. Thiele, S. Filipp, and A. Wallraff, “Driving Rydberg-Rydberg transitions from a co-planar microwave waveguide,” *Phys. Rev. Lett.*, vol. 108, p. 063004, 2012.
- [6] A. André, D. DeMille, J. M. Doyle, M. D. Lukin, S. E. Maxwell, P. Rabi, R. J. Schoelkopf, and P. Zoller, “A coherent all-electrical interface between polar molecules and mesoscopic superconducting resonators,” *Nature Physics*, vol. 2, pp. 636–642, 2006.

- [7] R. P. Abel, C. Carr, U. Krohn, and C. S. Adams, “Electrometry near a dielectric surface using Rydberg electromagnetically induced transparency,” *Phys. Rev. A*, vol. 84, p. 023408, 2011.
- [8] M. S. Rzchowski and J. R. Henderson, “Properties of random fields outside a metal surface and their effect on time-of-flight spectroscopy,” *Phys. Rev. A*, vol. 38, p. 4622, 1988.
- [9] J. D. Carter and J. D. D. Martin, “Energy shifts of Rydberg atoms due to patch fields near metal surfaces,” *Phys. Rev. A*, vol. 83, p. 032902, 2011.
- [10] N. Daniilidis, S. Narayanan, S. A. Möller, R. Clark, T. E. Lee, P. J. Leek, A. Wallraff, S. Schulz, F. Schmidt-Kaler, and H. Häffner, “Fabrication and heating rate study of microscopic surface electrode ion traps,” *New Journal of Physics*, vol. 13, no. 1, p. 013032, 2011.
- [11] D. A. Hite, Y. Colombe, A. C. Wilson, K. R. Brown, U. Warring, R. Jördens, J. D. Jost, K. S. McKay, D. P. Pappas, D. Leibfried, and D. J. Wineland, “100-fold reduction of electric-field noise in an ion trap cleaned with *in situ* argon-ion-beam bombardment,” *Phys. Rev. Lett.*, vol. 109, p. 103001, Sep 2012.
- [12] M. Müller, H. Haakh, T. Calarco, C. Koch, and C. Henkel, “Prospects for fast Rydberg gates on an atom chip,” *Quantum Information Processing*, vol. 10, pp. 771–792, 2011.
- [13] T. F. Gallagher, *Rydberg Atoms*. Cambridge: Cambridge University Press, 1994.
- [14] A. Osterwalder and F. Merkt, “Using high Rydberg states as electric field sensors,” *Phys. Rev. Lett.*, vol. 82, p. 1831, 1999.
- [15] J. Sedlacek, A. Schwettmann, H. Kübler, R. Löw, T. Pfau, and J. P. Shaffer, “Quantum assisted electrometry using bright atomic resonances.” arXiv:1205.4461, 2012.
- [16] T. F. Gallagher, L. M. Humphrey, W. E. Cooke, R. M. Hill, and S. A. Edelstein, “Field ionization of highly excited states of sodium,” *Phys. Rev. A*, vol. 16, pp. 1098–1108, Sep 1977.

- [17] T. R. Gentile, B. J. Hughey, D. Kleppner, and T. W. Ducas, “Experimental study of one- and two-photon Rabi oscillations,” *Phys. Rev. A*, vol. 40, pp. 5103–5115, Nov 1989.
- [18] A. Tauschinsky, R. M. T. Thijssen, S. Whitlock, H. B. van Linden van den Heuvell, and R. J. C. Spreeuw, “Spatially resolved excitation of Rydberg atoms and surface effects on an atom chip,” *Phys. Rev. A*, vol. 81, no. 6, p. 063411, 2010.
- [19] S. B. Hill, C. B. Haich, Z. Zhou, P. Nordlander, and F. B. Dunning, “Ionization of Rydberg atoms at a metal surface,” *Phys. Rev. Lett.*, vol. 85, pp. 5444–5447, 2000.
- [20] Y. Pu, D. D. Neufeld, and F. B. Dunning, “Ionization of Rydberg atoms at metallic surfaces: Influence of stray fields,” *Phys. Rev. A*, vol. 81, no. 4, p. 042904, 2010.
- [21] J. D. Carter, O. Cherry, and J. D. D. Martin, “Electric-field sensing near the surface microstructure of an atom chip using cold Rydberg atoms,” *Phys. Rev. A*, vol. 86, p. 053401, Nov 2012.
- [22] L. Isenhower, E. Urban, X. L. Zhang, A. T. Gill, T. Henage, T. A. Johnson, T. G. Walker, and M. Saffman, “Demonstration of a neutral atom controlled-NOT quantum gate,” *Phys. Rev. Lett.*, vol. 104, p. 010503, 2010.
- [23] A. Gaëtan, Y. Miroshnychenko, T. Wilk, A. Chotia, M. Viteau, D. Comparat, P. Pillet, A. Browaeys, and P. Grangier, “Observation of collective excitation of two individual atoms in the Rydberg blockade regime,” *Nature Phys.*, vol. 5, pp. 115–118, 2009.
- [24] G. H. Low, P. F. Herskind, and I. L. Chuang, “Finite-geometry models of electric field noise from patch potentials in ion traps,” *Phys. Rev. A*, vol. 84, p. 053425, 2011.
- [25] Y.-J. Lin, I. Teper, C. Chin, and V. Vuletić, “Impact of the Casimir-Polder potential and Johnson noise on Bose-Einstein condensate stability near surfaces,” *Phys. Rev. Lett.*, vol. 92, no. 5, p. 050404, 2004.
- [26] R. Löw, H. Weimer, J. Nipper, J. B. Balewski, B. Butscher, H. P. Büchler, and T. Pfau, “An experimental and theoretical guide to strongly interacting Rydberg gases,” *J. Phys. B: At. Mol. Opt. Phys.*, vol. 45, p. 113001, 2012.

- [27] S. Wildermuth, P. Krüger, C. Becker, M. Brajdic, S. Haupt, A. Kasper, R. Folman, and J. Schmiedmayer, “Optimized magneto-optical trap for experiments with ultracold atoms near surfaces,” *Phys. Rev. A*, vol. 69, p. 030901, 2004.
- [28] J.-H. Choi, J. R. Guest, A. P. Povilus, E. Hansis, and G. Raithel, “Magnetic trapping of long-lived cold Rydberg atoms,” *Phys. Rev. Lett.*, vol. 95, p. 243001, 2005.
- [29] P. Hyafil, J. Mozley, A. Perrin, J. Tailleur, G. Nogues, M. Brune, J. M. Raimond, and S. Haroche, “Coherence-preserving trap architecture for long-term control of giant Rydberg atoms,” *Phys. Rev. Lett.*, vol. 93, no. 10, p. 103001, 2004.
- [30] SAES Getters, Viale Italia 77, Lainate (Milan), Italy.
- [31] O. Cherry, J. D. Carter, and J. D. D. Martin, “An atom chip for the manipulation of ultracold atoms,” *Can. J. Phys.*, vol. 87, p. 633, 2009.
- [32] C. E. Liekhus-Schmaltz, R. Mantifel, M. Torabifard, I. B. Burgess, and J. D. D. Martin, “Injection-locked diode laser current modulation for Pound-Drever-Hall frequency stabilization using transfer cavities,” *J. Opt. Soc. Am. B*, vol. 29, p. 1394, 2012.
- [33] M. Tanasittikosol, C. Carr, C. S. Adams, and K. J. Weatherill, “Subnatural linewidths in two-photon excited-state spectroscopy,” *Phys. Rev. A*, vol. 85, p. 033830, Mar 2012.
- [34] B. Deal, “Standardized terminology for oxide charges associated with thermally oxidized silicon,” *IEEE Trans. Electron Devices*, vol. 27, pp. 606 – 608, 1980.
- [35] J. M. Obrecht, R. J. Wild, and E. A. Cornell, “Measuring electric fields from surface contaminants with neutral atoms,” *Phys. Rev. A*, vol. 75, no. 6, p. 062903, 2007.
- [36] H. Hattermann, M. Mack, F. Karlewski, F. Jessen, D. Cano, and J. Fortágh, “Detrimental adsorbate fields in experiments with cold Rydberg gases near surfaces,” *Phys. Rev. A*, vol. 86, p. 022511, 2012.
- [37] V. Sandoghdar, C. I. Sukenik, S. Haroche, and E. A. Hinds, “Spectroscopy of atoms confined to the single node of a standing wave in a parallel-plate cavity,” *Phys. Rev. A*, vol. 53, p. 1919, 1996.

- [38] P. Krüger, X. Luo, M. W. Klein, K. Brugger, A. Haase, S. Wildermuth, S. Groth, I. Bar-Joseph, R. Folman, and J. Schmiedmayer, “Trapping and manipulating neutral atoms with electrostatic fields,” *Phys. Rev. Lett.*, vol. 91, p. 233201, 2003.
- [39] J. Bylander, S. Gustavsson, F. Yan, F. Yoshihara, K. Harrabi, G. Fitch, D. G. Cory, Y. Nakamura, J.-S. Tsai, and W. D. Oliver, “Noise spectroscopy through dynamical decoupling with a superconducting flux qubit,” *Nature Physics*, vol. 7, pp. 565–570, 2011.
- [40] A. Safavi-Naini, P. Rabl, P. F. Weck, and H. R. Sadeghpour, “Microscopic model of electric-field-noise heating in ion traps,” *Phys. Rev. A*, vol. 84, p. 023412, 2011.
- [41] Q. A. Turchette, Kielpinski, B. E. King, D. Leibfried, D. M. Meekhof, C. J. Myatt, M. A. Rowe, C. A. Sackett, C. S. Wood, W. M. Itano, C. Monroe, and D. J. Wineland, “Heating of trapped ions from the quantum ground state,” *Phys. Rev. A*, vol. 61, p. 063418, May 2000.
- [42] J. I. Cirac and P. Zoller, “Quantum computations with cold trapped ions,” *Phys. Rev. Lett.*, vol. 74, pp. 4091–4094, May 1995.
- [43] S. X. Wang, Y. Ge, J. Labaziewicz, E. Dauler, K. Berggren, and I. L. Chuang, “Superconducting microfabricated ion traps,” *Applied Physics Letters*, vol. 97, no. 24, p. 244102, 2010.
- [44] R. Dubessy, T. Coudreau, and L. Guidoni, “Electric field noise above surfaces: A model for heating-rate scaling law in ion traps,” *Phys. Rev. A*, vol. 80, no. 3, p. 031402, 2009.
- [45] D. J. Wineland, C. Monroe, W. M. Itano, D. Leibfried, B. E. King, and D. M. Meekhof, “Experimental issues in coherent quantum-state manipulation of trapped atomic ions,” *J. Res. Natl. Inst. Stand. Technol.*, vol. 103, p. 259, May-June 1998.
- [46] M. A. Gesley and L. W. Swanson, “Spectral analysis of adsorbate induced field-emission flicker noise,” *Phys. Rev. B*, vol. 32, pp. 7703–7712, Dec 1985.

- [47] R. Gomer, “Diffusion of adsorbates on metal surfaces,” *Reports on Progress in Physics*, vol. 53, no. 7, p. 917, 1990.
- [48] A. Safavi-Naini, E. Kim, P. F. Weck, P. Rabl, and H. R. Sadeghpour, “Influence of monolayer contamination on electric-field-noise heating in ion traps,” *Phys. Rev. A*, vol. 87, p. 023421, Feb 2013.
- [49] C. Henkel and B. Horowitz, “Noise from metallic surfaces: Effects of charge diffusion,” *Phys. Rev. A*, vol. 78, p. 042902, Oct 2008.
- [50] L. M. K. Vandersypen and I. L. Chuang, “NMR techniques for quantum control and computation,” *Rev. Mod. Phys.*, vol. 76, pp. 1037–1069, Jan 2005.
- [51] S. Lasič, J. Stepišnik, and A. Mohorič, “Displacement power spectrum measurement by CPMG in constant gradient,” *Journal of Magnetic Resonance*, vol. 182, no. 2, pp. 208 – 214, 2006.
- [52] G. Ithier, E. Collin, P. Joyez, P. J. Meeson, D. Vion, D. Esteve, F. Chiarello, A. Shnirman, Y. Makhlin, J. Schrieffer, and G. Schön, “Decoherence in a superconducting quantum bit circuit,” *Phys. Rev. B*, vol. 72, p. 134519, Oct 2005.
- [53] M. Loretz, T. Rosskopf, and C. L. Degen, “Radio-frequency magnetometry using a single electron spin,” *Phys. Rev. Lett.*, vol. 110, p. 017602, Jan 2013.
- [54] R. S. Minns, M. R. Kutteruf, H. Zaidi, L. Ko, and R. R. Jones, “Preserving coherence in Rydberg quantum bits,” *Phys. Rev. Lett.*, vol. 97, p. 040504, Jul 2006.
- [55] S. Yoshida, C. O. Reinhold, J. Burgdörfer, W. Zhao, J. J. Mestayer, J. C. Lancaster, and F. B. Dunning, “Extracting irreversible dephasing rates from electric dipole echoes in Rydberg stark wave packets,” *Phys. Rev. A*, vol. 78, p. 063414, Dec 2008.
- [56] R. K. Wangsness and F. Bloch, “The dynamical theory of nuclear induction,” *Phys. Rev.*, vol. 89, pp. 728–739, Feb 1953.
- [57] A. G. Redfield, “On the theory of relaxation processes,” *IBM Journal of Research and Development*, vol. 1, no. 1, pp. 19–31, 1957.

- [58] E. L. Hahn, “Spin echoes,” *Phys. Rev.*, vol. 80, pp. 580–594, Nov 1950.
- [59] H. Y. Carr and E. M. Purcell, “Effects of diffusion on free precession in nuclear magnetic resonance experiments,” *Phys. Rev.*, vol. 94, pp. 630–638, May 1954.
- [60] S. Meiboom and D. Gill, “Modified spin-echo method for measuring nuclear relaxation times,” *Rev. Sci. Instrum.*, vol. 29, pp. 688–691, May 1958.
- [61] D. Vion, A. Aassime, A. Cottet, P. Joyez, H. Pothier, C. Urbina, D. Esteve, and M. H. Devoret, “Manipulating the quantum state of an electrical circuit,” *Science*, vol. 296, no. 5569, pp. 886–889, 2002.
- [62] Y. Makhlin and A. Shnirman, “Dephasing of solid-state qubits at optimal points,” *Phys. Rev. Lett.*, vol. 92, p. 178301, Apr 2004.
- [63] R. Kubo, M. Toda, and N. Hashitsume, *Statistical physics II: Nonequilibrium statistical mechanics*. Springer-Verlag, second ed., 1985.
- [64] J. A. Jones, “Quantum computing with NMR,” *Progress in Nuclear Magnetic Resonance Spectroscopy*, vol. 59, no. 2, pp. 91 – 120, 2011.
- [65] S. Wimperis, “Broadband, narrowband, and passband composite pulses for use in advanced NMR experiments,” *Journal of Magnetic Resonance, Series A*, vol. 109, no. 2, pp. 221 – 231, 1994.
- [66] A. G. Redfield, “Nuclear magnetic resonance saturation and rotary saturation in solids,” *Phys. Rev.*, vol. 98, pp. 1787–1809, Jun 1955.
- [67] F. W. Cummings, “Long-time transition probabilities for a two-level system interacting with a stochastic electromagnetic field,” *American Journal of Physics*, vol. 30, no. 12, pp. 898–901, 1962.
- [68] B. Bidégaray, A. Bourgeade, and D. Reignier, “Introducing physical relaxation terms in Bloch equations,” *Journal of Computational Physics*, vol. 170, no. 2, pp. 603 – 613, 2001.

- [69] M. L. Zimmerman, M. G. Littman, M. M. Kash, and D. Kleppner, “Stark structure of the Rydberg states of alkali-metal atoms,” *Phys. Rev. A*, vol. 20, pp. 2251–2275, Dec 1979.
- [70] P. N. Brown, A. C. Hindmarsh, and G. D. Byrne, “DVODE: Variable-coefficient ordinary differential equation solver, with fixed-leading-coefficient implementation.” <http://www.netlib.org/ode/vode.f>.
- [71] Gounand, F., Hugon, M., and Fournier, P.R., “Radiative lifetimes of highly excited states in rubidium,” *J. Phys. France*, vol. 41, no. 2, pp. 119–121, 1980.
- [72] I. I. Beterov, I. I. Ryabtsev, D. B. Tretyakov, and V. M. Entin, “Quasiclassical calculations of blackbody-radiation-induced depopulation rates and effective lifetimes of Rydberg ns , np , and nd alkali-metal atoms with $n \leq 80$,” *Phys. Rev. A*, vol. 79, p. 052504, May 2009.
- [73] W. E. Cooke and T. F. Gallagher, “Effects of blackbody radiation on highly excited atoms,” *Phys. Rev. A*, vol. 21, pp. 588–593, Feb 1980.
- [74] W. Li, I. Mourachko, M. W. Noel, and T. F. Gallagher, “Millimeter-wave spectroscopy of cold Rb Rydberg atoms in a magneto-optical trap: Quantum defects of the ns , np , and nd series,” *Phys. Rev. A*, vol. 67, p. 052502, May 2003.
- [75] L. A. Jones, J. D. Carter, and J. D. D. Martin, “Rydberg atoms with a reduced sensitivity to dc and low-frequency electric fields,” *Phys. Rev. A*, vol. 87, p. 023423, Feb 2013.
- [76] V. Sandoghdar, C. I. Sukenik, E. A. Hinds, and S. Haroche, “Direct measurement of the van der Waals interaction between an atom and its images in a micron-sized cavity,” *Phys. Rev. Lett.*, vol. 68, no. 23, pp. 3432–3435, 1992.
- [77] A. V. Chaplik, “Ionization of highly excited atoms near a metal surface,” *Soviet Physics JETP*, vol. 27, p. 178, 1968.
- [78] C. Herring and M. H. Nichols, “Thermionic emission,” *Rev. Mod. Phys.*, vol. 21, p. 185, 1949.

- [79] N. W. Ashcroft and N. D. Mermin, *Solid State Physics*. Philadelphia: Saunders College, 1976.
- [80] N. E. Singh-Miller and N. Marzari, “Surface energies, work functions, and surface relaxations of low-index metallic surfaces from first principles,” *Phys. Rev. B*, vol. 80, no. 23, p. 235407, 2009.
- [81] I. Lesanovsky, J. Schmiedmayer, and P. Schmelcher, “Electronic structure of atoms in magnetic quadrupole traps,” *Phys. Rev. A*, vol. 69, no. 5, p. 053405, 2004.
- [82] J. A. Crosse, S. A. Ellingsen, K. Clements, S. Y. Buhmann, and S. Scheel, “Thermal Casimir-Polder shifts in Rydberg atoms near metallic surfaces,” *Phys. Rev. A*, vol. 82, no. 1, p. 010901, 2010.
- [83] D. Petrosyan, G. Bensky, G. Kurizki, I. Mazets, J. Majer, and J. Schmiedmayer, “Reversible state transfer between superconducting qubits and atomic ensembles,” *Phys. Rev. A*, vol. 79, no. 4, p. 040304, 2009.
- [84] F. C. Witteborn and W. M. Fairbank, “Apparatus for measuring the force of gravity on freely falling electrons,” *Rev. Sci. Instrum.*, vol. 48, p. 1, 1977.
- [85] L. D. Landau and L. M. Lifshitz, *Quantum mechanics, non-relativistic theory*. Butterworth-Heinemann, 3rd ed., 1981.
- [86] C. G. Gray and K. E. Gubbins, *Theory of molecular fluids. Volume 1: Fundamentals*. Oxford: Oxford, 1984.
- [87] N. Baddour, “Operational and convolution properties of two-dimensional Fourier transforms in polar coordinates,” vol. 26, pp. 1767–1777, 2009.
- [88] J. G. Simmonds and J. E. Mann Jr., *A first look at perturbation theory*. Dover, 2nd ed., 1997.
- [89] C.-S. Man, R. Paroni, Y. Xiang, and E. A. Kenik, “On the geometric autocorrelation function of polycrystalline materials,” *Journal of Computational and Applied Mathematics*, vol. 190, no. 1-2, pp. 200 – 210, 2006.

- [90] R. C. Gonzalez and R. E. Woods, *Digital Image Processing*. New Jersey: Prentice-Hall, 2nd ed., 2002.
- [91] D. Sage, “Watershed segmentation plugin for ImageJ.” <http://bigwww.epfl.ch/sage/soft/watershed/>, 2010.
- [92] J. Mozley, P. Hyafil, G. Nogues, M. Brune, J.-M. Raimond, and S. Haroche *Eur. Phys. J. D.*, vol. 35, pp. 43–57, 2005.
- [93] C. C. Speake and C. Trenkel, “Forces between conducting surfaces due to spatial variations of surface potential,” *Phys. Rev. Lett.*, vol. 90, no. 16, p. 160403, 2003.
- [94] S. Groth, P. Kruger, S. Wildermuth, R. Folman, T. Fernholz, J. Schmiedmayer, D. Mahalu, and I. Bar-Joseph, “Atom chips: Fabrication and thermal properties,” *Appl. Phys. Lett.*, vol. 85, no. 14, pp. 2980–2982, 2004.
- [95] C. A. Kocher and C. R. Taylor, “High-Rydberg atoms as probes of surface electric fields and sub-monolayer adsorption,” *Physics Letters A*, vol. 124, no. 1-2, pp. 68 – 72, 1987.
- [96] Z. L. Mišković, S. G. Davison, and F. O. Goodman, “Statistical treatment of adsorbate effects on charge transfer in ion-surface collisions,” *Nucl. Instrum. Methods B*, vol. 100, no. 2-3, pp. 431 – 437, 1995.
- [97] T. Darling. PhD thesis, University of Melbourne, 1989.
- [98] S. M. Anton, C. Müller, J. S. Birenbaum, S. R. O’Kelley, A. D. Fefferman, D. S. Golubev, G. C. Hilton, H.-M. Cho, K. D. Irwin, F. C. Wellstood, G. Schön, A. Shnirman, and J. Clarke, “Pure dephasing in flux qubits due to flux noise with spectral density scaling as $1/f^\alpha$,” *Phys. Rev. B*, vol. 85, p. 224505, Jun 2012.
- [99] O. Cherry, “Fabrication of an atom chip for Rydberg atom-metal surface interaction studies,” Master’s thesis, University of Waterloo, 2007.